BEHAVIOR OF FRP REINFORCED AAC STRUCTURAL ELEMENTS

A THESIS SUBMITTED TO
THE GRADUATE SCHOOL OF NATURAL AND APPLIED SCIENCES
OF
MIDDLE EAST TECHNICAL UNIVERSITY

BY

ERTÜRK TUNCER

IN PARTIAL FULFILLMENT OF THE REQUIREMENTS
FOR
THE DEGREE OF MASTER OF SCIENCE
IN
CIVIL ENGINEERING

APRIL 2018

Approval of the thesis:

BEHAVIOR OF FRP REINFORCED AAC STRUCTURAL ELEMENTS

submitted by **ERTÜRK TUNCER** in partial fulfillment of the requirements for the degree of **Master of Science in Civil Engineering Department, Middle East Technical University** by,

Prof. Dr. Halil Kalıpçılar
Dean, Graduate School of **Natural and Applied Sciences** _____

Prof. Dr. İsmail Özgür Yaman
Head of Department, **Civil Engineering Dept., METU** _____

Prof. Dr. Barış Binici
Supervisor, **Civil Engineering Dept., METU** _____

Examining Committee Members:

Prof. Dr. M. Altuğ Erberik
Civil Engineering Dept., METU _____

Prof. Dr. Barış Binici
Civil Engineering Dept., METU _____

Prof. Dr. Erdem Canbay
Civil Engineering Dept., METU _____

Prof. Dr. Mehmet Utku
Civil Engineering Dept., METU _____

Dr. Alper Aldemir
Civil Engineering Dept., Hacettepe University _____

Date: 25.04.2018

I hereby declare that all information in this document has been obtained and presented in accordance with academic rules and ethical conduct. I also declare that, as required by these rules and conduct, I have fully cited and referenced all material and results that are not original to this work.

Name, Last name: Ertürk Tuncer

Signature :

ABSTRACT

BEHAVIOR OF FRP REINFORCED AAC STRUCTURAL ELEMENTS

Tuncer, Ertürk

M.S., Department of Civil Engineering

Supervisor: Prof. Dr. Barış Binici

April 2018, 98 pages

AAC beams are classically manufactured by using steel reinforcement. However, in order to obtain more economical design and to prevent corrosion, it is also possible to apply FRP reinforcement. For this purpose, first, an experimental study was conducted to investigate the response of steel reinforced and fiber reinforced AAC beam specimens under four point bending test. All the tests were performed with the collaboration of Middle East Technical University and AKG Gazbeton. Unidirectional single layer carbon and glass fiber composites were applied at the bottom and top faces of the specimens throughout either half or full section width. The main parameters under investigation were strength, stiffness, ductility and energy absorption capacity. Secondly, a closed form based section analysis program was prepared to compute capacity analysis and load-displacement relation of AAC specimens having steel reinforcement or composite fiber laminates. In this way, experimental results were correlated with the developed analytical modeling. It was observed that acceptable accuracy was obtained when experimental and theoretical results were compared. In other words, validation of analytical modeling was revealed. At the final stage of this study, usable

debonding strain equations depending on the ratio of beam width to fiber width and number of fiber layer were recommended. Design charts were prepared by using these strain equations. In these design charts, based on demanded uniform distributed loads, the most economical FRP schemes were proposed for AAC beams having different span lengths and cross section dimensions.

Keywords: Autoclaved Aerated Concrete (AAC) , Fiber Reinforced Polymer (FRP), Analytical modeling, Four point bending test, Load-displacement relation

ÖZ

LİFLİ POLİMER İLE DONATILANDIRILMIŞ GAZBETON YAPI ELEMANLARININ DAVRANIŞI

Tuncer, Ertürk

Yüksek Lisans, İnşaat Mühendisliği Bölümü

Tez Yöneticisi: Prof. Dr. Barış Binici

Nisan 2018, 98 sayfa

Gazbeton kirişler klasik olarak çelik donatı kullanılarak imal edilmektedir. Ancak daha ekonomik tasarım elde etmek ve paslanmayı önlemek için LP donatı uygulamak da mümkündür. Bu amaçla, ilk olarak çelik donatılı ve lif donatılı gazbeton kiriş numunelerin dört noktadan yüklü eğilme testi altındaki davranışını araştırmak için deneysel çalışma yürütülmüştür. Tüm testler AKG Gazbeton ve Orta Doğu Teknik Üniversitesi işbirliğiyle gerçekleştirilmiştir. Tek yönlü ve tek tabakalı karbon ve cam lifli kompozitler, numunelerin alt ve üst yüzlerine tam veya yarım kesit genişliğinde uygulanmıştır. Araştırmanın ana parametreleri dayanım, rijitlik, süneklik ve enerji yutma kapasitesidir. İkinci olarak, çelik donatılı veya kompozit lif kumaşlı gazbeton numunelerin kapasite analizi ve yük-deplasman ilişkisini hesaplamak için kapalı çözüm esaslı kesit analiz programı hazırlanmıştır. Böylelikle, deney sonuçları geliştirilen analitik modelle ilişkilendirilmiştir. Deney ve teorik sonuçlar karşılaştırıldığında kabul edilebilir hassasiyet elde edildiği gözlenmiştir. Bir başka deyişle, analitik modelin geçerliliği ortaya çıkmıştır. Bu çalışmanın sonunda, kiriş genişliğinin lif genişliği oranına ve lif adedine bağlı olarak kullanılabilir sıyrılma deformasyon denklemleri önerilmiştir. Bu

deformasyon denklemleri kullanılarak tasarım abakları hazırlanmıştır. Bu tasarım abaklarında, talep edilen düzgün yayılı yükler esas alınarak, farklı açıklıklara ve enkesit ölçülerine sahip gazbeton kirişler için en ekonomik LP yerleşimleri önerilmiştir.

Anahtar Kelimeler: Gazbeton, Lifli Polimer (LP), Analitik model, Dört noktadan yüklü eğilme testi, Yük-deplasman ilişkisi

To my family

ACKNOWLEDGEMENTS

I would like to express my deepest gratitude to my supervisor, Prof. Dr. Barış Binici, for his valuable guidance, useful advice, criticism and sincere encouragement throughout this research process. It has been a great honor and substantial experience for me to work with Professor Binici.

Besides my supervisor Prof.Binici, I would like to thank all committee members, Prof. Dr. Erdem Canbay, Prof. Dr. Murat Altuğ Erberik, Prof. Dr. Mehmet Utku and Dr. Alper Aldemir for sharing their valuable time, important insights, and beneficial contributions on this thesis. Their crucial comments and suggestions, along with critical questions affected and directed me to broaden my perspectives throughout the research. I believe this remarkable research process will contribute to my academic life both in the short and long term.

I also want to thank AKG Gazbeton personnels; application chief Zafer Eryurtlu, R & D manager Uğur Uzgan, AAC panel production responsible Mustafa Kaan Öğdü and foreman Mustafa.

Finally, I am deeply grateful to my parents Ayla Tuncer and Raşit Tuncer and my brother Türker Tuncer for their endless support throughout my entire life.

TABLE OF CONTENTS

ABSTRACT v

ÖZ vii

ACKNOWLEDGEMENTS x

TABLE OF CONTENTS xi

LIST OF TABLES xiii

LIST OF FIGURES xv

LIST OF SYMBOLS AND ABBREVATIONS xix

CHAPTERS

1 INTRODUCTION 1

1.1 General 1

1.2 Autoclaved Aerated Concrete 2

1.2.1 Manufacturing Process of Autoclaved Aerated Concrete 2

1.2.2 AAC Structural Elements 3

1.2.3 Material Properties of AAC elements 5

1.2.3.1 Dry Density 6

1.2.3.2 Compressive Strength 6

1.2.3.3 Tensile and Flexural Strength 7

1.2.3.4 Modulus of Elasticity 7

1.3 Fiber Reinforced Polymers (FRPs) 8

1.3.1 Types 8

1.3.2 Physical and Mechanical Properties of FRP 8

1.3.3 Application of FRP in Structural Retrofits 10

1.4 Use of FRPs with AAC 13

1.5 Objectives and Scope 18

1.6 Organization of the Thesis 19

2 EXPERIMENTAL STUDY 21

2.1 General 21
2.2 Material Properties 23
2.3 FRP Bonding 23
2.4 Experimental Setup 24
2.5 Test Specimens 25
2.6 Experimental Results 27
2.6.1 Group-A 28
2.6.2 Group-B 32
2.6.2.1 Group-B1 32
2.6.2.2 Group-B2 36
2.6.3 Group-C 39
2.7 Concluding Remarks 41
3 ANALYTICAL RESULTS 43
3.1 General 43
3.2 Analytical Model 43
3.3 Section Analysis 45
3.4 Validation of the Moment-Curvature Analysis 53
3.5 Load-Displacement Analysis 54
3.6 Comparison of Results 57
3.7 Design 60
4 CONCLUSION 67
4.1 Conclusion 67
REFERENCES 69
APPENDICES
A. STEEL REINFORCED SECTION ANALYSIS 71
B. FIBER REINFORCED SECTION ANALYSIS 91
C. MOMENT-CURVATURE ANALYSIS 97

LIST OF TABLES

TABLES

Table 1.1: Density classes for AAC (EN 12602, 2015) 6

Table 1.2: Compressive strength classes for AAC (EN 12602, 2015) 6

Table 1.3: Typical densities of FRP materials (ACI 440.2R, 2016) 9

Table 1.4: Typical tensile properties of FRP materials (ACI 440.2R, 2016) 9

Table 1.5: Typical thermal expansion coefficient ranges for FRPs (ACI 440.2R, 2016) 10

Table 1.6: Fiber reinforcement types used in the experiment (Memari et al., 2010) . 14

Table 1.7: Experimental test results (Memari et al., 2010) 14

Table 1.8: Critical scaled distances of test specimens (Wang et al., 2017) 16

Table 1.9: Comparison of analytical modeling and experimental results for UFFS panel type (Mousa and Uddin, 2009) 18

Table 1.10: Comparison of analytical modeling and experimental results for BFFS panel types (Mousa and Uddin, 2009) 18

Table 2.1: Mechanical properties of AAC 23

Table 2.2: Mechanical properties of steel 23

Table 2.3: Mechanical properties of FRPs 23

Table 2.4: Properties of the specimens used in the experiment 26

Table 2.5: Group A specimens 26

Table 2.6: Group B specimens 27

Table 2.7: Group C specimens 27

Table 2.8: Definition of test parameters 28

Table 2.9: Summary table for Group-A specimens 32

Table 2.10: Summary table for Group-B1 specimens 35
Table 2.11: Summary table for Group-B2 specimens 38
Table 2.12: Summary table for Group-C specimens 41
Table 3.1: Failure modes used in moment-curvature diagrams 52
Table 3.2: Critical locations used in load-displacement curves 55
Table 3.3: Abbreviations used in curvature diagrams 56
Table 3.4: The comparison of recommended debonding strain with ACI 440 61
Table 3.5: Design charts for composite specimens 63

LIST OF FIGURES

FIGURES

Figure 1.1: Production process of AAC (Hamad, 2014)..... 3

Figure 1.2: Porous structure of AAC (Schober, 2011) 3

Figure 1.3: Different samples of AAC products (Matthys and Barnett, 2004)..... 4

Figure 1.4: The main usage areas of AAC elements..... 4

Figure 1.5: Bond between concrete and reinforcement 5

Figure 1.6: Typical building erection..... 5

Figure 1.7: Fiber schemes for reinforced concrete beam specimens (Norris et al., 1997).....11

Figure 1.8: Confining of RC columns with CFRP (Ozcan, 2009)..... 11

Figure 1.9: Beam-column joint strengthened by L-shaped FRP (Yu et al., 2016) 12

Figure 1.10: CFRP anchor bonding to hollow clay tile specimen (Camlı, 2005)..... 12

Figure 1.11: Strengthening of brick infilled walls with CFRP strips (Akın, 2011)... 13

Figure 1.12: Steel reinforcement sketches of test specimen types (Memari et al., 2010).....14

Figure 1.13: Explosion experimental setup (Wang et al., 2017)..... 15

Figure 1.14: Reinforcement sketches of AAC panels (Wang et al., 2017)..... 15

Figure 1.15: CFRP wrapping schemes (Wang et al., 2017)..... 16

Figure 1.16: Layout of fiber composites (Mousa and Uddin, 2009)..... 17

Figure 1.17: Load-displacement comparison of panel types (Mousa and Uddin, 2009).....17

Figure 1.18: Failure mode of specimens (Mousa and Uddin, 2009)..... 17

Figure 2.1: Specimen cross section properties..... 22

Figure 2.2: Composite AAC beam production 24
Figure 2.3: Loading setup and data acquisition system 25
Figure 2.4: Idealized experimental loading scheme 25
Figure 2.5: Typical load-displacement curve 27
Figure 2.6: Test setup of Group-A specimens 28
Figure 2.7: Group-A specimen dimensions 29
Figure 2.8: Load-displacement curves for Group-A specimens 30
Figure 2.9: Failure modes of Group-A specimens 32
Figure 2.10: Test setup of Group-B1 specimens 33
Figure 2.11: Group-B1 specimen dimensions 33
Figure 2.12: Load-displacement curves for Group-B1 specimens 33
Figure 2.13: Failure modes of Group-B1 specimens 35
Figure 2.14: Test setup of Group-B2 specimens 36
Figure 2.15: Group-B2 specimen dimensions 36
Figure 2.16: Load-displacement curves for Group-B2 specimens 37
Figure 2.17: Failure modes of Group-B2 specimens 38
Figure 2.18: Experimental setup of Group-C specimens 39
Figure 2.19: Group-C specimen dimensions 39
Figure 2.20: Load-displacement curves for Group-C specimens 40
Figure 2.21: Failure modes of Group-C specimens 41
Figure 3.1: AAC stress-strain model inspired from Hognestad (1951) 44
Figure 3.2: Stress-strain model for elastic-perfectly plastic steel 44
Figure 3.3: Stress-strain model for FRP 45
Figure 3.4: Section analysis for uncracked section 46
Figure 3.5: Section analysis for cracked section 46
Figure 3.6: Stress-strain profile for steel yielding (ascending portion) 47

Figure 3.7: Stress-strain profile for steel yielding (descending portion) 47

Figure 3.8: Stress-strain profile at which $\varepsilon_{ctop} = \varepsilon_{co}$ (steel reinforced sections) 49

Figure 3.9: Stress-strain profile at which $\varepsilon_{ctop} = \varepsilon_{co}$ (FRP reinforced sections) 49

Figure 3.10: Stress-strain profile for AAC crushing (steel reinforced sections)..... 50

Figure 3.11: Stress-strain profile for AAC crushing (FRP reinforced sections)..... 50

Figure 3.12: Stress-strain profile for FRP debonding (ascending portion)..... 51

Figure 3.13: Stress-strain profile for FRP debonding (descending portion)..... 51

Figure 3.14: Typical moment-curvature curve for steel reinforced sections 52

Figure 3.15: Typical moment-curvature curve for FRP reinforced sections 52

Figure 3.16: Material properties of reference specimens..... 53

Figure 3.17: Reinforcement configurations of the reference specimens..... 53

Figure 3.18: Moment-curvature comparison based on SAP2000 and analytical modeling for steel reinforced specimens 54

Figure 3.19: Typical load-displacement curve for steel-reinforced sections 55

Figure 3.20: Typical load-displacement curve for fiber-reinforced sections..... 55

Figure 3.21: Curvature diagram for steel and FRP reinforced specimens 56

Figure 3.22: Comparison of load-displacement relation between the experimental results and analytical model for reference specimens..... 57

Figure 3.23: Comparison of load-displacement relation between the experimental results and analytical model for composite specimens 58

Figure 3.24: Average strain values for different fiber applications 61

Figure 3.25: Loading system for design charts..... 63

Figure A.1:Section analysis for prior to cracking case 71

Figure A.2: Section analysis for prior to cracking case 72

Figure A.3: Section analysis for after cracking case..... 72

Figure A.4: Section analysis for after cracking case..... 73

Figure A.5: Stress-strain profile for steel yielding case..... 74

Figure A.6: Stress-strain profile for steel yielding case 78

Figure A.7: Geometric center of ascending and descending portion of concrete stress block..... 78

Figure A.8: Stress-strain profile at which $\boldsymbol{\varepsilon = \varepsilon_{co}}$ 81

Figure A.9: Stress-strain profile for AAC crushing 86

Figure B.1: Section analysis for prior to cracking case..... 91

Figure B.2: Section analysis for after cracking case 92

Figure B.3: Stress-strain profile at which $\boldsymbol{\varepsilon = \varepsilon_{co}}$ 92

Figure B.4: Stress-strain profile for AAC crushing 93

Figure B.5: Stress-strain profile for FRP debonding..... 94

Figure B.6: Stress-strain profile for FRP debonding..... 95

Figure C.1: Moment-curvature relation for Group-A specimens..... 97

Figure C.2: Moment-curvature relation for Group-B specimens 98

Figure C.3: Moment-curvature relation for Group-C specimens 98

LIST OF SYMBOLS AND ABBREVIATIONS

ABBREVIATIONS

AAC	Autoclaved Aerated Concrete
AFRP	Aramid Fiber Reinforced Polymer
ACI	American Concrete Institute
BCRAP	Bidirectional CFRP Reinforced AAC Panel
BFFS	Biaxial FRP for Flexure and Shear Reinforcement
CFRP	Carbon Fiber Reinforced Polymer
EN	European Norms
FC	Full Carbon
FG	Full Glass
FRP	Fiber Reinforced Polymer
GFRP	Glass Fiber Reinforced Polymer
HC	Half Carbon
N.A	Neutral axis in the stress-strain profile of the section
PAP	Plain AAC Panel
RAP	Reinforced AAC Panel
RC	Reinforced Concrete
TS	Turkish Standards
S	Steel
UCRAP	Unidirectional CFRP Reinforced AAC Panel
UCPAP	Unidirectional CFRP Plain AAC Panel

UFFS	Uniaxial FRP for Flexure and Shear Reinforcement

SYMBOLS

a	Distance from load application point to the support
A_{frp}	Area of bottom fiber layer
$A_{frp'}$	Area of top fiber layer
A_i	The area of i^{th} region under the moment-curvature diagram
A_s	Area of top bottom steel
$A_{s'}$	Area of top steel
b	Section width
c	Neutral axis depth measured from top of the section
d	Distance measured from bottom steel to top of the section
d'	Distance measured from top steel to top of the section
D	Anchored rebar diameter
E	Energy absorption capacity
E_c	Modulus of elasticity of AAC
E_{cm}	Mean modulus of elasticity of AAC
E_{frp}	Modulus of elasticity of FRP
E_{Pmax}	Energy absorption capacity enclosed by the area between the origin and P_u-Δ under load-displacement curve
E_s	Modulus of elasticity of steel
EI_{eff}	Effective flexural rigidity
f_c'	Compressive strength of AAC

$f_{cflk};0,05$	Characteristic value of 5%- quantile of flexural tensile strength of AAC
$f_{cflk};0,95$	Characteristic value of 95%- quantile of flexural tensile strength of AAC
f_{ck}	Uniaxial characteristic compressive strength of AAC
$f_{ctk};0,05$	Characteristic value of 5%- quantile of direct tensile strength of AAC
$f_{ctk};0,95$	Characteristic value of 95%- quantile of direct tensile strength of AAC
$f_{ctf,d}$	Flexural design tensile strength of AAC
$f_{ctf,k}$	Flexural characteristic tensile strength of AAC
F_c	Total force due to AAC
F_{c1}	Force due to AAC (ascending portion of Hognestad curve)
F_{c2}	Force due to AAC (descending portion of Hognestad curve)
F_{fe}	Force due to bottom fiber
$F_{fe'}$	Force due to top fiber
F_s	Force due to bottom steel
F_s'	Force due to top steel
f_{yd}	Yield strength of steel
h	Section height
H	Beam height
I_{cr}	Moment of inertia of the cracked section
I_{tr}	Moment of inertia of the transformed section

K_s	Secant stiffness
l_b	Development length of anchored rebar
L	Beam length
L_n	Clear span length
M	Moment
M_{cr}	Moment at which specimen cracks
M_o	Moment at which f_c' becomes maximum
M_u	Moment at which specimen fails (AAC crushing/ FRP debonding)
M_y	Moment at which steel yields
n	Modular ratio (E_s/ E_c or E_{frp}/ E_c)
n_{frp}	Fiber layer number
P_u	Ultimate load capacity
q	Uniform distributed load that causes the same moment due to maximum point load given in the test data
q_{all}	Allowable load capacity of FRP bonded specimen
$t_{A/C}$	Tangential deviation of point A with respect to point C
$t_{B/C}$	Tangential deviation of point B with respect to point C
t_{frp}	Fiber layer thickness
T	Tensile force of anchored rebar
U	Prior to cracking (failure mode)
v	Distance from the support to the beam outer face
V	After cracking (failure mode)
w_b	Beam width

w_{frp}	Fiber width
W	Beam width
X	Maximum AAC compressive strength (failure mode)
$\bar{y}$	Distance measured from bottom of the section
$\overline{y1}$	Centroid of AAC force (ascending portion of Hognestad curve)
$\overline{y2}$	Centroid of AAC force (descending portion of Hognestad curve)
Y	Steel yielding (failure mode)
Z	AAC crushing (failure mode)
Z'	AAC crushing or FRP debonding (failure mode)
α	Prior to cracking (failure mode)
β	After cracking (failure mode)
γ	Steel yielding (failure mode)
γ_M	Material factor for AAC
Δ	Maximum displacement at the mid-span
Δ_{cr}	Cracking displacement
Δ_u	Ultimate displacement
Δ_y	Yield displacement
ΔL	Displacement limit under serviceability limit state
ε_{cfrp}	Recommended debonding strain CFRP bonded specimens
ε_{co}	Strain at which AAC reaches maximum compressive strength
ε_{ctop}	AAC strain at the extreme compression fiber
ε_{cu}	Crushing strain of AAC
ε_{fd}	Bottom fiber debonding strain

ε_{fe}	Bottom fiber strain
ε_{fe}'	Top fiber strain
ε_{fu}	Ultimate strain of FRP
ε_{gfrp}	Recommended debonding strain for GFRP bonded specimens
ε_{s}	Bottom steel strain
ε_{s}'	Top steel strain
ε_{sy}	Steel yield strain
ε_{u}	Ultimate strain of FRP
λ	Maximum AAC compressive strength (failure mode)
μ	Ductility
ρ_{m}	Dry density of AAC
σ_{c}	AAC compressive strength
σ_{s}	Bottom steel strength
σ_{s}'	Top steel strength
σ_{u}	Ultimate strength of FRP
σ_{y}	Yield strength
τ	Bond shear strength of anchored rebar
Ø	Curvature of the section
$Ø_{cr}$	Curvature for uncracked /cracked case
$Ø_{cr,after}$	Curvature for after cracking case
$Ø_{cr,before}$	Curvature for prior to cracking case
$Ø_{o}$	Curvature at which $\varepsilon_{ctop} = \varepsilon_{co}$

$Ø_u$	Curvature at which AAC crushes or FRP debonds
$Ø_y$	Curvature at which steel yields
ψ	AAC crushing (failure mode)
ω	AAC crushing or FRP debonding (failure mode)

CHAPTER 1

INTRODUCTION

1.1 General

Autoclaved Aerated Concrete (AAC) has been one of the most important construction materials used for residential and commercial buildings, hospitals and schools since the first commercially produced AAC in Sweden in 1923. From this date, AAC production spread to many countries and it has been used as non-structural and structural elements in the construction sector all over the world (Chaipanich and Chindaprasirt, 2015). The reasons behind this popularity are its superior insulation properties, possibility of manufacturing in accurate sizes, being lightweight and fire resistant, speed of construction and economy of final products (Alakoc, 1999). Furthermore, it is well known that seismic loads are directly proportional to the weight of the structures and earthquake forces on AAC buildings are expected to be significantly smaller compared to the similar height reinforced concrete buildings.

Starting from the 20^{th} century, strengthening and retrofitting of existing structures have been an important need for the aging infrastructure and deficient structures. In order to increase the load carrying capacity, stiffness, deformability and to improve the weak zones of existing concrete structural members, many different techniques were proposed. Fiber Reinforced Polymer (FRP) applications emerged as an alternative to many traditional retrofitting techniques such as external bonded steel plates, steel or concrete jackets since 1980s. FRP bonding technology was firstly performed at the Swiss Federal Laboratory for Materials Testing and Research in 1984 (Teng et al., 2002). The high strength to weight ratio, resistance against corrosion and high tensile strength of FRPs make them attractive alternatives for such retrofit application.

Using FRPs together with AAC can provide lighter, corrosion resistant, economically feasible load bearing elements in terms of workmanship, which can be produced at higher speeds compared to steel reinforced AAC elements. The available research on the testing and design of such elements are described in the next sections. It will be demonstrated that there are only limited number of studies investigating the behavior of FRP reinforced AAC beams. Hence, further studies are needed to enable the combination of these two “extremes,” i.e. AAC as a lightweight, low strength, high insulation, fire resistant material and FRP as a high strength product.

1.2 Autoclaved Aerated Concrete

1.2.1 Manufacturing Process of Autoclaved Aerated Concrete

AAC is a lightweight cellular material. It is mainly composed of silica (or quartz sand), lime, Portland Cement and aluminum powder. In the production stage, firstly, silica or quartz sand and lime are mixed with cement, then water is added to initiate the hydration reaction. After this mixture, aluminum powder is added as an expansion agent. In this way, mixture volume is increased up to 2 to 5 times of its original volume and a porous texture is obtained (Figure 1.2). Reaction of aluminum powder with calcium hydroxide creates air bubbles providing the cellular structure, while hydrogen evaporates from the mixture. Before the curing process, material is cut by means of steel wires to required sizes and shapes. Then, the specimens are cured in the chamber under high pressure (40-160 bar) and temperature (121-124 °C) for 8-12 hours. This curing process is named as "autoclaving". After curing, the specimens are packaged and they are ready to be transported to the construction site. Production steps are schematically explained in Figure 1.1.

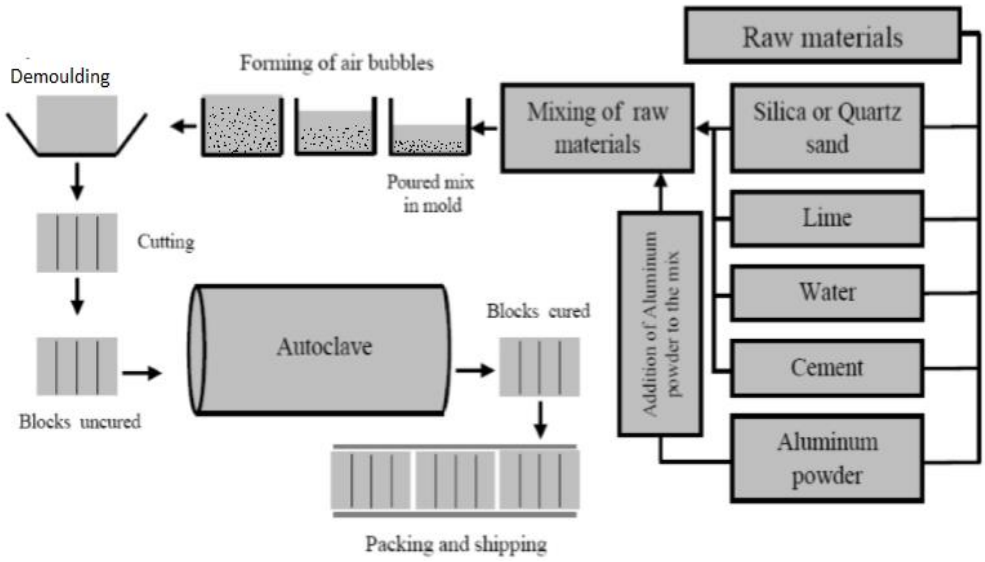

Figure 1.1: Production process of AAC (Hamad, 2014)

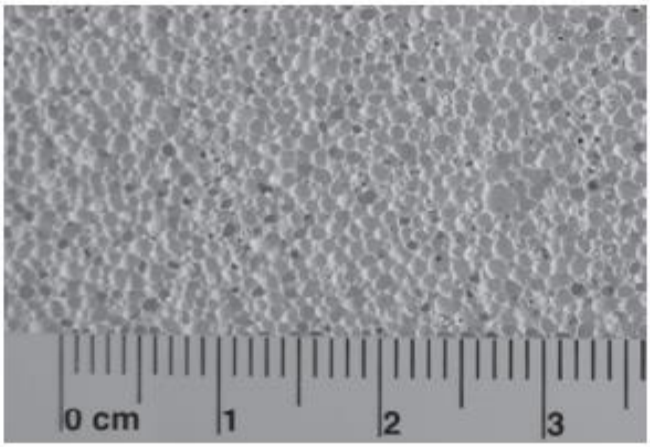

Figure 1.2: Porous structure of AAC (Schober, 2011)

1.2.2 AAC Structural Elements

AAC is commonly utilized as interior, exterior load bearing or non-bearing walls in buildings. They can be devised as wall, floor or roof panels and lintels in the building construction. They are available in many shapes as shown in Figure 1.3 and Figure 1.4. Typical AAC blocks are 60 cm in length and 25 cm in width, whereas the thickness varies from 5 cm to 35 cm depending on the desired insulation characteristics. For the panel types of AAC, maximum length and typical width of the elements are usually 600 cm and 60 cm, respectively. Panel thicknesses may be between 10 cm and 30 cm.

Since AAC is weak in tension compared to its compressive strength similar to concrete, reinforcement is needed to carry tensile forces and to resist bending moments in wall panels, slabs or lintels. Reinforcing bars in the form of welded wire mesh are commonly used in AAC elements. The bond between AAC and the reinforcement is provided through the bearing action of the transverse reinforcement welded to the longitudinal reinforcement as shown in Figure 1.5. An AAC building constructed by using different AAC elements is visualized in Figure 1.6. In addition to buildings, AAC products are also used in steel and RC construction as infill walls, lintels, roofs and slab panels. It can be observed that reinforced wall panels and slab panels are connected through reinforced concrete bond beams. Non-bearing walls are constructed with AAC blocks. Lintels are used over the door and windows to carry the loads imposed from wall blocks.

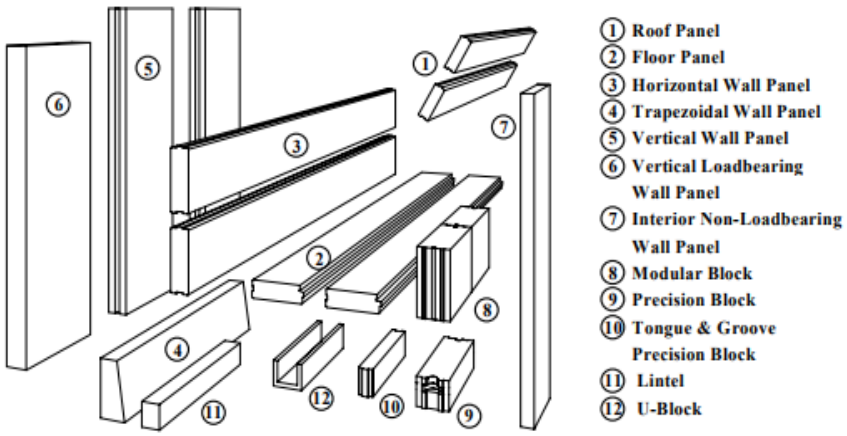

Figure 1.3: Different samples of AAC products (Matthys and Barnett, 2004)

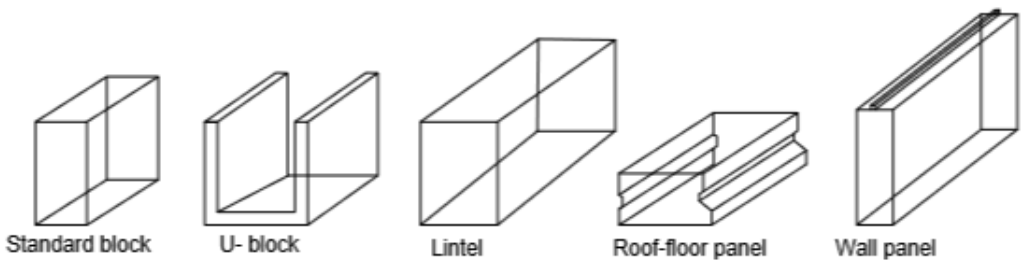

Figure 1.4: The main usage areas of AAC elements

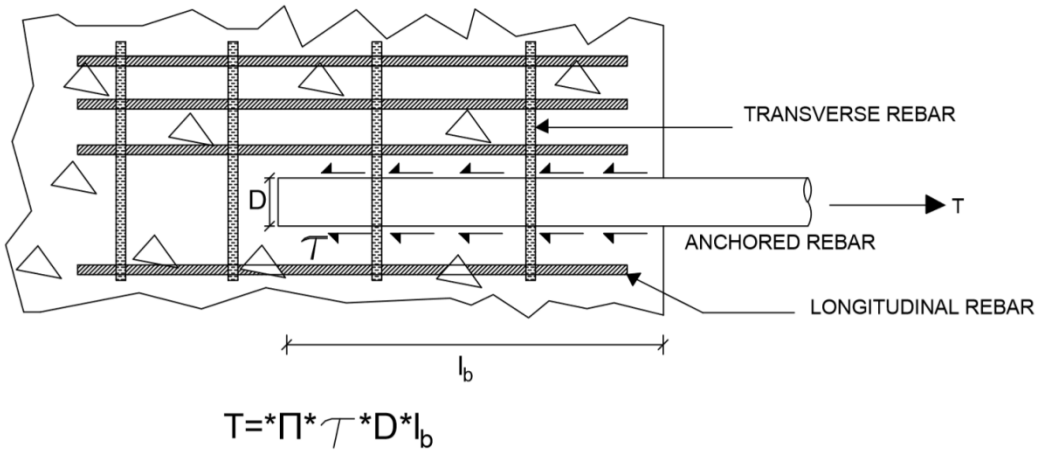

Figure 1.5: Bond between concrete and reinforcement

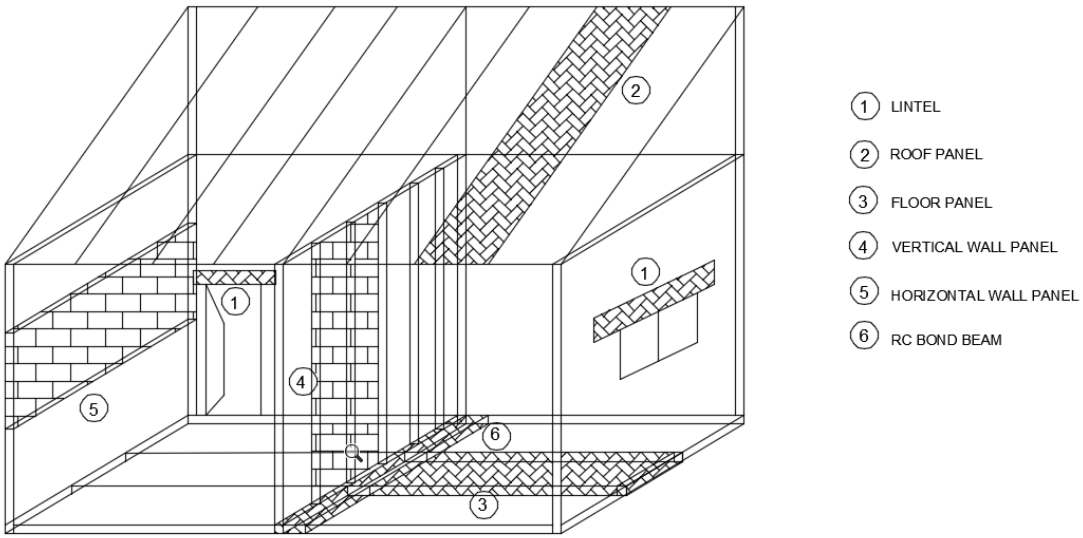

Figure 1.6: Typical building erection

1.2.3 Material Properties of AAC elements

European Standard EN 12602:2015 “Prefabricated Reinforced Components of Autoclaved Aerated Concrete” and TS EN 845-2 "Specification for Ancillary Components for Masonry-Part 2:Lintels" are the available guidelines in Turkey and Europe to design and test reinforced AAC panels. Material properties of AAC as described in that document are summarized below.

1.2.3.1 Dry Density

Dry density ranges for different classes are provided in Table 1.1. It can be observed that AAC can be as light as 250 kg/m^3 which is about one tenth of the concrete density. Due to the moisture penetration, the actual density of AAC is usually around 30% higher.

Table 1.1: Density classes for AAC (EN 12602, 2015)

Density class	**300**	**350**	**400**	**450**	**500**	**550**	**600**	**650**
ρ_m (kg/m^3)	>250 ≤300	>300 ≤350	>350 ≤400	>400 ≤450	>450 ≤500	>500 ≤550	>550 ≤600	>600 ≤650
Density class	**700**	**750**	**800**	**850**	**900**	**950**	**1000**	
ρ_m (kg/m^3)	>650 ≤700	>700 ≤750	>750 ≤800	>800 ≤850	>850 ≤900	>900 ≤950	>950 ≤1000	

1.2.3.2 Compressive Strength

Characteristic compressive strengths and their corresponding strength classes are provided in Table 1.2.

Table 1.2: Compressive strength classes for AAC (EN 12602, 2015)

Strength class	**AAC 1,5**	**AAC 2**	**AAC 2,5**	**AAC 3**	**AAC 3,5**
f_{ck} (MPa)	1,5	2	2,5	3	3,5
Strength class	**AAC 4**	**AAC 4,5**	**AAC 5**	**AAC 6**	**AAC 7**
f_{ck} (MPa)	4	4,5	5	6	7
Strength class	**AAC 8**	**AAC 9**	**AAC 10**		
f_{ck} (MPa)	8	9	10		

1.2.3.3 Tensile and Flexural Strength

When experimental results are not available, the following equations are recommended to estimate tensile strength. According to EN 12602 (2015), direct tensile strength and flexural strength values are obtained by using either 5% or 95% probabilistic frequencies.

$$f_{ctk;0,05} = 0,10\ f_{ck} \quad (1.1)$$

$$f_{ctk;0,95} = 0,24\ f_{ck} \quad (1.2)$$

$$f_{cflk;0,05} = 0,18\ f_{ck} \quad (1.3)$$

$$f_{cflk;0,95} = 0,36\ f_{ck} \quad (1.4)$$

where:

$f_{ctk;0,05}$ is the characteristic value of 5%- quantile of direct tensile strength

$f_{ctk;0,95}$ is the characteristic value of 95%- quantile of direct tensile strength

$f_{cflk;0,05}$ is the characteristic value of 5%- quantile of flexural tensile strength

$f_{cflk;0,95}$ is the characteristic value of 95%- quantile of flexural tensile strength

f_{ck} is the uniaxial characteristic compressive strength

1.2.3.4 Modulus of Elasticity

In the absence of experimental data, specification suggests that modulus of elasticity can be determined by Equation 1.5.

$$E_{cm} = 5\ (\rho_m - 150) \quad (1.5)$$

where E_{cm} is the mean modulus of elasticity in MPa

1.3 Fiber Reinforced Polymers (FRPs)

1.3.1 Types

FRP composites are produced by embedding fibers in a resin matrix. The main components of FRPs are therefore the resin and the fibers. Resin is used to increase the adhesion between concrete and fiber laminates, resist against environmental factors and provide workability. Fibers play the important role of providing tensile strength. FRPs are mainly used to improve or repair the weakened part of structural members by increasing moment and/or shear capacity in existing structure. Although carbon fiber reinforced polymers (CFRP) are the most commonly used material in the market due to their high strength, glass fiber reinforced polymers (GFRP) and aramid fiber reinforced polymers (AFRP) are also available as other economical and durable alternatives, respectively. In addition to fiber and resin components, adhesives provide the bonding action between concrete and fiber. The most common methods of FRP production are named as "wet layup", "prepreg", "precured" and "near-surface-mounted" systems.

1.3.2 Physical and Mechanical Properties of FRP

Mechanical properties of FRPs and design using fiber composites are given in the American Standard ACI 440.2R-16 “Design and Construction of Externally Bonded FRP Systems”. Apart from explanations of material features, chemical compositions and manufacturing process; this specification is a comprehensive design handbook for engineers designing FRPs.

Fiber density is influenced by several factors such as production method, resin type, environmental condition. In Table 1.3, typical density ranges for different FRP types are given. In this table, density of fibers are compared with steel, as well.

Tensile strength of FRP composites are several times higher than steel. Typical values of tensile strength and modulus of elasticity are presented in Table 1.4. Upon combining with a less strong but deformable resin, the apparent tensile strength of the FRP composite reduces to about 30 to 90 % of the fiber strength.

Table 1.3: Typical densities of FRP materials (ACI 440.2R, 2016)

Steel (t/m^3)	**GFRP (t/m^3)**	**CFRP (t/m^3)**	**AFRP (t/m^3)**
7.9	1.2 to 2.1	1.5 to 1.6	1.2 to 1.5

Table 1.4: Typical tensile properties of FRP materials (ACI 440.2R, 2016)

Fiber type	**Elasticity Modulus (GPa)**	**Ultimate strength (MPa)**	**Rupture strain, %**
Carbon			
General purpose	220 to 240	2050 to 3790	1.2
High strength	220 to 240	3790 to 4820	1.4
Ultra high strength	220 to 240	4820 to 6200	1.5
High modulus	340 to 520	1720 to 3100	0.5
Ultra high modulus	520 to 690	1380 to 2400	0.2
Glass			
E-glass	10 to 10.5	1860 to 2680	4.5
S-glass	12.5 to 13	3440 to 4140	5.4
Aramid			
General purpose	10 to 12	3440 to 4140	2.5
High performance	16 to 18	3440 to 4140	1.6

As followed from Table 1.5, thermal expansion coefficient may exhibit changes in the longitudinal and transverse directions with respect to the fiber orientation, resin type, volumetric fraction of constituents. Also, AFRP and CFRP behave opposite to the common sense in longitudinal direction under temperature increase as indicated in Table 1.5. In other words, as opposed to commonly known material response, while temperature increase causes fiber contraction, expansion is observed when temperature is reduced. The reason behind this extraordinary result is the fact that AFRP and CFRP are composed of orthotropic polymeric matrices where GFRP shows isotropic behavior due to its nature (Nanni et al., 2014).

Table 1.5: Typical thermal expansion coefficient ranges for FRPs (ACI 440.2R, 2016)

Direction	**GFRP (x10^{-6}/°C)**	**CFRP (x10^{-6}/°C)**	**AFRP (x10^{-6}/°C)**
Longitudinal	6 to 10	-1 to 0	-6 to -2
Transverse	19 to 23	22 to 50	60 to 80

1.3.3 Application of FRP in Structural Retrofits

It is not aimed to provide all the literature on the use of FRPs in RC member strengthening in this section. Some examples are provided herein to give an idea about the available applications. The performance of structural members can be improved in flexure and/or shear by using FRPs. While flexural strengthening is mainly provided by applying externally bonded fiber strips in the tension zone of members, some techniques such as side bonding, U-jacketing and wrapping are implemented to obtain higher shear capacity. In structural engineering, FRPs are primarily used in reinforced concrete columns, beams, beam-column joints and infill walls. Comprehensive explanations related to FRP strengthening methods are available for the structural members including beams, slabs and columns (Teng et al., 2002).

Norris et.al (1997) performed several tests on reinforced concrete beams strengthened with CFRP in tension side and web zone (Figure 1.7) under four point bending to investigate the effect of fiber orientation to load capacity and ductility. Although CFRP sheet increased the strength and stiffness for all specimens, fiber orientation determined the degree of this improvement. The increase in strength and stiffness was more for the specimens having the fibers orthogonally oriented to the cracks, however, brittle failure was observed due to concrete crushing. When fibers were placed at an angle to the expected cracks, it was seen that capacity would slightly increase and a more ductile behavior would be obtained.

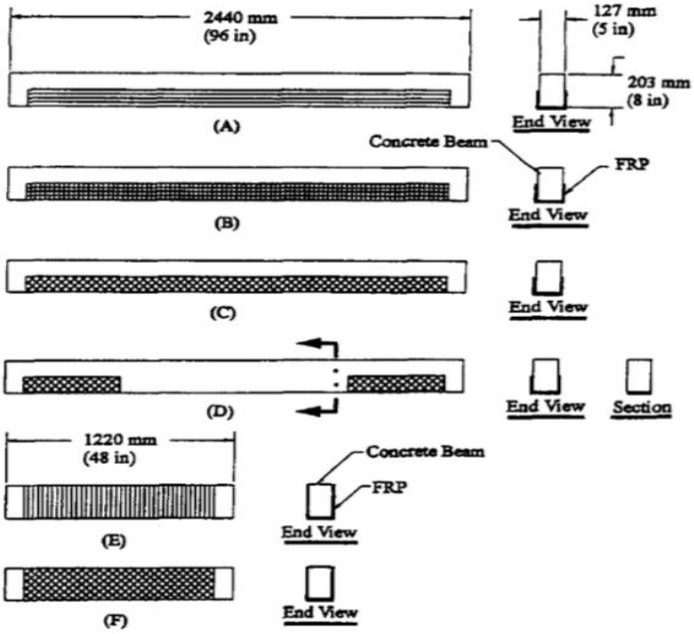

Figure 1.7: Fiber schemes for reinforced concrete beam specimens (Norris et al., 1997)

Ozcan (2009) carried out experiments on columns having inadequate transverse reinforcements and low strength concrete under the action of constant axial load and cyclic lateral displacement demands to investigate the effect of CFRPs on ductility. He observed that ductility and energy dissipation capacity were significantly increased by confining the plastic hinge zones of columns with CFRP sheets as seen in Figure 1.8. As opposed to this, the improvement in lateral load capacity was not significant relative to the ductility and energy dissipation.

Figure 1.8: Confining of RC columns with CFRP (Ozcan, 2009)

Most of the damage in reinforced concrete structures during earthquakes were mainly caused from insufficient reinforcements at beam-column joints. Yu et al. (2006) conducted tests for such joints to observe the effect of externally bonded L-shaped CFRP and GFRP (as shown in Figure 1.9) and to improve the behavior of seismic performance. According to those test results, while deformation capacity was significantly enhanced for both types of fibers, the increase in strength was more significant for CFRP laminates due to their higher strength. In this way, plastic hinge was shifted to the beam ends to meet flexural failure mode under simulated earthquake loads.

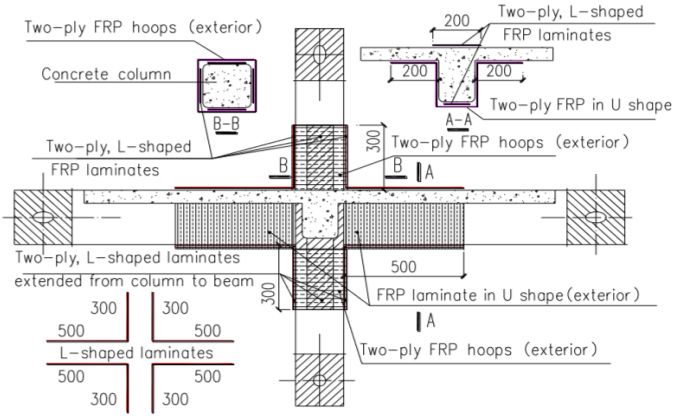

Figure 1.9: Beam-column joint strengthened by L-shaped FRP (Yu et al., 2016)

Camlı (2005) conducted double shear test experiments that measure the bond strength of CFRP anchors bonded to concrete and hollow clay tile masonry specimens as seen in Figure 1.10. He found out that embedded type CFRP anchors can significantly improve the load capacity of the specimens. Also, when bonding was on the plastered surfaces, it was seen that capacity was higher since plaster provided additional adherence between anchor and specimen.

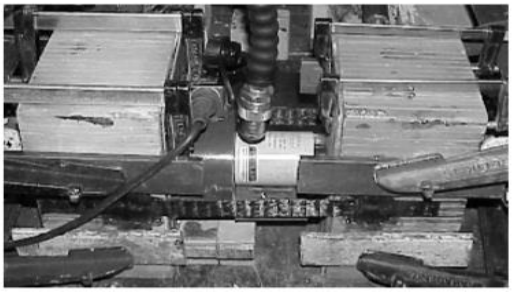

Figure 1.10: CFRP anchor bonding to hollow clay tile specimen (Camlı, 2005)

Akın (2011) implemented diagonal CFRP strips to brick infill walls and established a new lateral load resisting system that are composed of existing structural frame integrated to the FRP strengthened hollow clay tile infill walls (Figure 1.11). According to the test results; ductility, initial stiffness of the frames, story drift capacities of the specimens were significantly increased by integrating infill walls into existing frame.

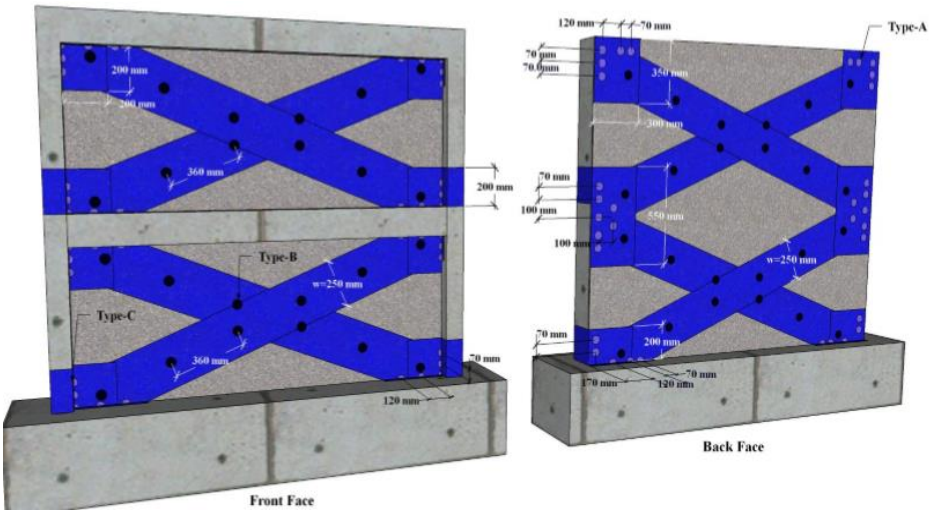

Figure 1.11: Strengthening of brick infilled walls with CFRP strips (Akın, 2011)

1.4 Use of FRPs with AAC

As stated in the first sections, studies including AAC with FRPs are very limited. In this part, available studies in the literature are presented.

Memari et al. (2010) employed four-point loading system to test FRP bonded beams. In the experimental series, tests were performed on reinforced concrete and AAC beams. While all the test samples had flexural and shear reinforcements, some of them were bonded with the application of GFRP for flexure and/or shear strength enhancement (Figure 1.12 and Table 1.6). The effects of clear length, flexural/shear reinforcement and fiber configuration and cross-sectional dimensions of the specimens on load capacity were investigated. According to the test results given in Table 1.7, it is clear that Type C reinforcement application mostly increased the load carrying capacities of the specimens. This table also indicates that shear failure was observed for all the specimens having Type C reinforcement layout.

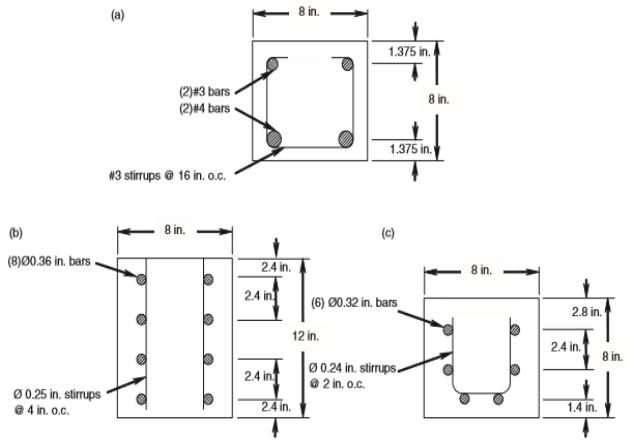

Figure 1.12: Steel reinforcement sketches of test specimen types (Memari et al., 2010)

Table 1.6: Fiber reinforcement types used in the experiment (Memari et al., 2010)

FRP reinforcement	FRP details
Type A: No FRP reinforcement	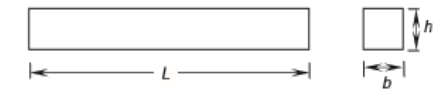
Type B: Flexural reinforcement at the bottom face only	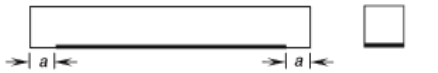
Type C: Flexural reinforcement at bottom face and U-wrap shear reinforcement at each end	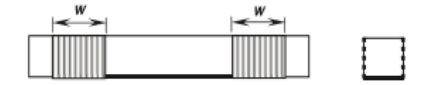
Type U: U-wrap along the length for flexural reinforcement	
Type F: Full-wrap along the length for shear reinforcement	

Dimensions, mm (in.):
L = 1020 (40), 1320 (52), 1630 (64), or 1930 (76);
b = 203 (8);
h = 203 (8) or 305 (12);
w = 305 (12);
a = 102 (4).

Table 1.7: Experimental test results (Memari et al., 2010)

Beam	Max. total load, kN (kip)	Avg. ult. load per cylinder, kN (kip)	Increased capacity (%)	Midspan deflection at peak load, mm (in.)	Failure mode
AAC4-A	89.51 (20.12)	44.75 (10.06)	–	5.5 (0.22)	Shear
AAC4-B	100.87 (22.68)	50.44 (11.34)	13	7.4 (0.29)	Shear
AAC4-C	118.29 (26.59)	59.15 (13.30)	32	8.4 (0.33)	Shear
AAC5-A	72.12 (16.21)	36.06 (8.11)	–	9.4 (0.37)	Shear
AAC5-B	78.39 (17.62)	39.19 (8.81)	9	8.4 (0.33)	Shear
AAC5-C	105.50 (23.72)	52.75 (11.86)	46	12.0(0.47)	Shear
AAC6-A	68.59 (15.42)	34.29 (7.71)	–	12.2 (0.48)	Flexural-Shear
AAC6-B	79.22 (17.81)	39.61 (8.91)	16	6.6 (0.26)	shear
AAC6-C	76.53 (17.20)	38.26 (8.60)	12	9.3 (0.37)	Shear
AAC7-A	46.54 (10.46)	23.27 (5.23)	–	11.5 (0.45)	Flexural
AAC7-B	62.41 (14.03)	31.21 (7.02)	34	13.6 (0.53)	Shear
AAC7-C	66.28 (14.90)	33.15 (7.45)	42	12.5 (0.49)	Shear

Wang et al. (2017) conducted blast experiments to investigate the structural performance of AAC panels under pulse type loading. Figure 1.13 indicates the explosion experimental setup. In this study, five types of specimens including unreinforced/reinforced AAC panels, unreinforced/ reinforced AAC panels bonded with CFRP in unidirectional configuration and reinforced AAC panels bonded with CFRP in bidirectional scheme were tested (Figure 1.14 and Figure 1.15). At the end of experiments, critical scaled distance ranges that measure the explosion resistance were obtained for all test samples as illustrated in Table 1.8. In the light of this table, specimens bonded with bidirectional FRPs showed superior resistance to blast damage due to smaller critical scaled distances compared to the others.

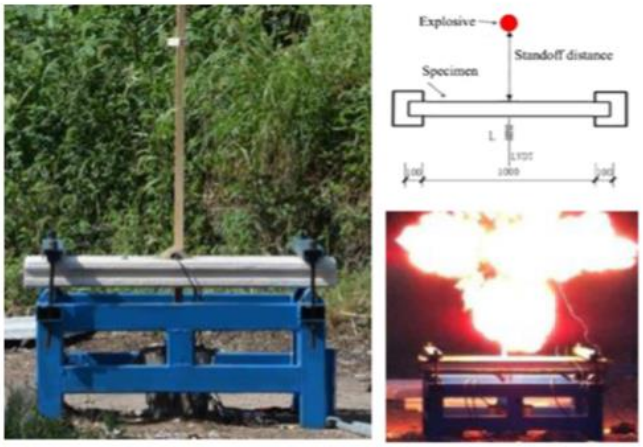

Figure 1.13: Explosion experimental setup (Wang et al., 2017)

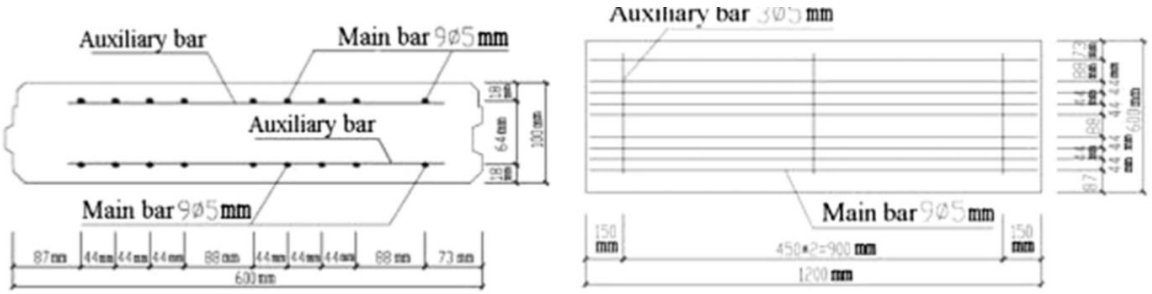

Figure 1.14: Reinforcement sketches of AAC panels (Wang et al., 2017)

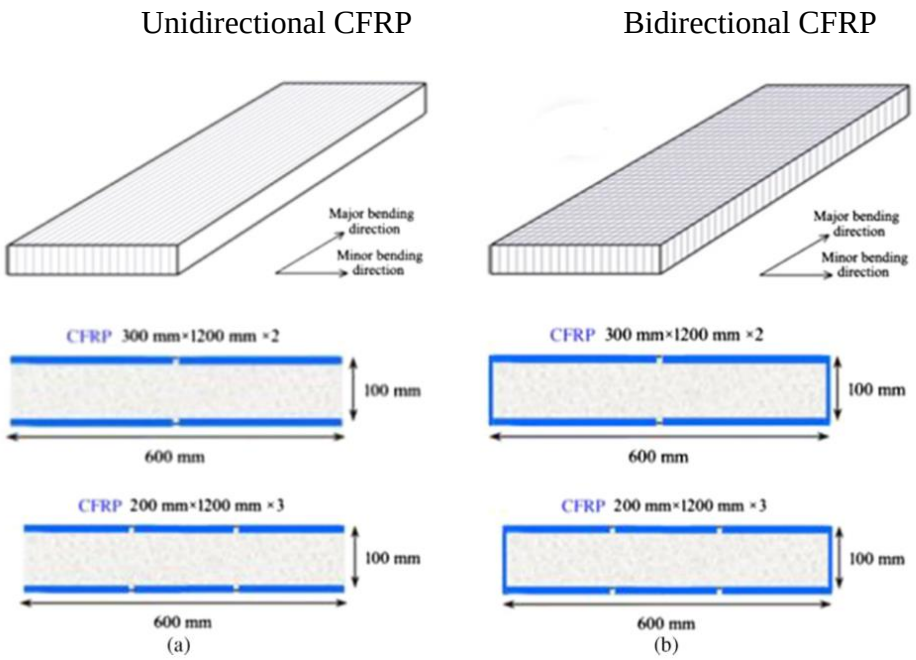

Figure 1.15: CFRP wrapping schemes (Wang et al., 2017)

Table 1.8: Critical scaled distances of test specimens (Wang et al., 2017)

Panel	Reinforced	CFRP	Critical scaled distance (m/kg$^{1/3}$)
PAP	No	No	3.257–2.714
RAP	Yes	No	1.723–1.506
UCPAP	No	Yes	1.723–1.506
UCRAP	Yes	Yes	1.506–1.368
BCRAP	Yes	Yes	0.862–0.684

Mousa and Uddin (2009) carried out a study that aimed to compare moment capacities determined as per the ultimate limit state assumptions and acquired via experiments for CFRP-AAC sandwich panels having the clear span length of 1.2 m under the action of four-point loading. All the test specimens had the same cross-sectional dimensions and clear lengths. The only variable was the fiber scheme (Figure 1.16). Those laboratory studies pointed out that FRPs were successful in providing moment capacity. Since unidirectional CFRP specimens had higher elasticity modulus, smaller deflection was measured relative to the bidirectional CFRP specimens as can be understood from Figure 1.17. Failure modes were shear and flexure for unidirectional and bidirectional CFRPs, respectively (Figure 1.18). Apart from these, a good agreement was obtained between experimental results and theoretical calculations (Table 1.9 and Table 1.10).

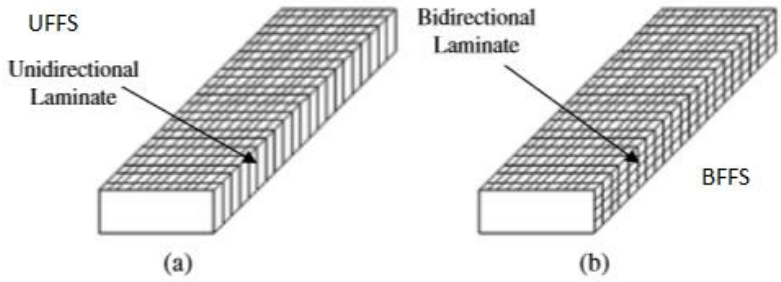

Figure 1.16: Layout of fiber composites (Mousa and Uddin, 2009)

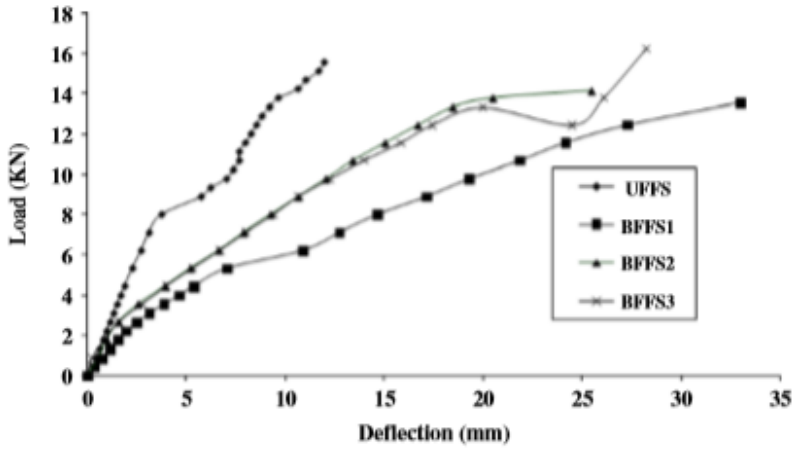

Figure 1.17: Load-displacement comparison of panel types (Mousa and Uddin, 2009)

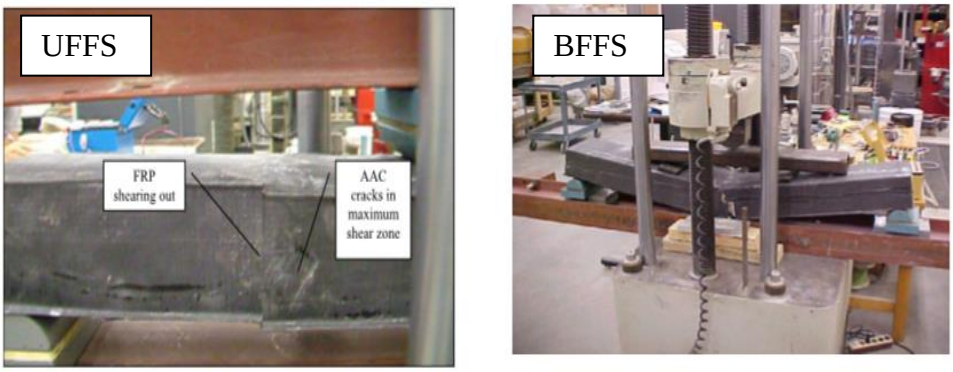

Figure 1.18: Failure mode of specimens (Mousa and Uddin, 2009)

Table 1.9: Comparison of analytical modeling and experimental results for UFFS panel type (Mousa and Uddin, 2009)

Panel no.	Loading condition	Experimental shear force (kN)	Nominal shear strength (kN)	Difference %
UFFS	Simply supported	7.77	8.41	7.6

Table 1.10: Comparison of analytical modeling and experimental results for BFFS panel types (Mousa and Uddin, 2009)

Data	BFFS1	BFFS2	BFFS3
b (mm)	175	175	175
t_{FRP} (mm)	0.25	0.25	0.25
ε_{rFRP}	0.012	0.012	0.012
E (MPa)	41380	41380	41380
d (mm)	100.25	100.25	100.25
M_n (kN m)	2.18	2.18	2.18
P (N)	13600	14150	16240
L (mm)	1200	1200	1200
$M_{EXP.}$ (kN m)	2.72	2.83	3.25
Difference % of ($M_{EXP.}$ & M_n)	24.9	29.9	49.1

1.5 Objectives and Scope

The literature review shows that there is very limited number of studies on FRP-AAC composites designed to act as load bearing members. Most of the work concentrated on the strengthening of reinforced AAC members by using CFRPs. However, it could be argued that FRP reinforced AAC composites can also be designed economically as a steel free member with no corrosion vulnerability. Due to the workmanship involved with steel reinforcement placement in a factory, FRPs, when used in AAC structural members, can also reduce the costs associated with workmanship, energy and material.

The objectives of this work can be outlined as follows:

1- To experimentally prove that FRP reinforced AAC members can act as load bearing members,
2- To simulate the experimentally observed response by using classical section analysis tools,
3- To propose FRP amounts for typical uniform loads on AAC beams.

1.6 Organization of the Thesis

This thesis study is composed of four chapters. In Chapter 1, brief information regarding manufacturing process, structural performance, application areas and material behavior of FRP and AAC is presented. Experimental study is the main concept of Chapter 2. In this chapter; test setup, material properties used in the experiment are explained and load-displacement curves are plotted for all specimen types. Failure modes and graphical results are discussed in detail. The assumptions established and algorithm behind obtaining the moment-curvature and load-displacement analyses in analytical modeling for reference/composite AAC specimens are issued in Chapter 3. Then, results obtained via computational modeling are compared with experimental analysis and comments are made on the usable strain levels of FRP. In addition, depending on demanded uniform loads, design charts were prepared to determine the economically feasible FRP configuration of AAC beams having different span lengths and cross section dimensions. In Chapter 4, conclusion and summary are given.

CHAPTER 2

EXPERIMENTAL STUDY

2.1 General

Experimental work was conducted to understand the load-displacement relation of reinforced and composite AAC blocks with the collaboration of Middle East Technical University and AKG Gazbeton. All the test specimens were prepared and tested at the factory of AKG Gazbeton in Kırıkkale. In the context of the experimental program, test specimens were categorized into two classes named as "reference" and "composite". Also, composite ones were divided into two subcategories called "full FRP" and "half FRP" in terms of FRP application width. As can be understood from their names, while "full FRP" indicates that FRP was applied throughout full specimen width, "half FRP" denotes fibers were placed for only the half portion of specimen width. In addition, fibers were implemented on the top and bottom faces of the specimens for both classes. Among the specimens tested with the fibers, two types of FRPs including Carbon Fiber Reinforced Polymer (CFRP) and Glass Fiber Reinforced Polymer (GFRP) were used. A total of 13 beam specimens were tested throughout the experimental program.

Specimen denoted as "reference" implies that the specimens were constructed with steel reinforcement without using any FRPs. A typical beam design reinforcement was used for these tests where 4 mm diameter rebars were placed as shown in Figure 2.1. For all composite AAC blocks, tests were conducted without using any steel reinforcement. Cross section properties, reinforcement configurations and fiber layouts are shown in Figure 2.1 for all the test specimens. In this chapter; material properties, test procedure, test setup, test specimens and experimental results are explained.

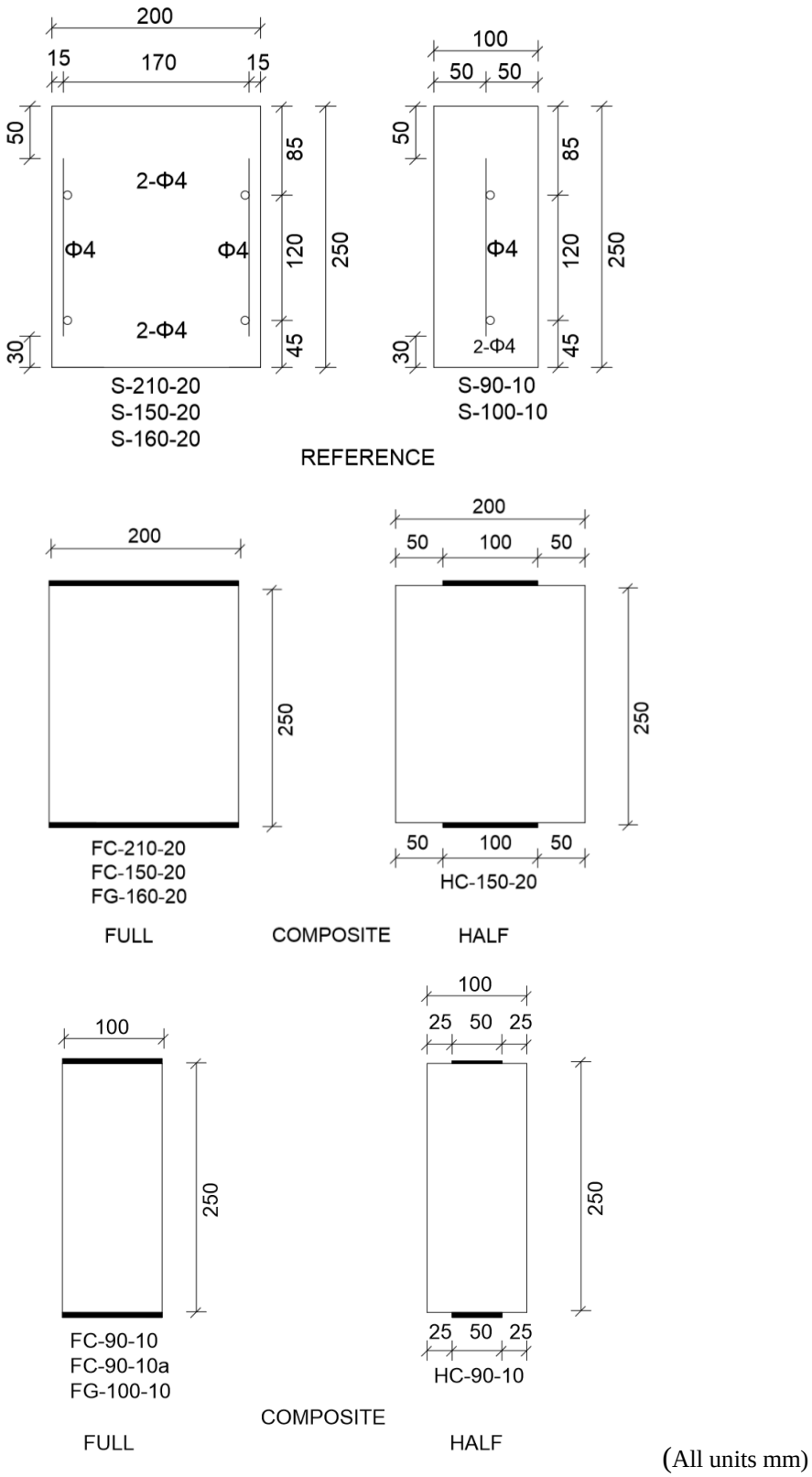

Figure 2.1: Specimen cross section properties

2.2 Material Properties

Within the scope of this study, grades of AAC blocks were G2/04 and G3 for composite and reference specimens, respectively. For all reference test specimens, S500 rebar grade was used as the steel reinforcement. Unidirectional single layer CFRP and GFRP laminates were used for specimens tested with FRPs. Mechanical properties of all the materials are summarized in Tables 2.1 through 2.3. The material data was obtained from the quality control tests of AKG.

Table 2.1: Mechanical properties of AAC

Specimen type	AAC grade	28 day compressive strength (MPa)	Modulus of Elasticity (MPa)
Reference	G3	3.5	1750
Composite	G2/04	2.5	1000

Table 2.2: Mechanical properties of steel

Specimen type	Steel grade	Yield strength (MPa)	Ultimate strength (MPa)	Modulus of Elasticity (MPa)	Ultimate strain
Reference	S500	500	550-730	200000	0.120

Table 2.3: Mechanical properties of FRPs

Specimen type	Fiber type	Fiber thickness (mm)	Tensile strength (MPa)	Modulus of Elasticity (MPa)	Ultimate strain
Composite	Carbon	0.165	3900	230000	0.015
	Glass	0.132	2300	76000	0.040

2.3 FRP Bonding

Firstly, AAC surface was cleaned from dirty substances and surface was filled by using putty. Epoxy was applied on the smooth surface and FRP sheets. Then, AAC blocks were placed adjacent to each other by using adhesive to achieve the required span lengths. Afterwards, fiber polymers (glass, carbon) were bonded at the top and bottom faces along beam length. Finally, finishing epoxy coat was applied by brush on the composite layer and specimens were left to curing. The procedure of making FRP re-

inforced AAC composite beams is shown in Figure 2.2. The most prominent advantages of this application are to prepare the specimens without any reinforcement inside, construct economical beams, ease to carry and handle AAC blocks.

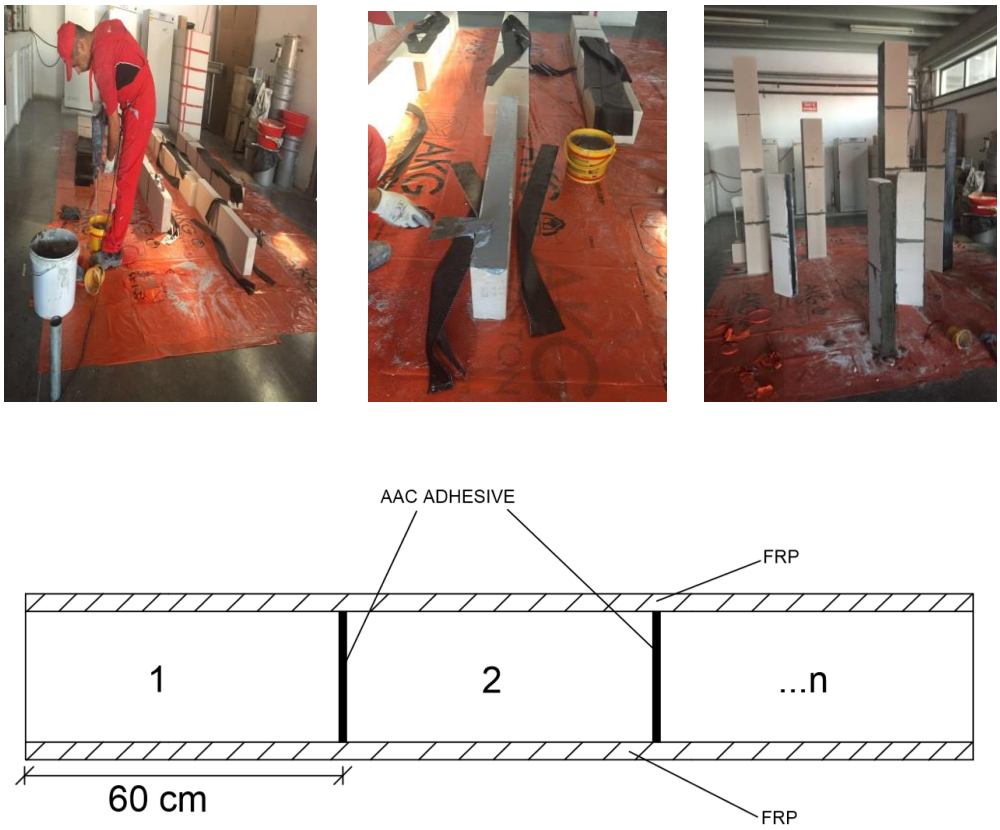

Figure 2.2: Composite AAC beam production

2.4 Experimental Setup

The experiments were conducted at the factory of AKG Gazbeton in Kırıkkale. In the tests, four-point symmetrical loading setup for the simply supported beams was used (Figure 2.3). Displacement was measured by means of a displacement transducer at the mid-span. Load was measured through the load cell attached to the loading machine. The applied load versus mid-span deflection was the key result of the tests. The experimental setup is shown in Figure 2.4. In this figure, "L" denotes the beam length and the clear span length is defined by "L_n". The distance from load application point to the support is represented by "a". Also, "v" indicates the distance measured from support to the beam outer face.

Figure 2.3: Loading setup and data acquisition system

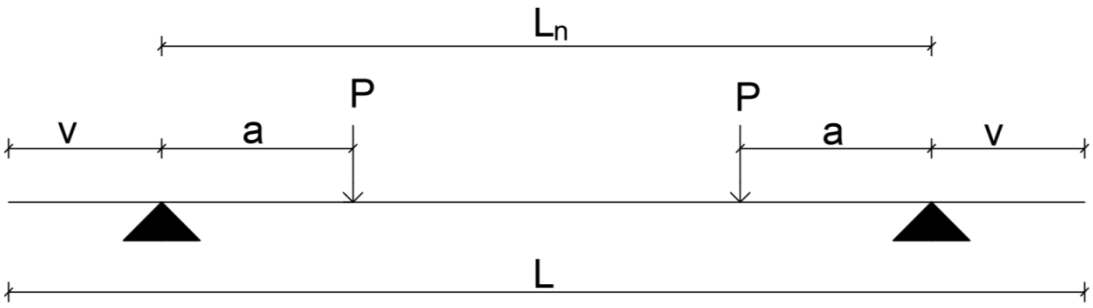

Figure 2.4: Idealized experimental loading scheme

2.5 Test Specimens

The specimens were named by using some abbreviations as presented in Table 2.4. First term in these abbreviations indicates the reinforcement type of the specimen (i.e; steel reinforcement, fiber reinforcement). For example, when the specimen was reinforced with steel, specimen was labeled by "S". On the other hand, if the specimen was reinforced with fiber composites; the first letter defines the FRP application type (such as "F", "H"), second letter represents the fiber type (i.e; "C", "G"). As a result, first part of naming was constructed by combining the first letters of FRP application type and fiber type, respectively. In addition to this, second term defined by numbers represents the specimen clear length, third term denotes the specimen width. In order to give an example, S-150-20 indicates that specimen was reinforced with steel (S), had a clear span length of 150 cm and the width of 20 cm. Similar to the this example, FC-90-10 implies that specimen was reinforced with carbon (C) fiber applied throughout full (F) specimen width of 10 cm and had a clear span length of 90 cm.

A total of 13 specimens were tested during the experimental program. Specimen sizes, specimen types, fiber types, fiber widths, fiber locations and the support distances are provided in Table 2.4. These specimens were evaluated in three different categories named as Group A to C. Specimen labels in these groups are explained in Tables 2.5 through 2.7. The criteria behind these classifications are specified based on the test parameters that include reinforcement type (i.e; reference, composite) and fiber type (such as carbon, glass).

Among these categories, Group A includes all the reference specimens constructed by using conventional steel reinforcement. While the specimens tested with CFRP were included in Group B, GFRP bonded specimens were named as Group C.

Table 2.4: Properties of the specimens used in the experiment

Specimen Label	Category	Size (cm) (width × height × length)	a (cm)	v (cm)	a/h	Fiber width		Explanation
						Bottom	Top	
S-210-20	Group-A	20 × 25 × 210	52.5	15	2.1	—	—	Reference
S-150-20	Group-A	20 × 25 × 150	37.5	15	1.5	—	—	Reference
S-160-20	Group-A	20 × 25 × 160	40	10	1.6	—	—	Reference
S-90-10	Group-A	10 × 25 × 90	22.5	15	0.9	—	—	Reference
S-100-10	Group-A	10 × 25 × 100	25	10	1	—	—	Reference
FC-210-20	Group-B	20 × 25 × 210	52.5	15	2.1	20	20	Full CFRP
FC-150-20	Group-B	20 × 25 × 150	37.5	15	1.5	20	20	Full CFRP
FC-90-10	Group-B	10 × 25 × 90	22.5	15	0.9	10	10	Full CFRP
FC-90-10a	Group-B	10 × 25 × 90	22.5	15	0.9	10	10	Full CFRP- AAC adhesive
HC-150-20	Group-B	20 × 25 × 150	37.5	15	1.5	10	10	Half CFRP
HC-90-10	Group-B	10 × 25 × 90	22.5	15	0.9	5	5	Half CFRP
FG-160-20	Group-C	20 × 25 × 160	40	10	1.6	20	20	Full GFRP
FG-100-10	Group-C	10 × 25 × 100	25	10	1	10	10	Full GFRP

Table 2.5: Group A specimens

L(cm)	v(cm)	Specimen Label
120	10	S-100-10
	15	S-90-10
180	10	S-160-20
	15	S-150-20
240	15	S-210-20

Table 2.6: Group B specimens

L(cm)	v(cm)	Fiber width / specimen width		Specimen Label
		Bottom	Top	
120	15	1	1	FC-90-10
		1	1	FC-90-10a
		0.5	0.5	HC-90-10
180	15	1	1	FC-150-20
		0.5	0.5	HC-150-20
240	15	1	1	FC-210-20

Table 2.7: Group C specimens

L(cm)	v(cm)	Fiber width / specimen width		Specimen Label
		Bottom	Top	
120	10	1	1	FG-100-10
180	10	1	1	FG-160-20

2.6 Experimental Results

In this part, total load-displacement curves obtained from the experiments are presented and comparisons are made for each group in detail. Figure 2.5 represents a typical load-displacement graph. Important points; i.e; secant stiffness (K_s), ultimate load capacity (P_u), ultimate displacement (Δ_u), yield displacement (Δ_y) and energy absorption capacity (E) are shown in this figure. Test results for each group are summarized in tabular form at the end of each group. Test parameters reported in these summary tables are explained in Table 2.8, as well.

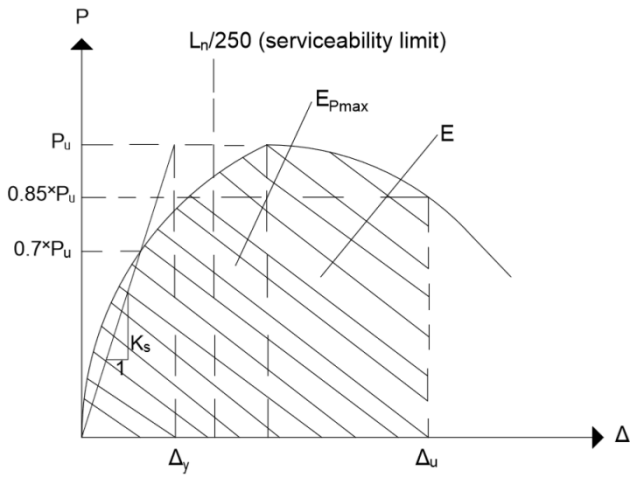

Figure 2.5: Typical load-displacement curve

Table 2.8: Definition of test parameters

Test parameter	Explanation
Δ_{cr}	Displacement value at which cracking initiates
ΔL	Displacement serviceability limit ($L_n/250$)
μ	Ductility ratio (Δ_u/Δ_y)
q	Uniform distributed load that causes the same moment due to maximum point load given in the test data
E_{Pmax}	Energy absorption capacity enclosed by the area between the origin and P_u-Δ under load-displacement curve

2.6.1 Group-A

The results of the steel reinforced specimens given in Table 2.5 are presented in this section. The effects of cross-section size, span length and reinforcement on ductility, load carrying capacity and energy absorption capacity characteristics are discussed. Figures 2.6 and 2.7 present the pictures of the test setup and the dimensions of the specimens, respectively. Load-displacement curves are presented in Figure 2.8. The pictures of failed specimens are shown in Figure 2.9. Summary of test results is provided in Table 2.9.

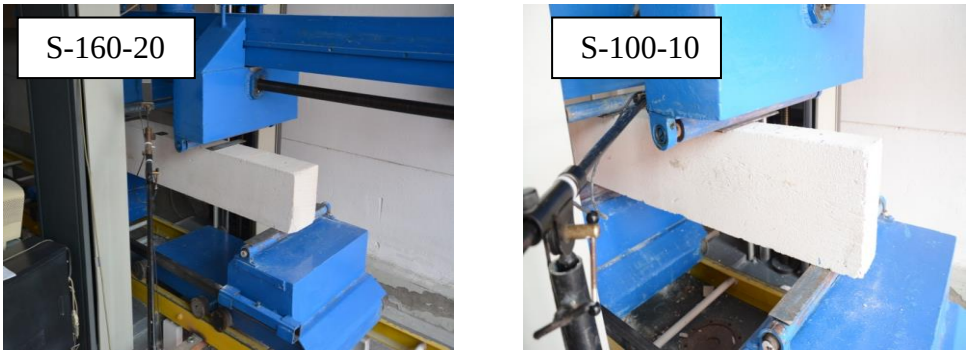

Figure 2.6: Test setup of Group-A specimens

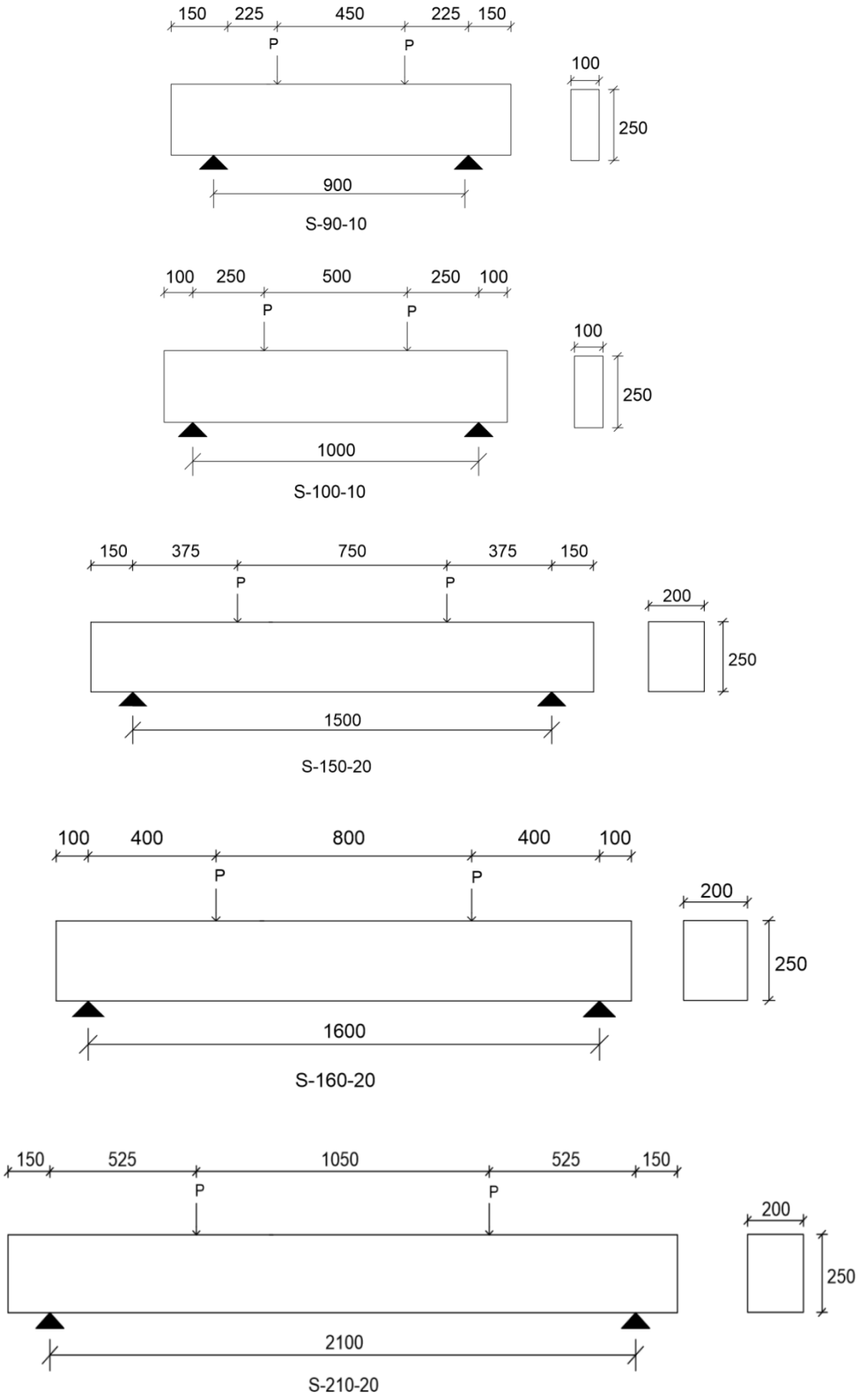

Figure 2.7: Group-A specimen dimensions (All units mm)

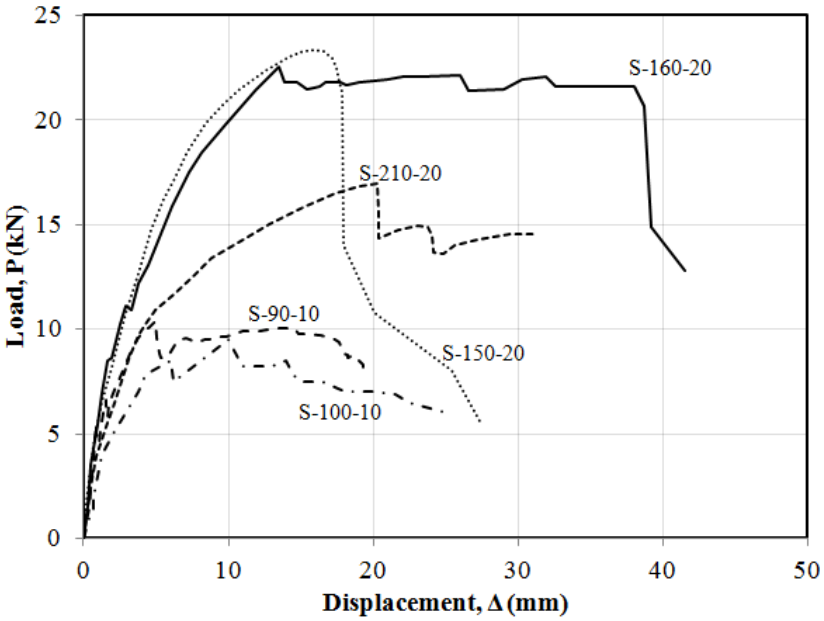

Figure 2.8: Load-displacement curves for Group-A specimens

Stiffness

The stiffness of the specimens were estimated by drawing a secant line to the load-displacement plots. The stiffness values presented in Table 2.9 show that stiffness of the specimens increased with increasing section depth and decreased with increasing span lengths. The ratio of secant stiffness for S-150-20 to S-160-20 was about 1.1, which is in proportion to the EI_{eff}/L^3 ratio of the two members. A similar comparison can be made upon observing the stiffness ratio of S-150-20 and S-210-20. However, the stiffness of S-210-20 was considerably smaller than its expected secant stiffness. The stiffness ratio between S-90-10 and S-100-10 was not perfectly proportional with EI_{eff}/L^3, as well. The reason of this contradictory result can be attributed to the possible variation in the modulus of elasticity of AAC from specimen to specimen and presence of precracks formed at the autoclave chamber. Apart from those, Table 2.9 indicates that displacements at which cracking initiates were below the displacement limit defined under serviceability condition.

Strength

First, the specimens having the width of 20 cm were investigated. These specimens were identical except for their shear span lengths. Following Figure 2.8, it can be observed that the load carrying capacities were almost equal for S-150-20 and S-160-20.

On the other hand, S-210-20 had about 25% smaller load capacity compared to the others. Secondly, the comparison was made for the specimens having the width of 10 cm. Similar to the first case, the only difference between S-90-10 and S-100-10 was their shear span lengths. Figure 2.8 represents that S-90-10 and S-100-10 nearly reached to the same load capacity. From a structural point of view, it is expected that transverse loads are inversely proportional with the shear span length provided that all other parameters are the same. As a result, it is seen that the relation between load carrying capacities of the specimens were compatible with this approach. However, it should be remembered that reinforcement configurations were different for the specimens having the width of 10 cm and 20 cm (see Figure 2.1). Therefore, detailed estimation of load capacities and its comparisons with test results will be conducted in Chapter 3. In addition to this, all the reference test specimens showed AAC crushing after following steel yielding.

Ductility

According to Table 2.9, it is seen that ductility levels were significantly different between S-150-20 and S-160-20. Although the key difference between the specimens was the minor span length difference, there was a major change in their ductility values. The brittle nature of S-150-20 can be due to the bond failure of the reinforcement following flexural cracking, whereas S-160-20 experienced a ductile flexural failure mode where AAC crushing observed after significant steel yielding. On the other hand, ductility of the S-90-10 and S-100-10 were similar as expected.

Energy absorption capacity

When S-210-20, S-160-20 and S-150-20 were compared for energy absorption capacity, it is seen that S-160-20 had about 2.5, 3 times higher values relative to S-150-20 and S-210-20, respectively. Table 2.9 clearly exhibits that the relation between energy absorption capacities of the specimens were directly related to E/E_{Pmax} ratio. As seen from this table, difference in E/E_{Pmax} ratios of these specimens were between 20-30% when compared with the ratios of their corresponding energy absorption capacities. Therefore, it can be observed that E/E_{Pmax} is an important indicator of displacement ductility for the tested specimens.

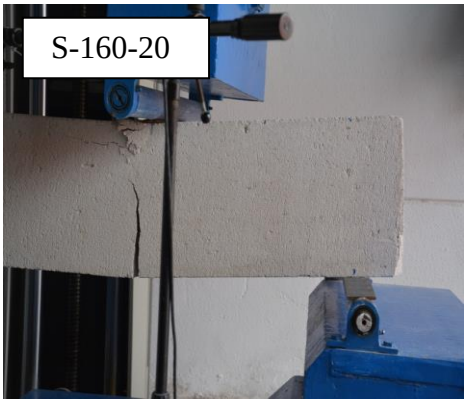

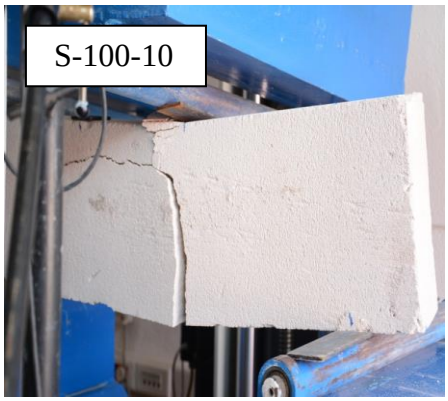

Figure 2.9: Failure modes of Group-A specimens

Table 2.9: Summary table for Group-A specimens

Specimen Label	Size (W × H) in cm	Δ_{cr} (mm)	ΔL (mm)	Δ_y (mm)	Δ_u (mm)	K_s (kN/m)	μ	E_{Pmax} (N.m)	E (N.m)	E/E_{Pmax}	q (kN/m)	Failure mode
S-210-20	20 × 25	1.63	8.4	9.40	20.74	1805.45	2.2	257.98	265.12	1.03	8.25	Steel yielding
S-160-20	20 × 25	1.35	6.4	8.63	38.90	2614.64	4.50	207.03	759.63	3.66	14.32	Steel yielding
S-150-20	20 × 25	1.74	6.0	8.01	17.87	2914.19	2.2	272.46	316.80	1.16	16.22	Steel yielding
S-100-10	10 × 25	1.60	4.0	5.17	10.94	1902.35	2.1	43.15	62.34	1.44	9.90	Steel yielding
S-90-10	10 × 25	2.10	3.6	3.14	5.20	3297.25	1.7	35.23	37.44	1.06	12.95	Steel yielding

2.6.2 Group-B

The results of composite specimens given in Table 2.6 are presented in this section. The effects of cross-section size, span length and reinforcement on ductility, load carrying capacity and energy absorption capacity characteristics are discussed. The specimens in Group-B are analyzed in two subcategories in terms of their cross section sizes.

2.6.2.1 Group-B1

In this group, all the specimens had the dimensions of 10 cm × 25 cm. Figures 2.10 and 2.11 present the pictures of the test setup and the dimensions of the specimens, respectively. Load-displacement curves are presented in Figure 2.12. The pictures of failed specimens are shown in Figure 2.13. Summary of test results is provided in Table 2.10.

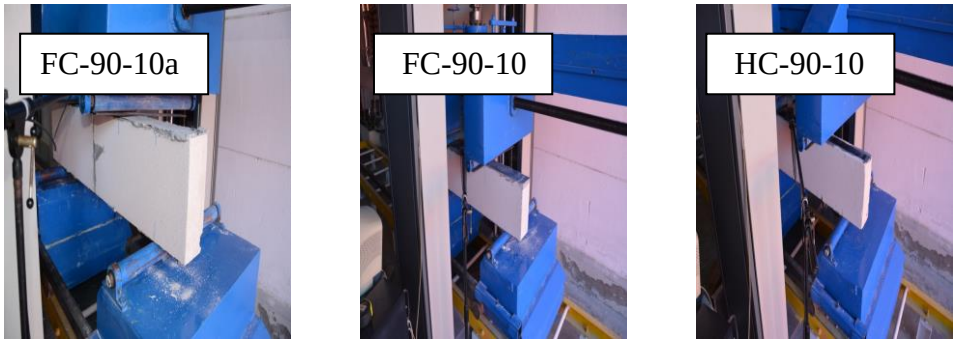

Figure 2.10: Test setup of Group-B1 specimens

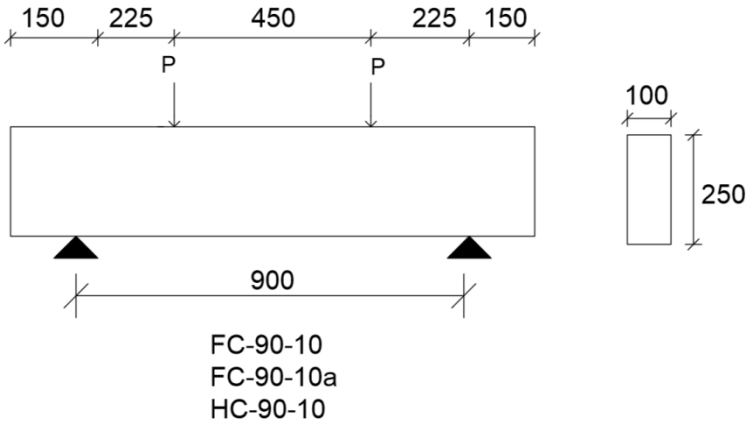

(All units mm)

Figure 2.11: Group-B1 specimen dimensions

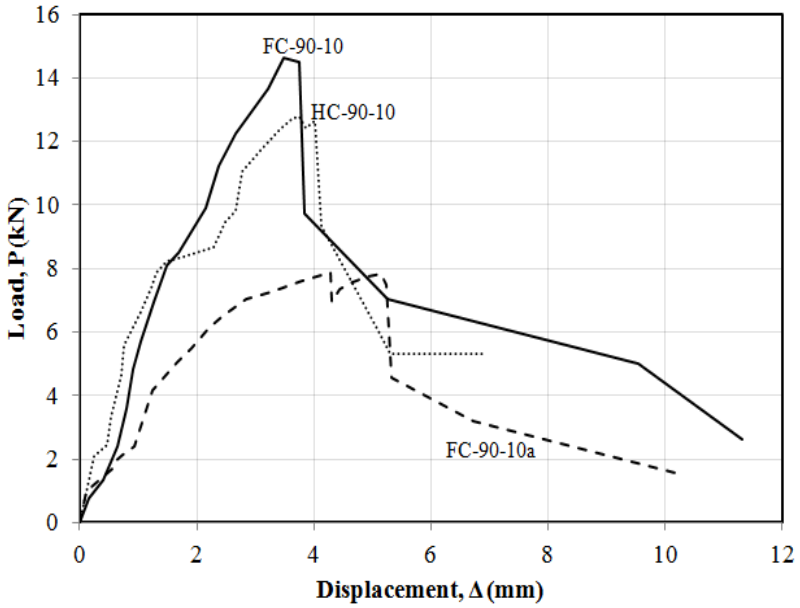

Figure 2.12: Load-displacement curves for Group-B1 specimens

Stiffness

Table 2.10 indicates that FC-90-10 had higher secant stiffness compared to HC-90-10 due to the use of double FRP width as expected. Also, since the epoxy-based adhesive used for FC-90-10 was stiffer relative to the AAC adhesive used in FC-90-10a, smaller secant stiffness was obtained. Furthermore, it was understood that cracking displacement values given in Table 2.10 were smaller than the allowable displacement limit for all the specimens.

Strength

According to Figure 2.12, maximum and minimum load capacities were obtained from FC-90-10 and FC-90-10a, respectively. The figure represents that load capacity was about 15% higher for FC-90-10 compared to HC-90-10. Since the fiber amount in FC-90-10 was double that of the amount used in HC-90-10, it was theoretically expected that load capacity of FC-90-10 would be double that of the capacity obtained from HC-90-10. However, the back calculated FRP strains in Chapter 3 show that HC-90-10 exhibited about 80% greater debonding strain compared to FC-90-10. Such a situation can enable to increase the load capacity of HC-90-10. Therefore, the observed capacities seemed to be reasonable based on the calculations presented in Chapter 3. When FC-90-10 and FC-90-10a were compared, Figure 2.12 indicates that FC-90-10 had approximately 85% greater load capacity. Actually, these two specimens were identical except the adhesive type. AAC adhesive is a more ductile but less stronger material than the epoxy-based adhesive. Hence, observed response shows that use of epoxy was better for strength enhancement. Detailed estimation of load capacities and its comparisons with test results will be conducted in Chapter 3. Apart from those, AAC crushing was observed during the testing of FC-90-10a. On the other hand; while FC-90-10 exhibited shear cracking initiating from the fiber, FRP delamination was observed in HC-90-10.

Ductility

Figure 2.12 shows that there was a sudden drop in load carrying capacity after reaching the peak loads for all the specimens. Therefore, there was a limited ductility for these specimens compared to the ones with steel reinforcement. This result is similar to those

observed in the testing of FRP bonded reinforced concrete beams. As a result of this fact, Table 2.10 shows that ductility levels were almost the same for FC-90-10 and HC-90-10 although the fiber amounts used were different. The reason of slightly higher ductility of FC-90-10a relative to the others can be attributed to the ductile characteristics of AAC adhesive compared to a more brittle epoxy.

Energy absorption capacity

Following Table 2.10, FC-90-10 and HC-90-10 had almost the same energy absorption capacities similar to their ductility levels as expected. However, it was anticipated that FC-90-10a had higher energy absorption capacity relative to the others due to adhesive type. Although a tension controlled failure mechanism occurred for FC-90-10a, Figure 2.12 implies that a brittle load-displacement curve pattern was observed due to the brittle nature of FRPs.

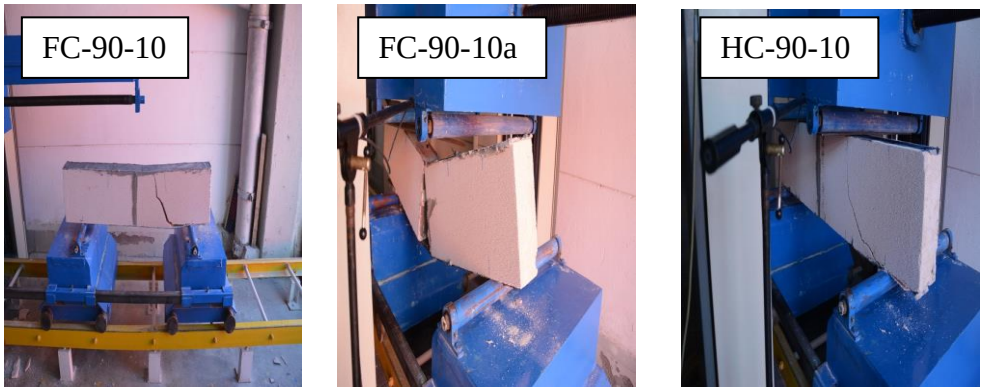

Figure 2.13: Failure modes of Group-B1 specimens

Table 2.10: Summary table for Group-B1 specimens

Specimen Label	Size (W × H) in cm	Δ_{cr} (mm)	ΔL (mm)	Δ_y (mm)	Δ_u (mm)	K_s (kN/m)	μ	E_{Pmax} (N.m)	E (N.m)	E/E_{Pmax}	q (kN/m)	Failure mode
FC-90-10	10 × 25	1.38	3.6	3.14	3.80	4651.05	1.21	28.26	32.64	1.15	18.27	Shear
FC-90-10a	10 × 25	1.12	3.6	2.71	5.26	2895.97	1.94	22.29	29.73	1.33	9.83	AAC crushing
HC-90-10	10 × 25	0.43	3.6	3.36	4.10	3783.81	1.22	29.82	34.24	1.15	15.88	FRP delamination

2.6.2.2 Group-B2

In this group, all the specimens had the dimensions of 20 cm × 25 cm. Figures 2.14 and 2.15 present the pictures of the test setup and the dimensions of the specimens, respectively. Load-displacement curves are presented in Figure 2.16. The pictures of failed specimens are shown in Figure 2.17. Summary of test results is provided in Table 2.11.

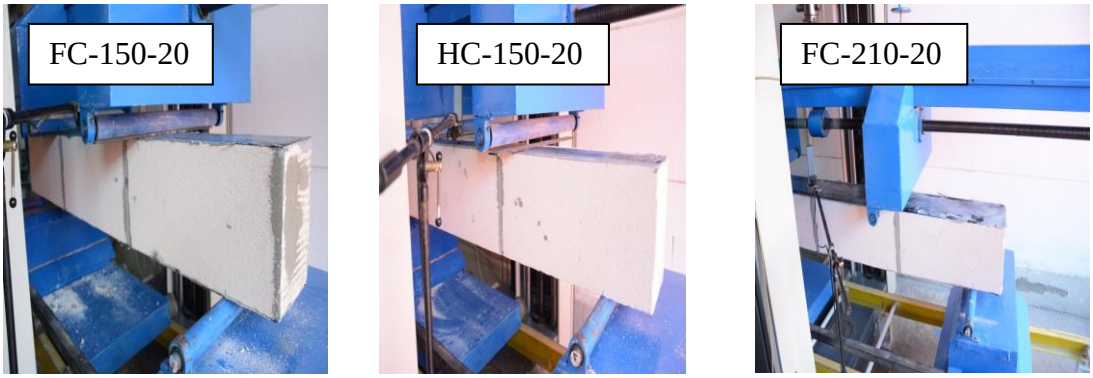

Figure 2.14: Test setup of Group-B2 specimens

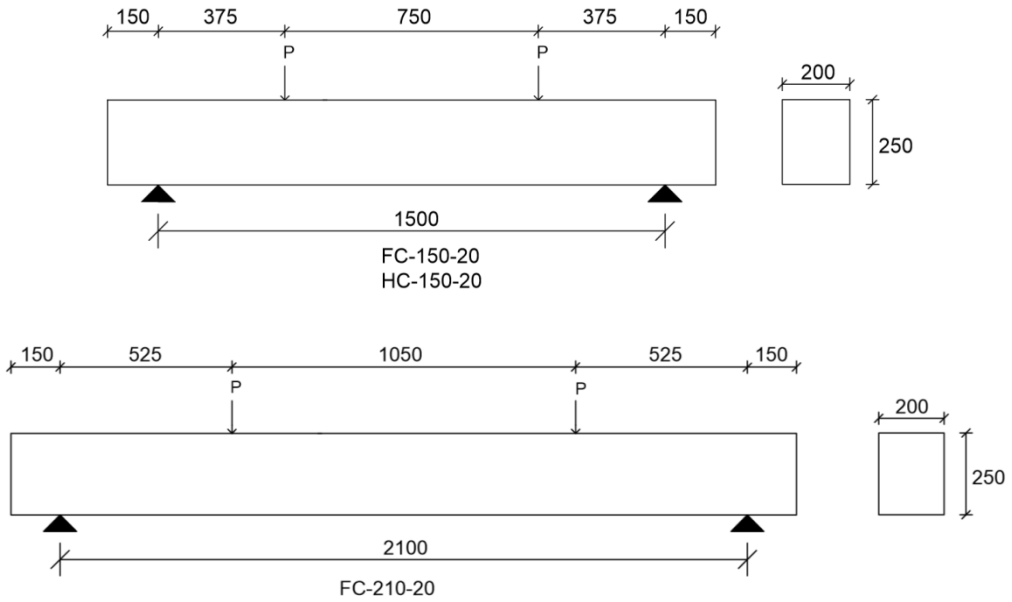

Figure 2.15: Group-B2 specimen dimensions

(All units mm)

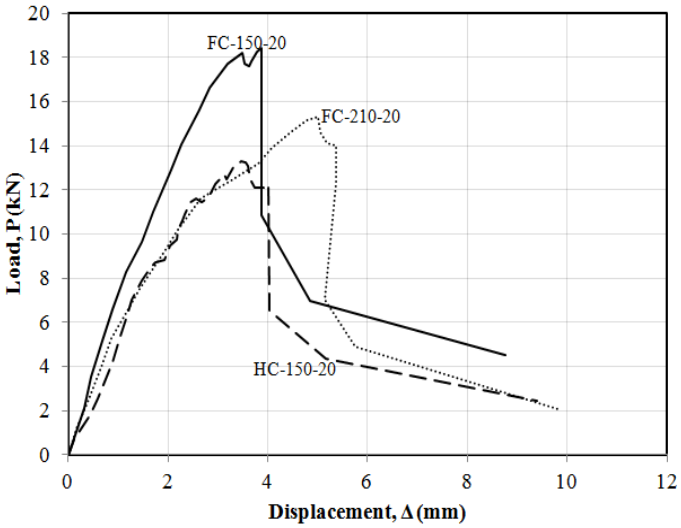

Figure 2.16: Load-displacement curves for Group-B2 specimens

Stiffness

According to Table 2.11, secant stiffness was higher for FC-150-20 compared to HC-150-20 as a result of double fiber amount used. Besides, it was observed that cracking displacement values given in Table 2.11 met the displacement criteria based on serviceability specified for all the specimens.

Strength

When Figure 2.16 was examined, maximum and minimum load capacities were obtained from FC-150-20 and HC-150-20, respectively. The figure shows that load capacity was about 40% higher for FC-150-20 compared to HC-150-20. It should be known that the only difference between these two specimens was the fiber amount applied. Since the fiber amount in FC-150-20 was double that of the amount used in HC-150-20, it was theoretically expected that load capacity of FC-150-20 would be double that of the capacity obtained from HC-150-20. On the other hand, the increase in the load capacity obtained from the experimental results were significantly below the expected one. However, the back calculated FRP strains in Chapter 3 show that debonding strain was approximately 30% higher for HC-150-20 compared to FC-150-20. Higher debonding strain can improve the load capacity of HC-90-10. For this reason, experimental load carrying capacities that are close to each other relative to expected one can be admissible as per the calculations illustrated in Chapter 3. The other comparison was made between FC-150-20 and FC-210-20. Figure 2.16 indicates that

FC-150-20 had approximately 20% greater load capacity compared to FC-210-20. Actually, these two specimens were identical except for their span lengths. Therefore, it was expected that the difference would be 40% due to their span length ratio. Detailed estimation of load capacities and its comparisons with test results will be conducted in Chapter 3. Besides, FC-150-20 and HC-150-20 failed in shear. FRP delamination was observed in FC-210-20.

Ductility

Load-displacement curve pattern shown in Figure 2.16 was almost identical with the previous group composite specimens. Although fiber amounts were different among the specimens, Table 2.11 indicates that ductility levels were quite close to each other due to brittle nature of fibers.

Energy absorption capacity

Due to the low ductility levels of the specimens, Table 2.11 represents that that there was no significant fluctuation between energy absorption capacities of the specimens as expected.

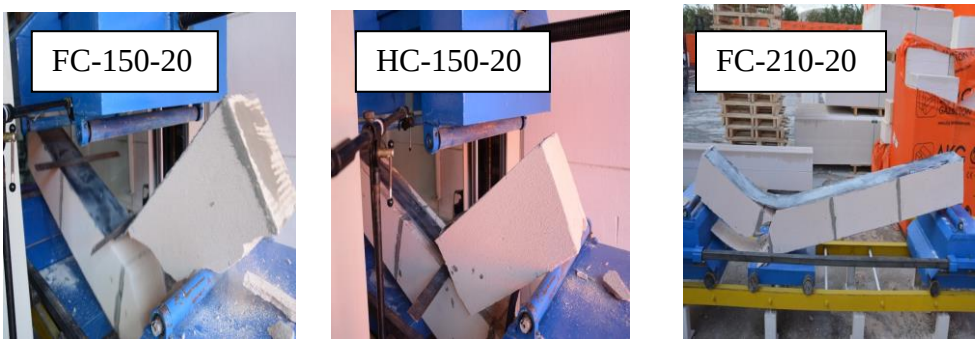

Figure 2.17: Failure modes of Group-B2 specimens

Table 2.11: Summary table for Group-B2 specimens

Specimen Label	Size (W × H) in cm	Δ_{cr} (mm)	ΔL (mm)	Δ_y (mm)	Δ_u (mm)	K_s (kN/m)	μ	E_{Pmax} (N.m)	E (N.m)	E/E_{Pmax}	q (kN/m)	Failure mode
FC-150-20	20 × 25	1.45	6.0	3.71	3.87	4914.29	1.04	42.44	44.08	1.04	12.68	Shear
HC-150-20	20 × 25	0.74	6.0	2.89	4.02	4606.27	1.39	26.95	33.72	1.25	9.23	FRP delamination
FC-210-20	20 × 25	1.26	8.4	3.37	5.37	4540.56	1.59	49.38	54.52	1.10	7.44	Shear

2.6.3 Group-C

The results of composite specimens given in Table 2.7 are presented in this section. The effects of cross-section size, span length and reinforcement on ductility, load carrying capacity and energy absorption capacity characteristics are discussed. Figures 2.18 and 2.19 present the pictures of the test setup and the dimensions of the specimens, respectively. Load-displacement curves are presented in Figure 2.20. The pictures of failed specimens are shown in Figure 2.21. Summary of test results is provided in Table 2.12.

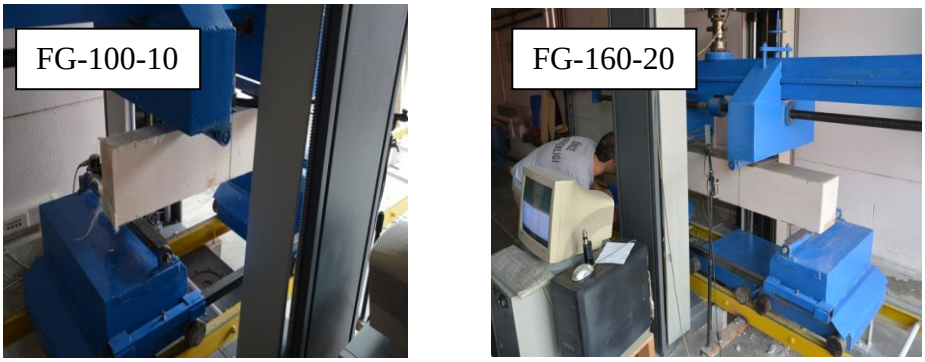

Figure 2.18: Experimental setup of Group-C specimens

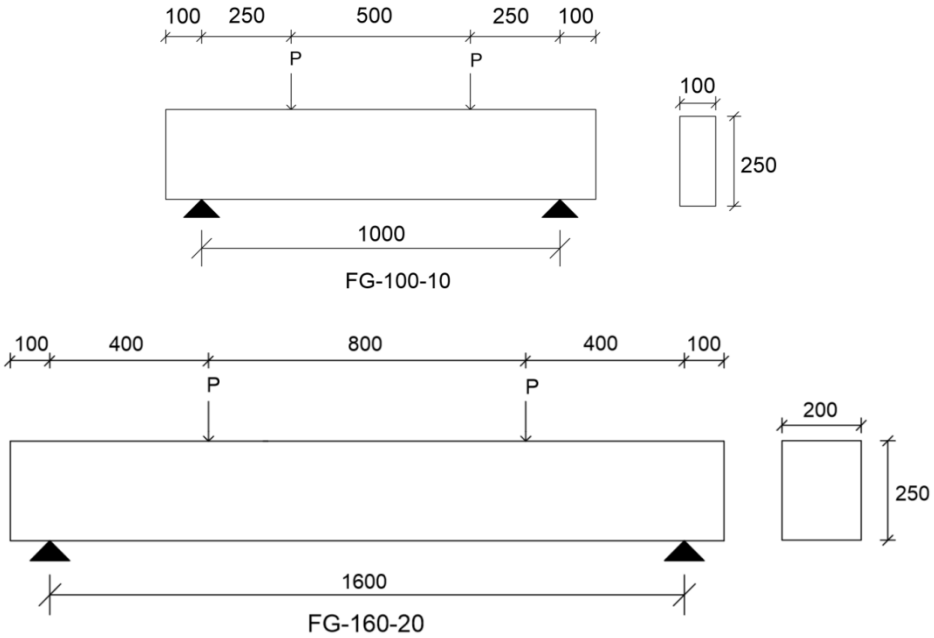

Figure 2.19: Group-C specimen dimensions

(All units mm)

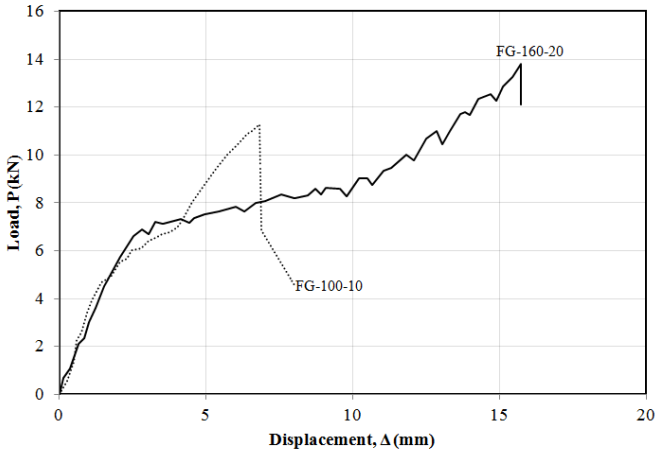

Figure 2.20: Load-displacement curves for Group-C specimens

Stiffness

Table 2.12 shows that secant stiffness values were almost equal for FG-160-20 and FG-100-10. However, it was theoretically expected that FG-160-20 would have greater secant stiffness relative to FG-100-10 due to its fiber amount. Such a result can be caused by the differentiation in material properties from specimen to specimen. It was observed that cracking displacement values of both specimens given in Table 2.12 satisfied the displacement condition.

Strength

Following Figure 2.20, it can be observed that FG-160-20 had approximately 20% greater load carrying capacity compared to FG-100-10. When the properties were taken into consideration for these specimens, it is seen that they were identical except for the section width and span length. If these test specimens had equal span length, it was expected that FG-160-20 has the capacity that double of the one obtained from FG-100-10 due to the increase in the fiber amount. On the other hand, it should be known that load capacity is reduced as the shear span length increases. When these two basic structural explanations are combined, it was anticipated that load capacity theoretically would be 25% higher for FG-160-20 relative to FG-100-10. When this ratio was compared with the one obtained from the test, it is understood that the result was reasonable. Detailed estimation of load capacities and its comparisons with test results will be conducted in Chapter 3. Also, it should be known that both specimens failed in shear.

Ductility

Table 2.12 indicates that FG-160-20 had higher ductility level compared to FG-100-10. As seen from Figure 2.20, while sharp increase/decrease was observed in FG-100-10, load-displacement pattern progressively advanced for FG-160-20. This situation can enable to allow more displacement for FG-160-20. As a result of unusual load-displacement pattern of FG-160-20, ductility levels were considerably differentiated from each other.

Energy absorption capacity

Debonding progressively occurred for FG-160-20 compared to sudden mechanism observed in FG-100-10. Although ductility levels were significantly different from each other, Table 2.12 shows that E/E_{Pmax} ratios were nearly the same.

Table 2.12: Summary table for Group-C specimens

Specimen Label	Size (W × H) in cm	Δ_{cr} (mm)	ΔL (mm)	Δ_y (mm)	Δ_u (mm)	K_s (kN/m)	μ	E_{Pmax} (N.m)	E (N.m)	E/E_{Pmax}	q (kN/m)	Failure mode
FG-100-10	10 × 25	1.50	4.0	4.02	6.86	1552.61	1.71	41.20	41.50	1.01	10.69	Shear
FG-160-20	20 × 25	2.10	6.4	4.32	16.5	1603.97	3.82	129.54	139.83	1.08	8.77	Shear

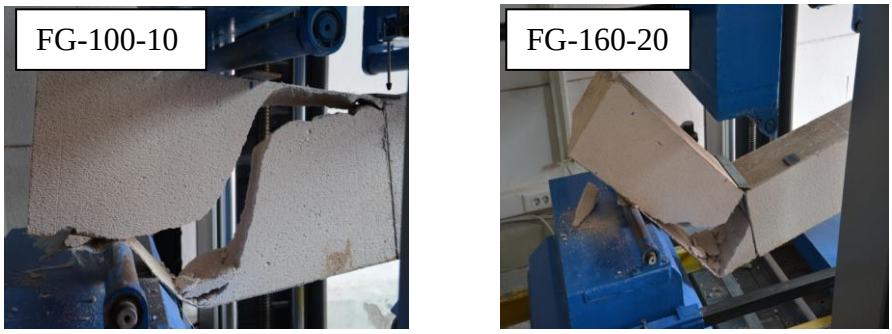

Figure 2.21: Failure modes of Group-C specimens

2.7 Concluding Remarks

The following important conclusions can be drawn from this chapter:

- FRP debonding was observed for all the composite test specimens used with epoxy-based adhesive. On the other hand, FC-90-10a showed AAC crushing since the AAC adhesive used in this specimen was more ductile compared to epoxy-based adhesive. As a result of insufficient adherence of AAC adhesive,

it is seen that FC-90-10a had approximately 50% smaller load capacity compared to FC-90-10.

- AAC crushing after steel yielding was seen for all reference specimens due to ductile characteristics of steel. As opposed to this, brittle failure was governed for all the composite AAC beams as a result of brittle nature of the fibers.
- Stiffness values of reference specimens were aligned directly proportional with EI_{eff} /L^3 ratio. On the other hand, it was seen that stiffness was significantly higher for composite specimens as the increase of fiber amount caused to increase in EI_{eff}.
- From structural point of view, load carrying capacity was inversely proportional with the shear span length for all specimen types. In addition to this fact, it was observed that load capacity increased with the increase in fiber amount for composite AAC beams.
- Test results showed that energy absorption capacity was directly linked with the strength and displacement capacity parameters for fiber reinforced and steel reinforced specimens, respectively.

CHAPTER 3

ANALYTICAL RESULTS

3.1 General

In this chapter, experimental results were compared with the analytical studies. In the context of analytical studies, a spreadsheet was developed to compute the section moment-curvature response and load-displacement curves. In this way, validation of the used analytical model was conducted. The assumptions, algorithms and theorem behind the analytical calculations are explained in detail in the following parts of this chapter. The analytical model was then used to back-calculate usable FRP strains corresponding to FRP debonding from AAC surface. Based on these results and comparisons with ACI 440 guidelines, recommendations for such strains were made for design. Finally, design charts that present the required FRP amounts for demanded uniform distributed loads were prepared for the AAC beams having different cross sections and span lengths.

3.2 Analytical Model

The assumptions, solution methods and algorithm underlying the response calculations are described as follows:

- There is a perfect bond between steel-AAC and FRP-AAC composite beams.
- Moment-curvature relation was obtained by means of an analytical section integration procedure where all possible failure modes were separately considered. Classical Euler-Bernoulli beam theory assumptions were used. In the light of moment-curvature data, load-displacement response was obtained for beams loaded under four point bending.

- A parabolic stress-strain model was used with a linear descending branch for the AAC as shown in Figure 3.1. In this figure, while f_c' represents the uniaxial compressive strength of AAC, ε_{co} and ε_{cu} indicate the strain at which f_c' becomes maximum and AAC crushes, respectively.
- It was assumed that steel behaved as an elastic-perfectly plastic material (Figure 3.2). In this figure, σ_y and ε_{sy} imply the yield strength and yielding strain of steel, respectively. Strain hardening stage of steel was not taken into consideration.
- FRP was assumed to behave as a linear elastic material up to failure (Figure 3.3). In this figure, σ_u and ε_u denote the rupture/debonding strength and debonding/rupture strain of FRP, respectively.

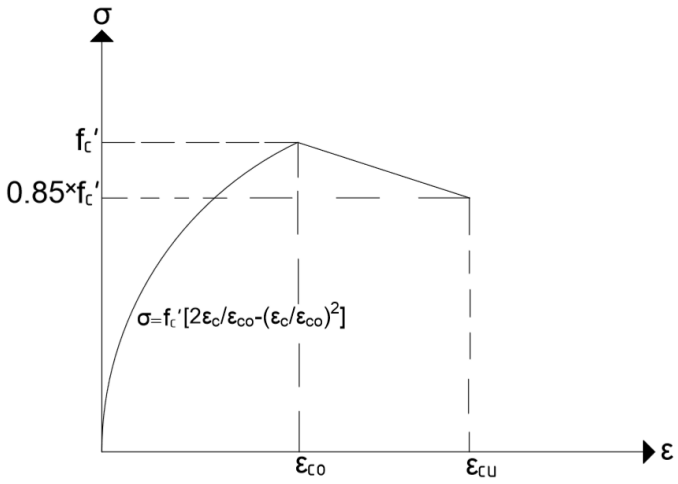

Figure 3.1: AAC stress-strain model inspired from Hognestad (1951)

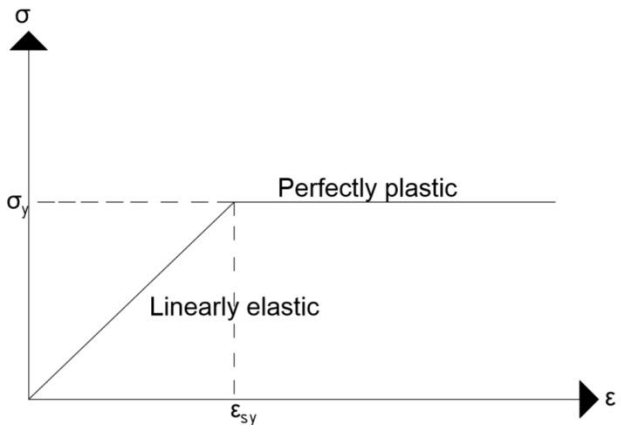

Figure 3.2: Stress-strain model for elastic-perfectly plastic steel

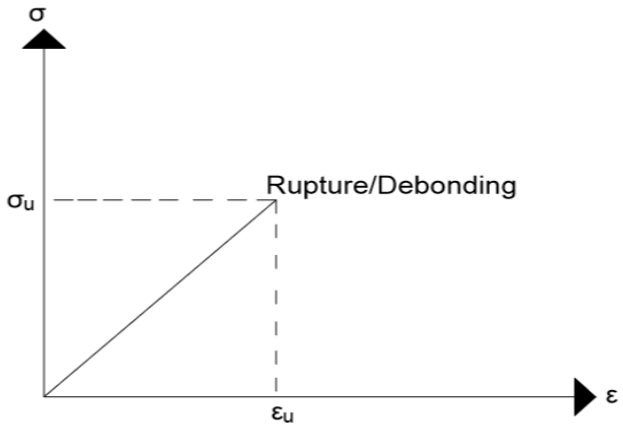

Figure 3.3: Stress-strain model for FRP

3.3 Section Analysis

Based on the assumptions explained before, stress-strain profiles and equilibrium equations were constructed for each failure situation as presented in Appendix A to B in detail. The possible failure modes presented below were solved for steel reinforced and fiber reinforced AAC beams:

a- Prior to cracking

1- It was assumed that AAC is elastic. In accordance with the transformed section method, modular ratio (n) was calculated by using the ratio of the elasticity modulus of steel or FRP to AAC (Figure 3.4).

2- Centroid of the section denoted as $\bar{y}$ was found (Figure 3.4).

3- After calculating moment of inertia of the section (I_{tr}) with respect to centroid, uncracked moment capacity was obtained by using basic principles of mechanics of materials.

4- Section curvature was determined by using M_{cr}/E_cI_{tr}.

5- (M,Ø) couple was recorded.

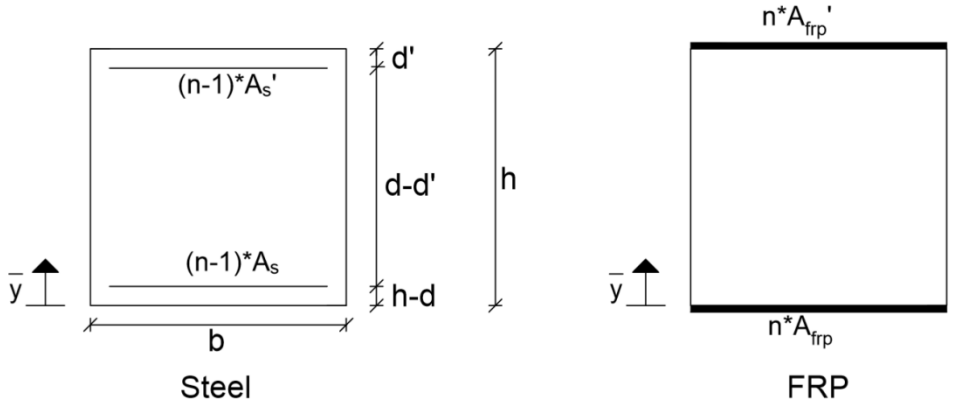

Figure 3.4: Section analysis for uncracked section

b- After cracking

1- It was assumed that AAC is elastic. Force equilibrium was established between the shaded (compression) and unshaded regions (tension) to determine the distance "c" (Figure 3.5).

2- Moment of inertia of the section (I_{cr}) was calculated with respect to the neutral axis (N.A).

3- Moment capacity was the same as the uncracked section analysis in the above step.

4- Curvature was calculated by using $M_{cr}/ E_c I_{cr}$.

5- (M,Ø) couple was recorded.

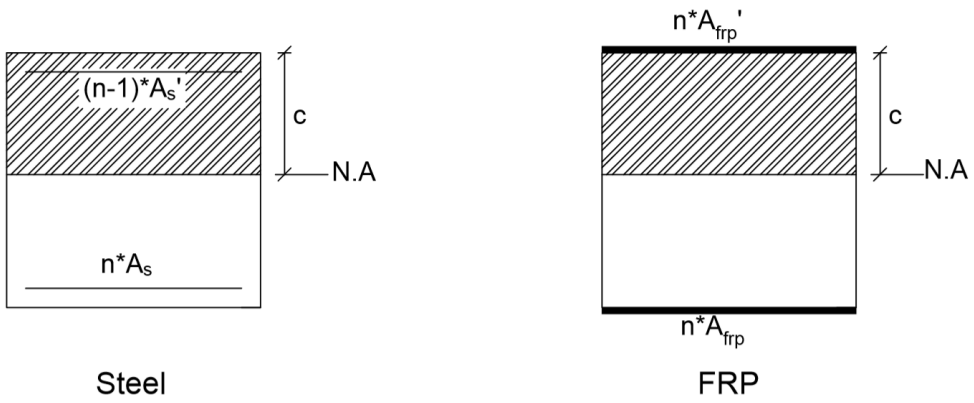

Figure 3.5: Section analysis for cracked section

c- Steel yielding

1- Depending on the steel yielding occurring either in the ascending or descending portion of Hognestad curve, force equilibrium equations were separately constructed.

2- While constructing these equations, it was paid attention whether compression steel has yielded or not. The location of the neutral axis of the section was used to compute the steel / FRP forces.

3- The "c" value was obtained from the force equilibrium equations (Figure 3.6 or Figure 3.7).

4- If force equilibrium could not be reached, it indicated that the section failed in a brittle manner.

5- Provided that appropriate "c" value existed, moment was calculated by summing the forces with respect to the neutral axis and curvature was found from the strain profile.

6- (M,Ø) couple was recorded.

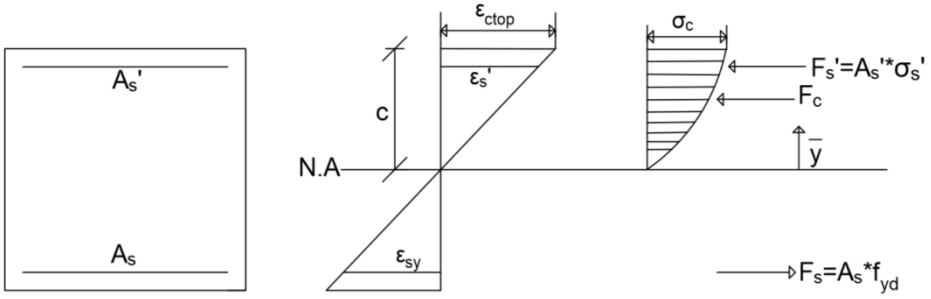

Figure 3.6: Stress-strain profile for steel yielding (ascending portion)

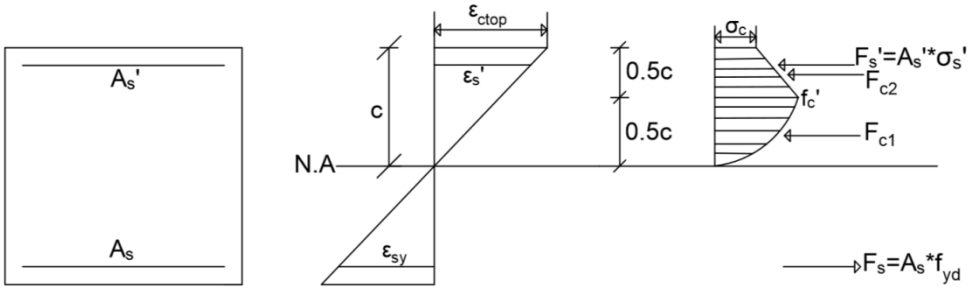

Figure 3.7: Stress-strain profile for steel yielding (descending portion)

d- AAC reaches its maximum compressive strength

Steel reinforced sections:

1- Yielding situations of tension and compression reinforcements were taken into consideration. The location of the neutral axis of the section was used to compute the steel / FRP forces.

2- All the alternatives linked with the yielding cases of both steels were separately computed.

3- Appropriate "c" value was found from one of the equilibrium equations of these alternatives (Figure 3.8).

4- Moment was computed by summing the forces with respect to the neutral axis and curvature was found from the strain profile.

5- (M,Ø) couple was recorded.

FRP reinforced sections:

1- It was assumed that FRP has not reached to its debonding strain.

2- Force equilibrium was established and "c" value was found from force equilibrium equation (Figure 3.9).

3- FRP debonding was checked.

4- If it was understood that FRP has already reached to its debonding strain, go to case (f).

5- Provided that FRP strain obtained was smaller than its debonding strain, moment was calculated by summing the forces with respect to the neutral axis and curvature was found from the strain profile.

6- (M,Ø) couple was recorded.

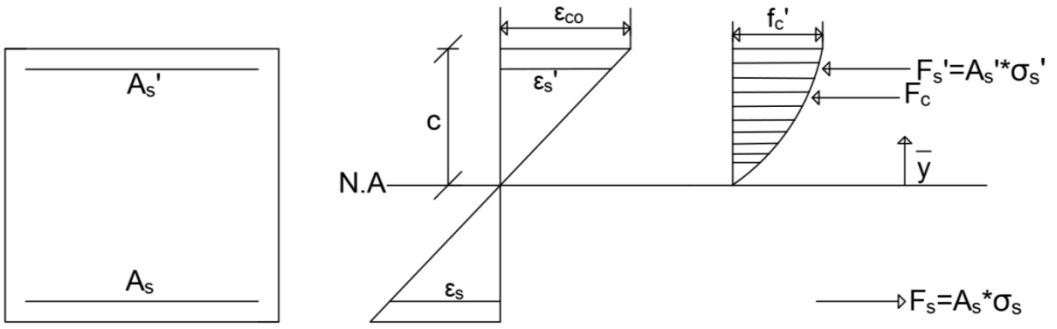

Figure 3.8: Stress-strain profile at which $\varepsilon_{ctop} = \varepsilon_{co}$ (steel reinforced sections)

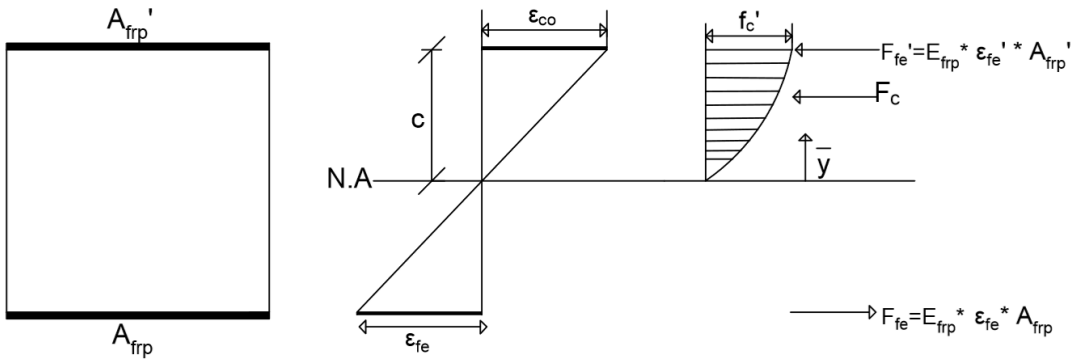

Figure 3.9: Stress-strain profile at which $\varepsilon_{ctop} = \varepsilon_{co}$ (FRP reinforced sections)

e- AAC crushing

Steel reinforced sections:

1- Yielding possibilities of tension and compression reinforcements were considered. The location of the neutral axis of the section was used to compute the steel / FRP forces.

2- All the force equilibrium equations related to the yielding conditions of both steels were separately solved.

3- Appropriate "c" value was obtained from these equations (Figure 3.10).

4- Moment was computed by summing the forces with respect to the neutral axis and curvature was found from the strain profile.

5- M-Ø couple was recorded.

FRP reinforced sections:

1- It was assumed that FRP has not reached to its debonding strain.

2- Force equilibrium was established and "c" value was found from force equilibrium equation (Figure 3.11).

3- FRP debonding was checked.

4- If it was determined that FRP has already reached to its debonding strain, go to case (f).

5- Provided that FRP strain obtained was smaller than its debonding strain, moment was calculated by summing the forces with respect to the neutral axis and curvature was found from the strain profile.

6- (M,Ø) couple was recorded.

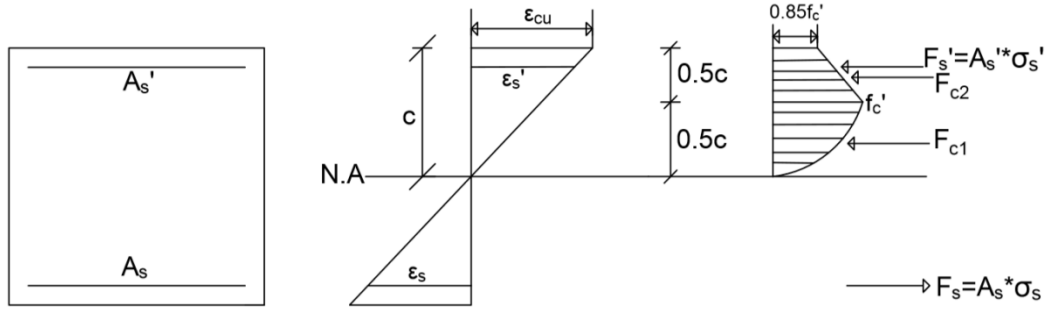

Figure 3.10: Stress-strain profile for AAC crushing (steel reinforced sections)

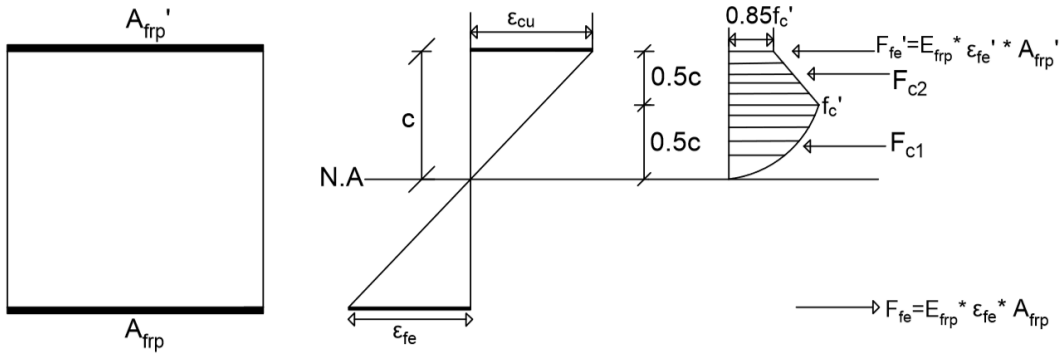

Figure 3.11: Stress-strain profile for AAC crushing (FRP reinforced sections)

f- FRP debonding

1- It was assumed that AAC has not reached to its crushing strain.

2- Depending on the FRP debonding occurring either in the ascending or descending portion of Hognestad curve, force equilibrium equations were separately constructed.

3- Appropriate "c" value was calculated from force equilibrium equations (Figure 3.12 or Figure 3.13).

4- AAC crushing was checked.

5- If it was seen that AAC has already reached to its crushing strain, go to case (e).

6- Provided that AAC strain obtained was smaller than its crushing strain, moment was calculated by summing the forces with respect to the neutral axis and curvature was found from the strain profile.

7- (M,Ø) couple was recorded.

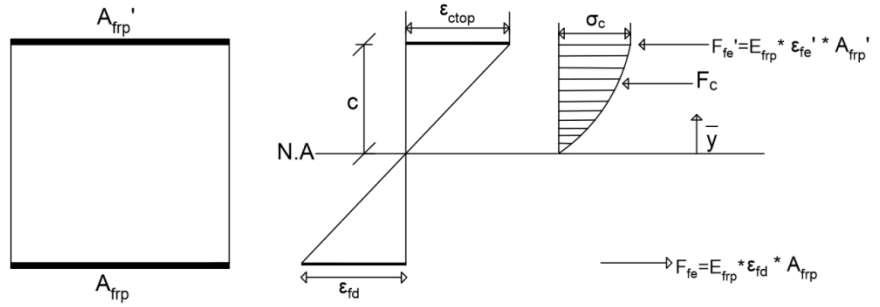

Figure 3.12: Stress-strain profile for FRP debonding (ascending portion)

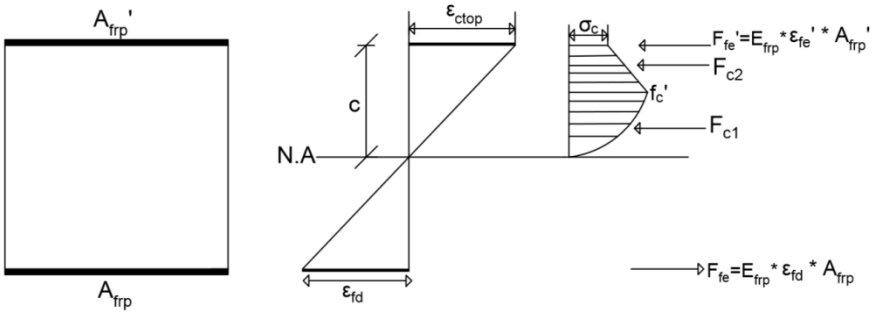

Figure 3.13: Stress-strain profile for FRP debonding (descending portion)

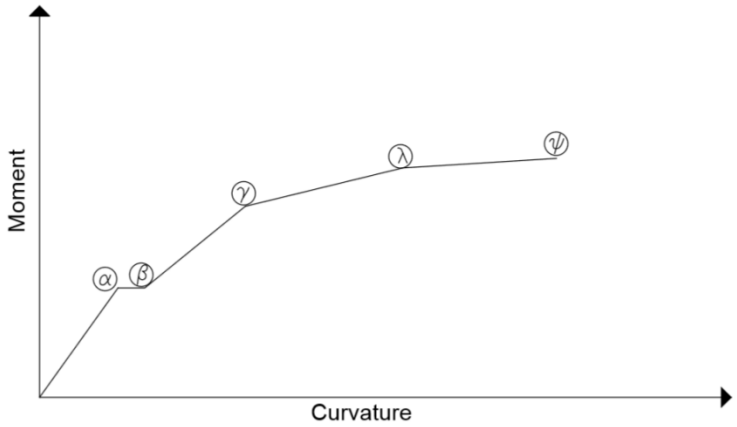

Figure 3.14: Typical moment-curvature curve for steel reinforced sections

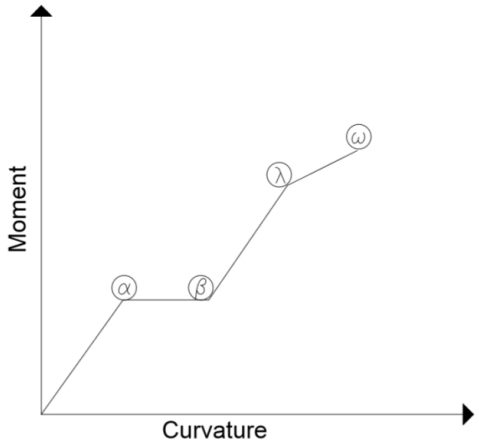

Figure 3.15: Typical moment-curvature curve for FRP reinforced sections

The failure modes represented by the letters in Figures 3.14 and 3.15 are explained in Table 3.1.

Table 3.1: Failure modes used in moment-curvature diagrams

Notation	**Explanation**
α	Prior to cracking
β	After cracking
γ	Yielding
λ	f_c' becomes maximum
ψ	AAC crushing
ω	AAC crushing or FRP debonding

3.4 Validation of the Moment-Curvature Analysis

Moment-curvature analysis results were compared by using the results from SAP2000 to check whether the analytical program provides sufficient degree of accuracy or not.

Material properties, section geometries and reinforcement configurations used in experimental tests are shown for reference specimens in Figure 3.16 and Figure 3.17, respectively. Figure 3.18 represents the comparison of moment-curvature analysis calculated by analytical program and SAP2000 software for steel reinforced AAC test beams. This figure clearly indicates that a good agreement between SAP2000 and analytical modeling was provided for both section geometries.

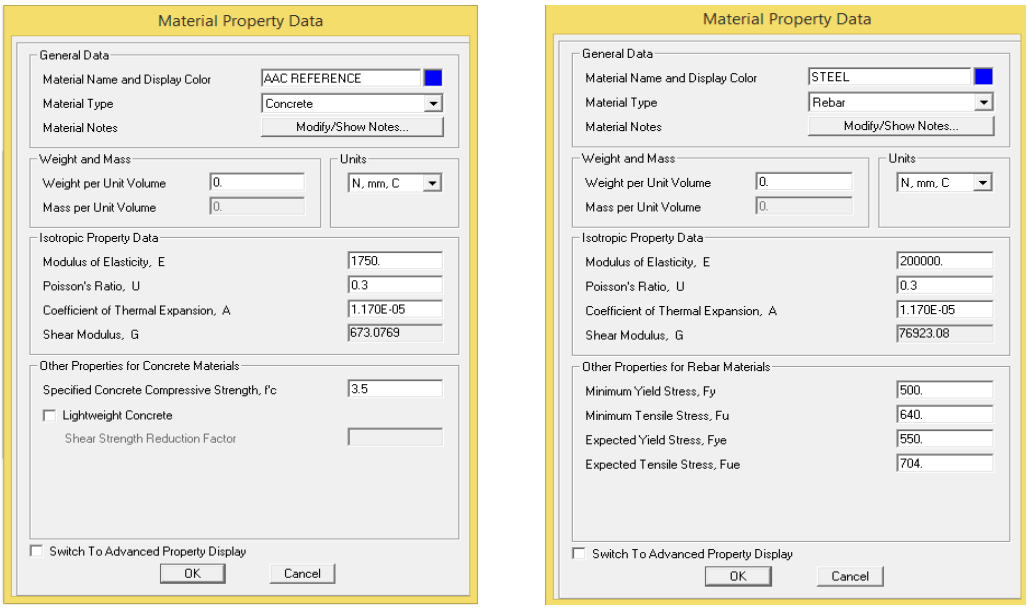

Figure 3.16: Material properties of reference specimens

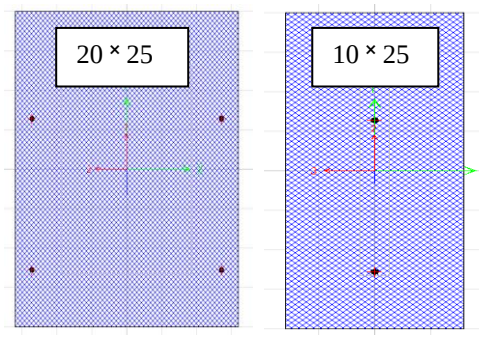

Figure 3.17: Reinforcement configurations of the reference specimens

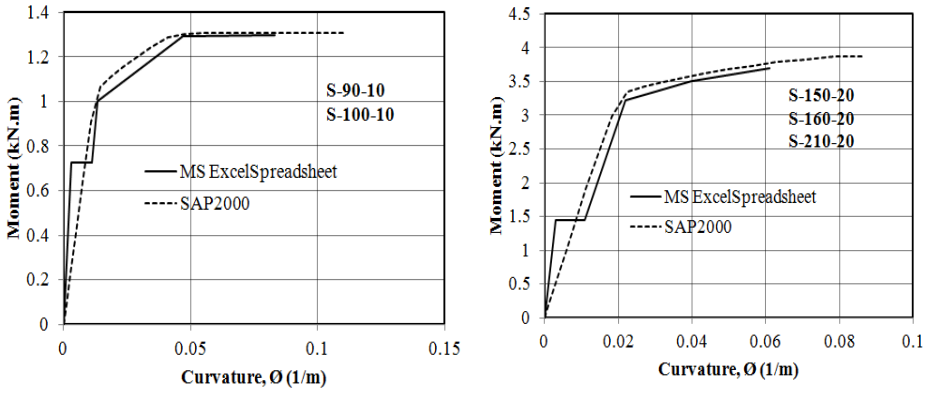

Figure 3.18: Moment-curvature comparison based on SAP2000 and analytical modeling for steel reinforced specimens

3.5 Load-Displacement Analysis

Typical load-displacement curves are presented in Figures 3.19 and 3.20 for steel reinforced and fiber-reinforced sections, respectively. Some critical locations on these response curves are shown. The explanations are given in Table 3.2 for these locations. Also, meanings of the abbreviations used in curvature diagram (Figure 3.21) are given in Table 3.3.

Moment area theorem was used to compute the load-displacement response of the members by using M-Ø results. Following steps were applied for this purpose:

1- Obtain moment capacity of the critical location symbolized by the listed number/letter in Table 3.2 for steel reinforced and fiber reinforced specimens, respectively.

2- Draw the moment diagram and construct curvature diagram (Figure 3.21).

3- Draw a tangent line passing through point "C" , find the moment of area under the curvature diagram with respect to point "C" and compute maximum deflection denoted by "Δ" (Figure 3.21).

4- Calculate the moment capacity of the next critical location and go to step-2.

5- Plot load-displacement graph.

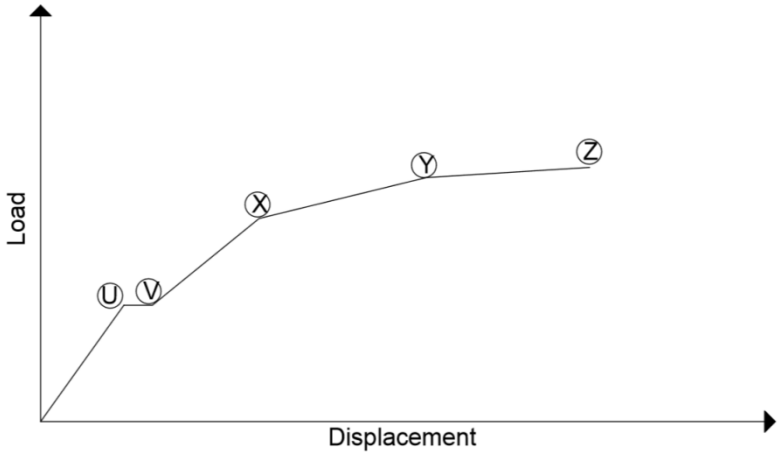

Figure 3.19: Typical load-displacement curve for steel-reinforced sections

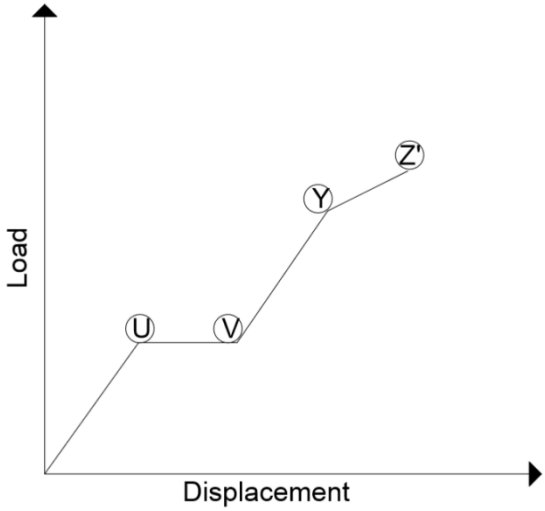

Figure 3.20: Typical load-displacement curve for fiber-reinforced sections

Table 3.2: Critical locations used in load-displacement curves

Notation	**Explanation**
U	Prior to cracking
V	After cracking
X	Yielding
Y	f_c' becomes maximum
Z	AAC crushing
Z'	AAC crushing or FRP debonding

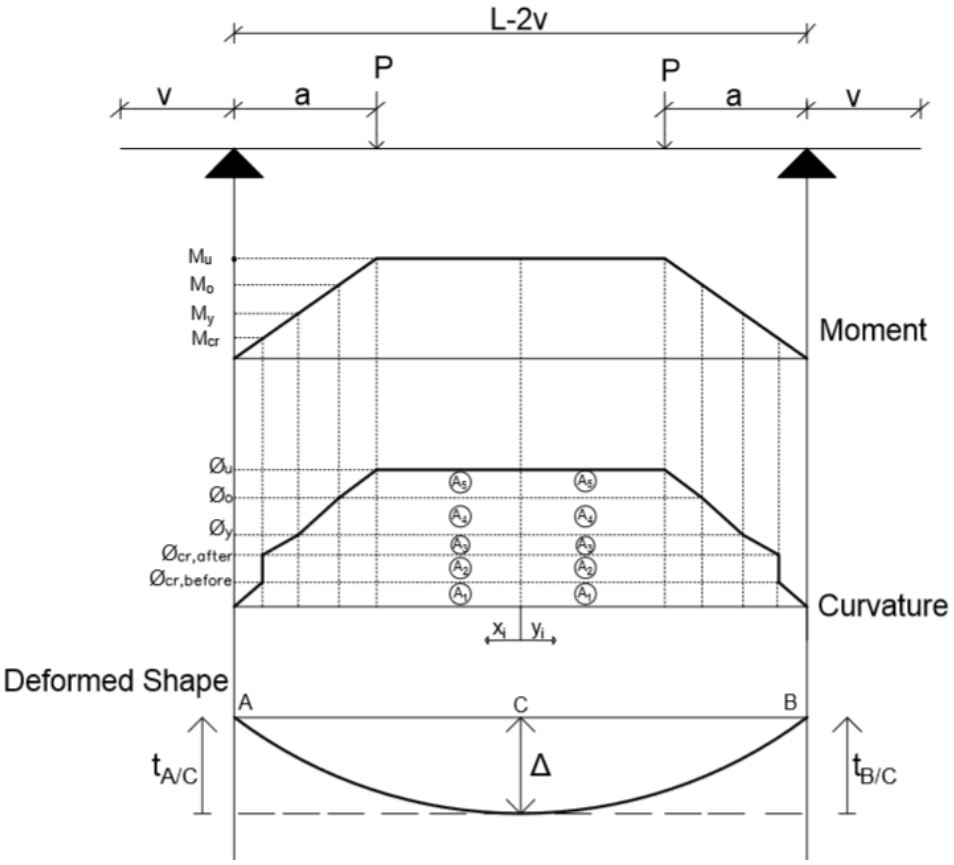

Figure 3.21: Curvature diagram for steel and FRP reinforced specimens

Table 3.3: Abbreviations used in curvature diagrams

Abbreviation	**Explanation**
M_{cr}	Moment at which specimen cracks
M_y	Moment at which steel yields
M_o	Moment at which f_c' becomes maximum
M_u	Moment at which specimen fails (AAC crushing or FRP debonding)
$Ø_{cr,before}$	Curvature at which before cracking
$Ø_{cr,after}$	Curvature at which after cracking
$Ø_y$	Curvature at which steel yields
$Ø_o$	Curvature at which f_c becomes maximum
$Ø_u$	Curvature at which specimen fails (AAC crushing or FRP debonding)

3.6 Comparison of Results

Experimental and analytical results are compared in this part. Load-displacement graphs obtained from experimental and analytical results are shown in Figure 3.22 and Figure 3.23 for reference and composite specimens, respectively. As seen from Figure 3.23, some geometrical shapes are used to identify important points. For example, "triangle " indicates load-displacement point at the test load that would be caused by the FRP debonding. These strain values were back-calculated by using the analytical modeling. In addition to this, "circle" represents the load-deflection point that corresponds to the maximum rupture strain specified by manufacturer.

Apart from those, there was no available experimental data to compare with the analytical moment-curvature results. For this reason, only load-displacement relation between experimental results and analytical modeling was compared herein for the test specimens. Moment-curvature responses of the test specimens are presented in Appendix C.

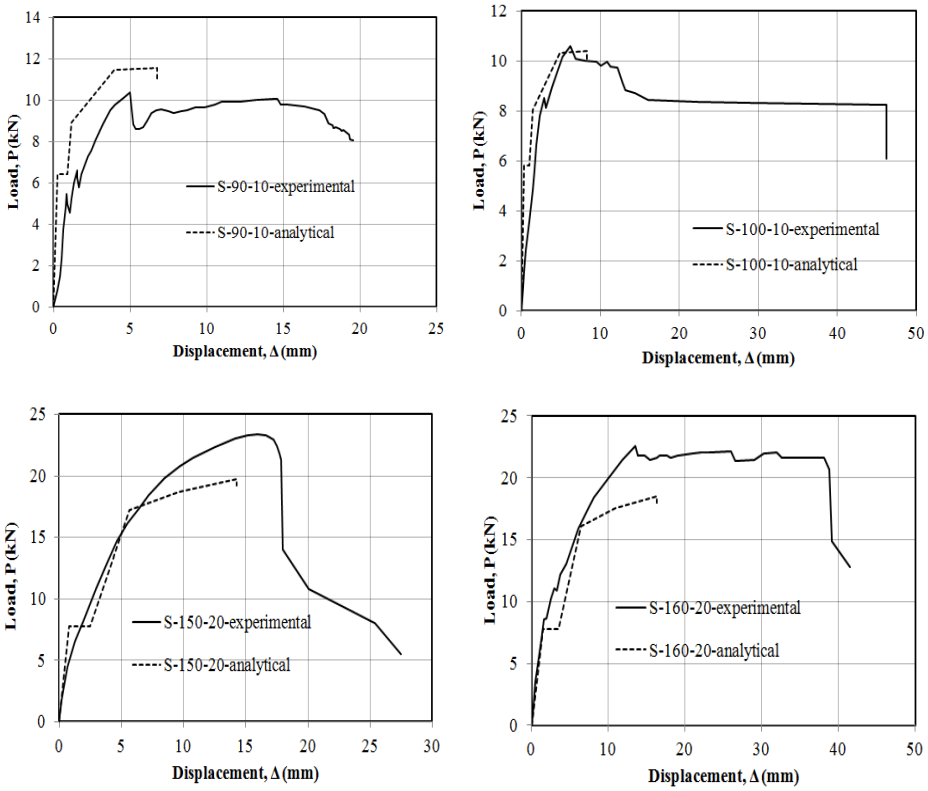

Figure 3.22: Comparison of load-displacement relation between the experimental results and analytical model for reference specimens

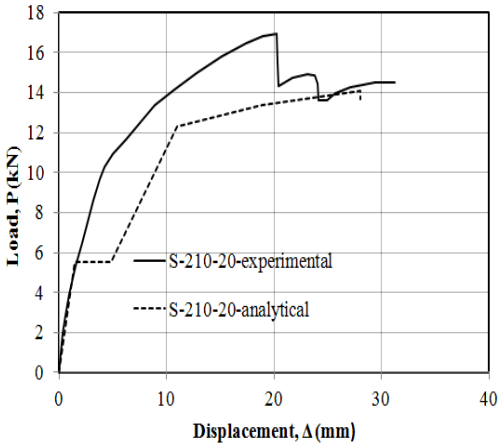

Figure 3.22: Comparison of load-displacement relation between the experimental results and analytical model for reference specimens (cont'd)

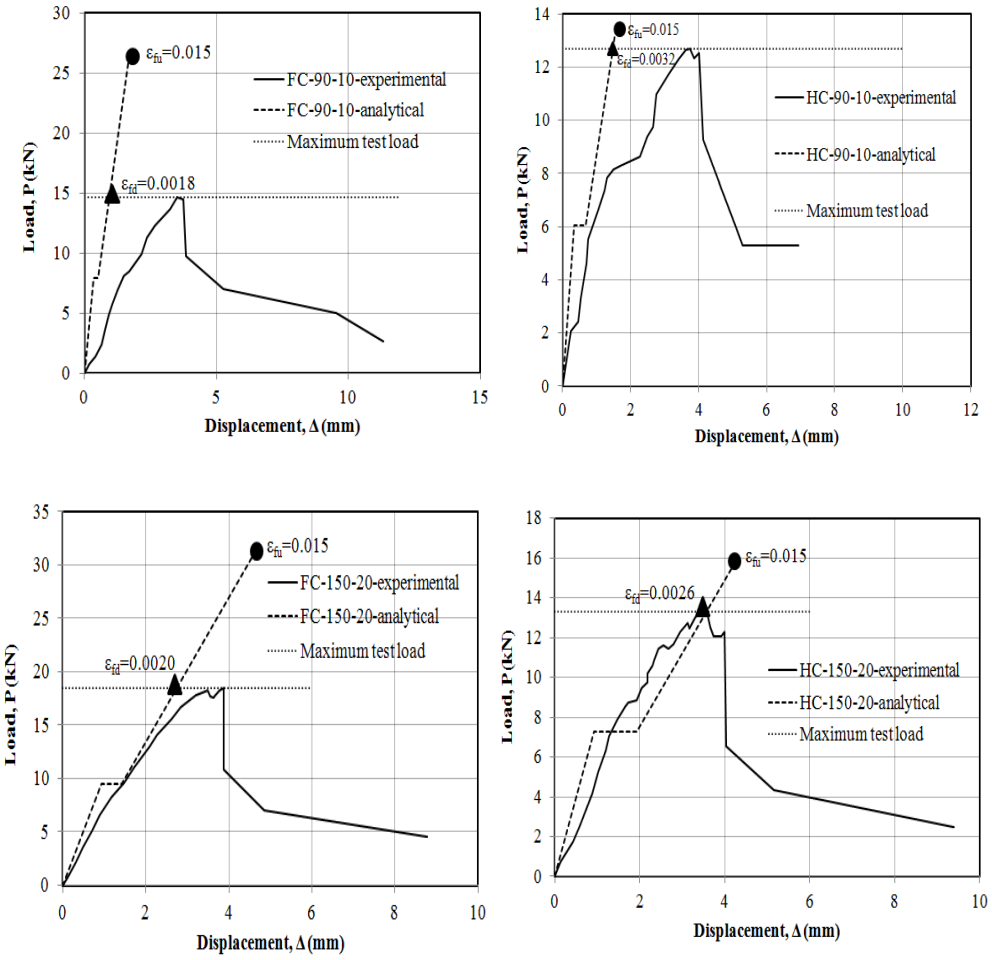

Figure 3.23: Comparison of load-displacement relation between the experimental results and analytical model for composite specimens

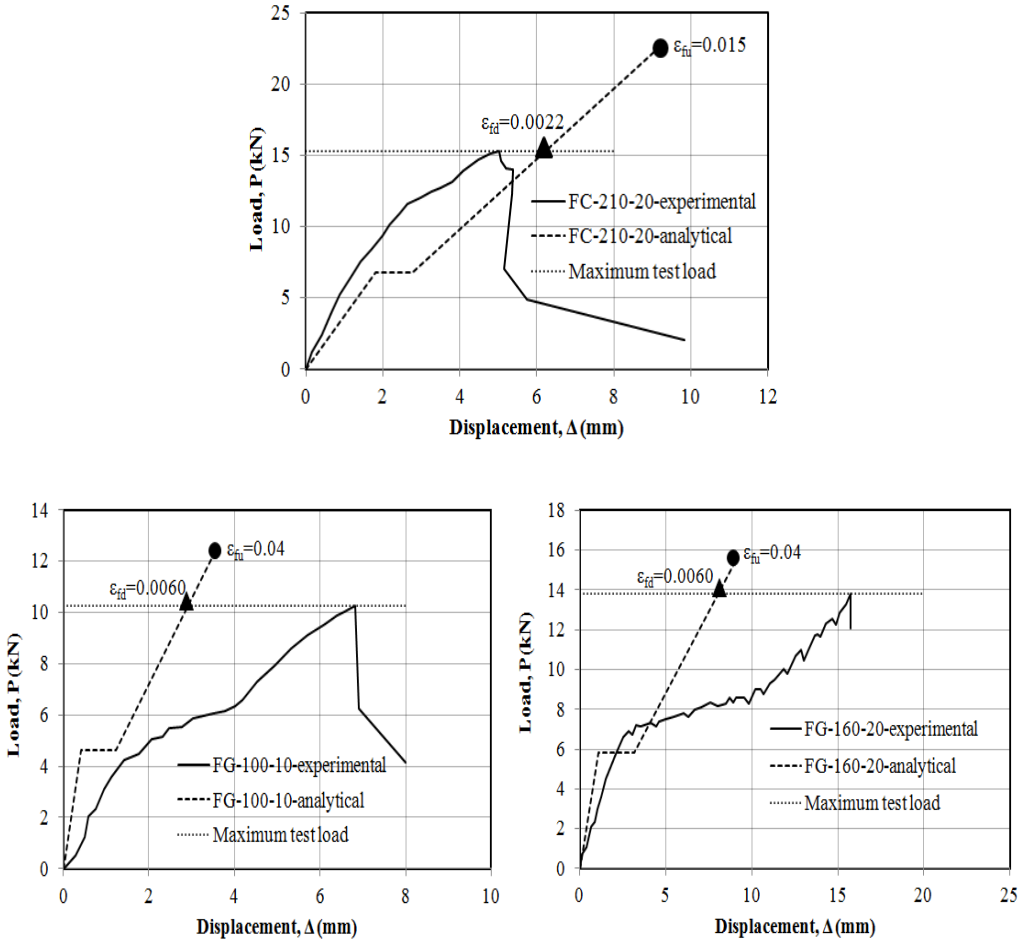

Figure 3.23: Comparison of load-displacement relation between the experimental results and analytical model for composite specimens (cont'd)

First evaluation was done for steel reinforced specimens. According to Figure 3.22, it is seen that load carrying capacities calculated by means of analytical modeling were in general agreement with the experimental results especially for the specimens having the width of 10 cm. On the other hand, analytical modeling slightly underestimated the load capacities for S-150-20, S-160-20 and S-160-20 relative to the experimental results. In other words, estimations were on the safe side. The reason behind this result can be due to neglecting strain hardening stage of steel in the analytical modeling. In addition to this, it is important to note that the experimental and theoretical secant stiffness values were quite close to each other. These observations provided confidence on the analytical modeling.

Secondly, similar evaluations were made for the composite specimens. Following Figure 3.23, load capacities seemed to be significantly different between the analytical

modeling and test results if one assumes the ultimate strength to be governed by FRP rupture. However, it should be known that the crucial point to evaluate this result mainly depends on debonding strain. According to Table 3.4, it is seen that usable strains back-calculated by using the test results and analytical modeling were smaller than those suggested by ACI 440.2R-16. In other words, it can be considered that ACI would not provide conservative designs based on limited test data. Apart from those, when "FC" and "HC" were taken into consideration from Table 3.4, it was observed that usable strains were closer to the ACI debonding strain as the fiber amount increased. Besides, it is understood that theoretical secant stiffness values were acceptable compared to the results obtained from experiments except FC-90-10 and FG-100-10. As a result, it can be said that the analytical based calculations were reasonable when compared with the test results.

3.7 Design

Design charts were developed to guide the designers regarding the load carrying capacities of FRP reinforced AAC beams. Depending on the demanded uniform distributed loads, the most economical FRP schemes were proposed for the CFRP and GFRP bonded AAC specimens having different span lengths and cross section dimensions in these design charts prepared.

Average strain values presented in Table 3.4 and Figure 3.24 were computed by means of the back-calculated debonding strains. By using the lower bound (mean-standard deviation) values of these strains, debonding strains were recommended for "FC", "HC" and "FG" fiber types in the same table. Also, debonding strains suggested by ACI 440 were calculated by using Equation 3.1 for fiber types and these values were proceeded into Table 3.4.

When proposed design strains were compared with the ones suggested by ACI, it is seen that ACI was not conservative. In other words, design strains recommended were in the safe side. However, it should be noted that the compressive strength ranges of AAC were quite narrow compared to reinforced concrete. Also, ACI is a design provision mainly used for RC members instead of light-weight concrete like AAC.

$$\varepsilon_{fd} = 0.41 * \sqrt{\frac{f_c'}{n_{frp} * t_{frp} * E_{frp}}} \leq 0.9 * \varepsilon_{fu} \qquad (3.1)$$

where:

ε_{fd} is the design debonding strain

ε_{fu} is the rupture strain specified by the manufacturer

n_{frp} is the number of fiber layer

E_{frp} is the modulus of elasticity of fiber

t_{frp} is the fiber thickness

Table 3.4: The comparison of recommended debonding strain with ACI 440

Fiber type	Specimen Label	Strain	Average strain	Standard deviation	Design strain	ACI 440 design debonding strain
FC	FC-90-10	0.0018	0.0020	0.00016	0.0018	0.0033
	FC-150-20	0.0020				
	FC-210-20	0.0022				
HC	HC-90-10	0.0032	0.0029	0.00020	0.0027	0.0033
	HC-150-20	0.0026				
FG	FG-100-10	0.0060	0.0060	-	0.0060	0.0065
	FG-160-20	0.0060				

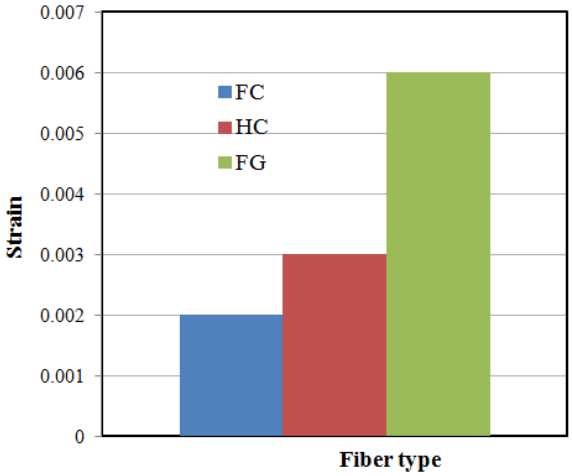

Figure 3.24: Average strain values for different fiber applications

Apart from those, when CFRP bonded test specimens in this study were considered, it is seen that the ratio of beam width to fiber width was different depending on fiber application type (i.e; full, half). On the other hand, material properties (such as AAC compressive strength, tensile strength of FRP, layer thickness of FRP) were the same. From this point of view, it was considered that debonding equations changing with respect to beam width to fiber width ratio can be constructed. As a result, Equation 3.2 was recommended for the AAC specimens composed of CFRP laminates. The constant number in this equation was determined by using design strain values given in Table 3.4 for "FC" and "HC" fiber types.

However, it is noted that fibers were applied throughout the full width of the section for the test specimens bonded by GFRP. In addition to having identical material properties, beam width to fiber width ratio was also the same for all GFRP bonded specimens as opposed to the ones used with CFRP. In this case, Equation 3.2 played an important role regarding the organisation of Equation 3.3 proposed for the GFRP reinforced AAC specimens.

In the scope of the experiments conducted in this study, all the composite specimens had single layer FRP as explained before. In addition to this, previous studies and ACI 440 revealed that the number of fiber layer is an important parameter affecting the debonding strain. For this reason, "n_{frp}" factor was also involved into these recommended equations as in the form of ACI 440.

$$\varepsilon_{cfrp} = 0.0009\left(1 + \frac{w_b}{w_{frp}}\right) / \sqrt{n_{frp}} \leq 0.9^* \varepsilon_{fu} \quad (3.2)$$

$$\varepsilon_{gfrp} = 0.0030\left(1 + \frac{w_b}{w_{frp}}\right) / \sqrt{n_{frp}} \leq 0.9^* \varepsilon_{fu} \quad (3.3)$$

where:

w_b is the specimen width

w_{frp} is the fiber width

ε_{cfrp} is the debonding strain for CFRP bonded specimens

ε_{gfrp} is the debonding strain for GFRP bonded specimens

The important points related to design charts are explained as follows:

- All the explanations given in "analytical model" was also valid for these design charts prepared.
- The mechanical and physical properties of the materials used in these charts were identical with the composite specimens tested during the experiments (i.e; fiber thickness, elasticity modulus of FRP/AAC, fiber tensile strength, AAC compressive strength).
- "q_{all}" is the uniform distributed load acting on the span length (Figure 3.25). This load implies that the allowable load carrying capacity of the specimens. To calculate this load, ultimate and serviceable limit states were taken into consideration. First, ultimate load capacities were calculated from the analytical modeling and divided by "1.35" which is the factored dead load case as per the regulations of Eurocode. Secondly, serviceable load capacity was obtained by considering displacement limit. The load that corresponds to (L_n/250) displacement value was determined as serviceable load capacity. The minimum load of both limit states were taken as load carrying capacity.

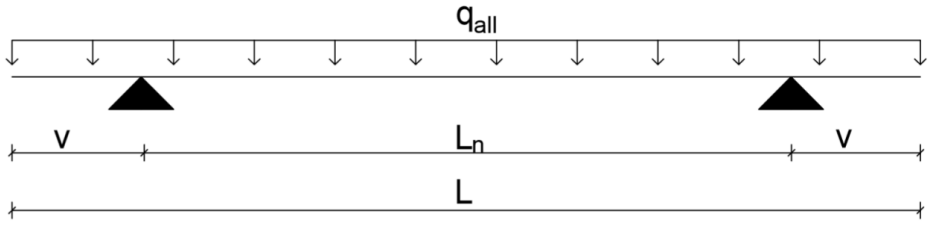

Figure 3.25: Loading system for design charts

Table 3.5: Design charts for composite specimens

Specimen dimensions				FRP type	FRP orientation		q_{all} (kN/m)				
W (mm)	H (mm)	L (mm)	v (mm)				0-6	6-8.5	8.5-11	11-13.5	13.5-16
100	250	1200	100	Carbon	Top	Layer number	1	1	1	1	1
						Fiber width (mm)	25	25	25	50	100
					Bottom	Layer number	1	2	3	2	3
						Fiber width (mm)	25	25	25	100	100
				Glass	Top	Layer number	1	1	1	1	-
						Fiber width (mm)	25	25	25	25	-
					Bottom	Layer number	1	1	3	3	-
						Fiber width (mm)	50	100	50	100	-

Table 3.5: Design charts for composite specimens (cont'd)

Specimen dimensions				FRP type	FRP orientation		q_{all} (kN/m)				
W (mm)	H (mm)	L (mm)	v (mm)				0-2	2-3	3-4	4-5	5-6
100	250	1800	100	Carbon	Top	Layer number	1	1	1	1	1
						Fiber width (mm)	25	25	25	25	100
					Bottom	Layer number	1	2	3	2	3
						Fiber width (mm)	25	25	25	100	100
				Glass	Top	Layer number	1	1	1	1	-
						Fiber width (mm)	25	25	25	25	-
					Bottom	Layer number	2	1	3	3	-
						Fiber width (mm)	25	100	50	100	-
Specimen dimensions				**FRP type**	**FRP orientation**		q_{all} (kN/m)				
W (mm)	**H (mm)**	**L (mm)**	**v (mm)**				**0-1.2**	**1.2-1.7**	**1.7-2.2**	**2.2-2.7**	**2.7-3.2**
100	250	2400	100	Carbon	Top	Layer number	1	1	1	1	1
						Fiber width (mm)	25	25	25	25	100
					Bottom	Layer number	1	2	3	2	3
						Fiber width (mm)	25	25	50	100	100
				Glass	Top	Layer number	1	3	1	1	-
						Fiber width (mm)	25	50	25	25	-
					Bottom	Layer number	1	1	2	3	-
						Fiber width (mm)	100	100	100	100	-
Specimen dimensions				**FRP type**	**FRP orientation**		q_{all} (kN/m)				
W (mm)	**H (mm)**	**L (mm)**	**v (mm)**				**0-0.4**	**0.4-0.8**	**0.8-1.2**	**1.2-1.6**	**1.6-2**
100	250	3000	100	Carbon	Top	Layer number	1	1	1	1	1
						Fiber width (mm)	25	50	25	50	100
					Bottom	Layer number	1	1	2	3	3
						Fiber width (mm)	25	50	50	50	100
				Glass	Top	Layer number	1	1	1	1	-
						Fiber width (mm)	25	25	100	100	-
					Bottom	Layer number	1	3	2	3	-
						Fiber width (mm)	25	50	100	100	-
Specimen dimensions				**FRP type**	**FRP orientation**		q_{all} (kN/m)				
W (mm)	**H (mm)**	**L (mm)**	**v (mm)**				**0-0.25**	**0.25-0.5**	**0.5-0.75**	**0.75-1**	**1-1.25**
100	250	3600	100	Carbon	Top	Layer number	1	1	1	1	1
						Fiber width (mm)	25	25	25	25	25
					Bottom	Layer number	1	1	2	3	3
						Fiber width (mm)	25	50	50	50	100
				Glass	Top	Layer number	1	1	1	1	-
						Fiber width (mm)	25	50	25	25	-
					Bottom	Layer number	1	3	3	3	-
						Fiber width (mm)	25	50	100	100	-
Specimen dimensions				**FRP type**	**FRP orientation**		q_{all} (kN/m)				
W (mm)	**H (mm)**	**L (mm)**	**v (mm)**				**0-12**	**12-17**	**17-22**	**22-27**	**27-32**
200	250	1200	100	Carbon	Top	Layer number	1	1	1	1	1
						Fiber width (mm)	50	50	50	100	200
					Bottom	Layer number	1	2	3	2	3
						Fiber width (mm)	50	50	50	200	200
				Glass	Top	Layer number	1	1	1	1	-
						Fiber width (mm)	50	50	50	50	-
					Bottom	Layer number	1	1	3	3	-
						Fiber width (mm)	100	200	100	200	-

Table 3.5: Design charts for composite specimens (cont'd)

Specimen dimensions				FRP type	FRP orientation		q_{all} (kN/m)				
W (mm)	H (mm)	L (mm)	v (mm)				0-4	4-6	6-8	8-10	10-12
200	250	1800	100	Carbon	Top	Layer number	1	1	1	1	1
						Fiber width (mm)	50	50	50	50	200
					Bottom	Layer number	1	2	3	2	3
						Fiber width (mm)	50	50	50	200	200
				Glass	Top	Layer number	1	1	1	1	-
						Fiber width (mm)	50	50	50	50	-
					Bottom	Layer number	2	1	3	3	-
						Fiber width (mm)	50	200	100	200	-
Specimen dimensions				**FRP type**	**FRP orientation**		**q_{all} (kN/m)**				
W (mm)	**H (mm)**	**L (mm)**	**v (mm)**				**0-2.4**	**2.4-3.4**	**3.4-4.4**	**4.4-5.4**	**5.4-6.4**
200	250	2400	100	Carbon	Top	Layer number	1	1	1	1	1
						Fiber width (mm)	50	50	50	50	100
					Bottom	Layer number	1	2	3	2	3
						Fiber width (mm)	50	50	100	100	100
				Glass	Top	Layer number	1	3	1	1	-
						Fiber width (mm)	50	100	50	50	-
					Bottom	Layer number	1	1	2	3	-
						Fiber width (mm)	200	200	200	200	-
Specimen dimensions				**FRP type**	**FRP orientation**		**q_{all} (kN/m)**				
W (mm)	**H (mm)**	**L (mm)**	**v (mm)**				**0-0.8**	**0.8-1.6**	**1.6-2.4**	**2.4-3.2**	**3.2-4**
200	250	3000	100	Carbon	Top	Layer number	1	1	1	1	1
						Fiber width (mm)	50	100	50	50	100
					Bottom	Layer number	1	1	2	3	3
						Fiber width (mm)	50	100	100	50	100
				Glass	Top	Layer number	1	1	1	1	-
						Fiber width (mm)	50	50	200	200	-
					Bottom	Layer number	1	3	2	3	-
						Fiber width (mm)	50	100	200	200	-
Specimen dimensions				**FRP type**	**FRP orientation**		**q_{all} (kN/m)**				
W (mm)	**H (mm)**	**L (mm)**	**v (mm)**				**0-0.5**	**0.5-1**	**1-1.5**	**1.5-2**	**2-2.5**
200	250	3600	100	Carbon	Top	Layer number	1	1	1	1	1
						Fiber width (mm)	50	50	50	50	50
					Bottom	Layer number	1	1	2	3	3
						Fiber width (mm)	50	100	100	100	200
				Glass	Top	Layer number	1	1	1	1	-
						Fiber width (mm)	50	100	50	50	-
					Bottom	Layer number	1	3	3	3	-
						Fiber width (mm)	50	100	200	200	-

360 analysis were conducted in the analytical program and results obtained were grouped according to the desired span lengths, cross section dimensions and fiber types in Table 3.5. According to this table, the computations were done for the specimens having either a width of 10 cm or 20 cm and a height of 25 cm. Five different span lengths (120, 180, 240, 300 and 360 cm) were taken into consideration. Also, the distance "v" was assumed as 10 cm for all cases.

In these design charts, the ratios of fiber width to beam width were determined as $\frac{1}{4}$, $\frac{1}{2}$ and 1 for both of top and bottom faces of the specimens. These options were increased by considering cross FRP distributions. As an example, while fiber width to beam width ratio is $\frac{1}{2}$ for bottom layer, the same ratio might be $\frac{1}{4}$ for top layer. However, it should be known that top FRP amount was always equal or smaller than bottom FRP amount for all the cases based on design charts prepared. Also, while the layer number can reach up to three for bottom fiber, one layer was assumed for the top fiber in each situation.

To estimate the design FRP amount, one must enter span length and cross section dimensions. Then, he/she reads the most economical value of FRP amount for CFRP and GFRP bonded specimens based on the demanded load ranges.

As a result, it is believed that these results may help engineers design FRP reinforced AAC beams for target loads.

CHAPTER 4

CONCLUSION

4.1 Conclusion

Load-displacement behavior of steel reinforced and fiber reinforced AAC beams were investigated in detail. Strength, ductility, energy absorption capacity and secant stiffness were the main test parameters. Also, an analytical modeling was developed to compute moment-curvature analysis and load-displacement behavior of steel reinforced and FRP reinforced AAC beams. Following key results can be drawn from this study:

- All the reference test specimens failed in AAC crushing after steel yielding. In other words, tension controlled failure mechanism occurred for steel reinforced AAC beams.
- Among FRP reinforced AAC test specimens, FC-90-10a showed AAC crushing since AAC adhesive used for this specimen behaved in more ductile manner relative to epoxy-based adhesive. On the other hand, the failure mode was FRP debonding for all the other composite beams as a result of brittle characteristics of epoxy-based adhesive used.
- Moment-curvature analysis of the numerical modeling was validated by SAP2000 for steel reinforced specimens.
- The load-displacement estimations computed by the analytical modeling were highly compatible with the test results. This situation indicates that the acceptable accuracy level was obtained.
- For "FC", "HC" and "FG" fiber types, usable debonding strains were recommended. It was observed that recommended debonding strains were smaller than to the ones suggested by ACI 440. This result indicates that design strains proposed were conservative.

- For design purposes, debonding strain equations depending on the beam width to fiber width ratio and fiber layer number were proposed for the CFRP and GFRP bonded AAC beams.
- By means of these recommended debonding strain equations, design charts were constructed. In these design charts, according to the demanded uniform load capacity ranges, economically reasonable FRP schemes were proposed for CFRP/GFRP bonded AAC beams having different span lengths and cross section dimensions.
- It is thought that the results obtained from the design charts might guide the designers interested in FRP bonded AAC beams.

REFERENCES

ACI 440.2R (2016), American Concrete Institute, "Design and Construction of Externally Bonded FRP Systems".

Akın, E. (2011), "Strengthening of Brick Infilled RC Frames with CFRP Reinforcement-General Principles ", Ph.D Thesis, Middle East Technical University, Ankara, Turkey.

Alakoc, C.A. (1999), "An Experimental Investigation on Autoclaved Aerated Concrete Blocks and Walls", Master Thesis, Middle East Technical University, Ankara, Turkey.

Camlı, U.S. (2005), "Anchorage Strength of Fiber Reinforced Polymers ", Master Thesis, Middle East Technical University, Ankara, Turkey.

Chaipanich, A., Chindaprasirt, P. (2015), "The properties and durability of autoclaved aerated concrete masonry blocks", *Eco-efficient Masonry Bricks and Blocks*, 215-230.

Hamad, A.J. (2014), "Materials, Production, Properties and Application of Aerated Lightweight Concrete: Review:", *International Journal of Materials Science and Engineering Vol.2*, 152-157.

Hognestad, E. (1951), "A study of combined bending and axial load in reinforced concrete members", *University of Illinois Bulletin. Vol. 49*, No. 22.

Matthys, J.H. , Barnett, R.E. (2004), "New Masonry Product for the US Designer Emerges-Autoclaved Aerated Concrete", *ASCE Structures*, 1-11.

Memari, A.M., Lepage, A., Setthachayanon, J. (2010), "An experimental study of autoclaved aerated concrete lintels strengthened with externally bonded glass FRP", *Journal of Reinforced Plastics and Composites*, 29 (22) 3322-3337.

Mousa, M.A., Uddin, N. (2009), "Experimental and analytical study of carbon fiber-reinforced polymer (FRP) / autoclaved aerated concrete (AAC) sandwich panels", *Engineering Structures*, 31 (2009) 2337-2344.

Nanni, A., Luca, A.D., Zadeh, H.J. (2014), " Reinforced concrete with FRP bars: Mechanics and Design", Boca Raton, CRC Press.

Norris, T., Saadetmanesh, H., Ehsani, M.R. (1997), "Shear and flexural strengthening of R/C beams with carbon fiber sheets", *Journal of Structural Engineering*, 903-911.

Ozcan, O. (2009), "Improving Ductility and Shear Capacity of Reinforced Concrete Columns with Carbon Fiber Polymer ", Ph.D Thesis, Middle East Technical University, Ankara, Turkey.

Schober, G. (2011), "Porosity in autoclaved aerated concrete (AAC):A review on pore structure, types of porosity, measurement methods and effects of porosity on properties", *Cement Wapno Beton*, 39-43.

Teng, J.G., Chen, J.F., Smith, S.T., Lam, L. (2002), "FRP-strengthened RC structures", England, John Wiley & Sons, Ltd.

TS EN 12602:2015, “Prefabricated Reinforced Components of Autoclaved Aerated Concrete".

Yu, J., Shang, X., Lu, Z. (2006), "Efficiency of Externally Bonded L-Shaped Laminates in Strengthening Reinforced-Concrete Interior Beam-Column Joints", *J. Compos. Constr.*, 20 (3):04015064.

Wang, B., Wang, P., Chen, Y., Zhou, J., Kong, X., Wu, H., Fan, H. , Jin, F. (2017), "Blast responses of CFRP strengthened autoclaved aerated cellular concrete panels", *Construction and Building Materials*, 157 (2017) 226-236.

.

APPENDIX A

STEEL REINFORCED SECTION ANALYSIS

All possible failure modes are mathematically explained in order to clarify the calculations behind analytical modeling. Solution procedure of steel reinforced sections is illustrated in this part.

A.1 Prior to Cracking

A.1.1 Two Layers Solution

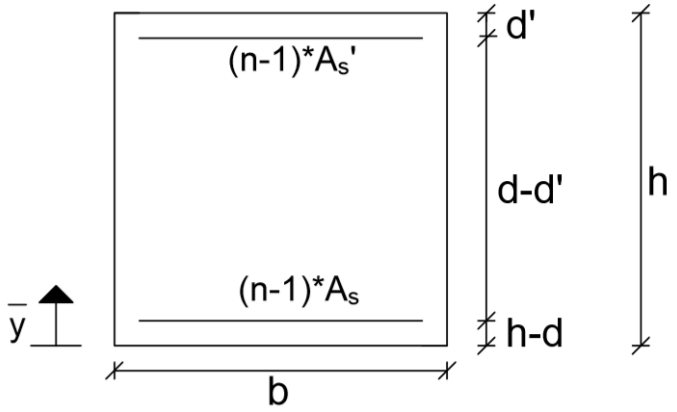

Figure A.1:Section analysis for prior to cracking case

$n = \frac{E_s}{E_c}$ $f_{ctf,d} = \frac{f_{ctf,k}}{\gamma_M}$ $M_{cr} = \frac{f_{ctf,d} * I_{tr}}{\bar{y}}$ $\emptyset_{cr} = \frac{M_{cr}}{E_c * I_{tr}}$

$$\bar{y} = \frac{(n-1)*A_s'*(h-d') + b*h*\frac{h}{2} + (n-1)*A_s*(h-d)}{b*h + (n-1)*A_s + (n-1)*A_s'}$$

$$I_{tr} = \frac{1}{12}bh^3 + bh(\frac{h}{2} - \bar{y})^2 + A_s(n-1)(\bar{y} - h + d)^2 + A_s'(n-1)(h - d' - \bar{y})^2$$

A.1.2 One Layer Solution

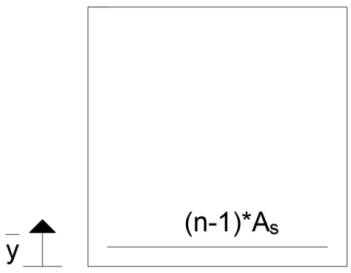

Figure A.2: Section analysis for prior to cracking case

$n = \frac{E_s}{E_c}$ $f_{ctf,d} = \frac{f_{ctf,k}}{\gamma_M}$ $M_{cr} = \frac{f_{ctf,d} * I_{tr}}{\bar{y}}$ $Ø_{cr} = \frac{M_{cr}}{E_c * I_{tr}}$

$$\bar{y} = \frac{b*h*\frac{h}{2} + (n-1)*A_s*(h-d)}{b*h+(n-1)*A_s}$$

$$I_{tr} = \frac{1}{12}bh^3 + bh(\frac{h}{2} - \bar{y})^2 + A_s(n-1)(\bar{y} - h + d)^2$$

A.2 After Cracking

A.2.1 Two Layers Solution

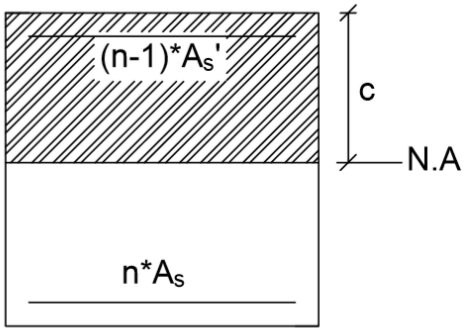

Figure A.3: Section analysis for after cracking case

Force Equilibrium:

$bc\frac{c}{2} + (n-1)A_s'(c-d') = nA_s(d-c)$

$bc^2 + 2(n-1)A_s'(c-d') = 2nA_s(d-c)$

$bc^2 + c(2nA_s' - 2A_s' + 2nA_s) - 2(A_s'nd' - A_s'd + A_sd) = 0$ (A.1)

If (A.1) is expressed in ($Ax^2 + Bx + C$) form, the constants are obtained as follows:

$A = b$

$B = 2nA_s' + 2nA_s$

$C = -2n(A_s'd' + A_sd)$

$\Delta = 4n^2(A_s + A_s')^2 + 8bn(A_s'd' + A_sd)$

$c = \frac{-2n(A_s + A_s') + \sqrt{\Delta}}{2b}$

$I_{cr} = \frac{1}{3}bc^3 + (n-1)A_s'(c-d')^2 + nA_s(d-c)^2$ $\qquad$ $Ø_{cr} = \frac{M_{cr}}{E_c * I_{cr}}$

A.2.2 One Layer Solution

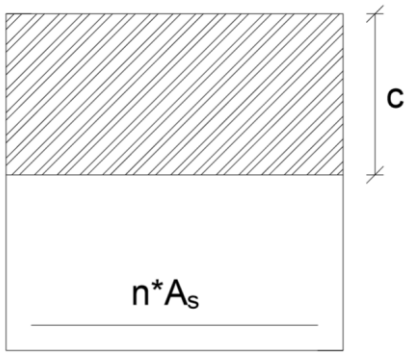

Figure A.4: Section analysis for after cracking case

Force Equilibrium:

$bc\frac{c}{2} = nA_s(d-c)$

$bc^2 = 2nA_s(d-c)$

$bc^2 + 2nA_sc - 2nA_sd = 0$ $\qquad$ (A.2)

If (A.2) is expressed in ($Ax^2 + Bx + C$) form, the constants are obtained as follows:

$A = b$

$B = 2nA_s$

$C = -2nA_sd$

$\Delta = 4n^2A_s^2 + 8bnA_sd$ $\qquad$ $c = \frac{-2nA_s + \sqrt{\Delta}}{2b}$

$I_{cr} = \frac{1}{3}bc^3 + nA_s(d-c)^2$ $\qquad$ $Ø_{cr} = \frac{M_{cr}}{E_c * I_{cr}}$

A.3 Yielding ($\varepsilon_s=\varepsilon_{sy}$)

A.3.1 Yielding occurs in the ascending portion ($\varepsilon_{ctop} < \varepsilon_{co}$)

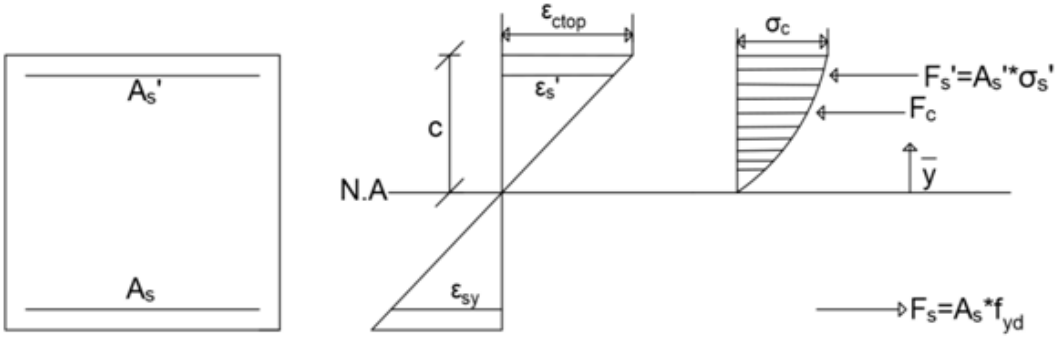

Figure A.5: Stress-strain profile for steel yielding case

$$\sigma(\varepsilon) = f_c'\left[\frac{2\varepsilon}{\varepsilon_{co}} - \left(\frac{\varepsilon}{\varepsilon_{co}}\right)^2\right]$$

$$F_c = \frac{bcf_c'}{\varepsilon_{ctop}}\int_0^{\varepsilon_{ctop}} \sigma(\varepsilon)d\varepsilon$$

$$= \frac{bcf_c'}{\varepsilon_{ctop}}\int_0^{\varepsilon_{ctop}}\left[\frac{2\varepsilon}{\varepsilon_{co}} - (\frac{\varepsilon}{\varepsilon_{co}})^2\right]d\varepsilon$$

$$= \frac{bcf_c'}{\varepsilon_{ctop}}(\frac{{\varepsilon_{ctop}}^2}{\varepsilon_{co}} - \frac{{\varepsilon_{ctop}}^3}{3{\varepsilon_{co}}^2})$$

$$F_c = bcf_c'(\frac{\varepsilon_{ctop}}{\varepsilon_{co}} - \frac{{\varepsilon_{ctop}}^2}{3{\varepsilon_{co}}^2}) \qquad \text{(A.3)}$$

$$\bar{y} = \frac{\int_0^{\varepsilon_{ctop}} \varepsilon\sigma(\varepsilon)d\varepsilon}{\int_0^{\varepsilon_{ctop}} \sigma(\varepsilon)d\varepsilon}(\frac{c}{\varepsilon_{ctop}})$$

$$\bar{y} = \frac{\int_0^{\varepsilon_{ctop}}\left(\frac{2\varepsilon^2}{\varepsilon_{co}} - \frac{\varepsilon^3}{{\varepsilon_{co}}^2}\right)d\varepsilon}{\int_0^{\varepsilon_{ctop}}(\frac{2\varepsilon}{\varepsilon_{co}} - \frac{\varepsilon^2}{{\varepsilon_{co}}^2})d\varepsilon}\ (\frac{c}{\varepsilon_{ctop}})$$

$$\bar{y} = \left[\frac{\frac{2\varepsilon_{ctop}}{3\varepsilon_{co}} - \frac{{\varepsilon_{ctop}}^2}{4{\varepsilon_{co}}^2}}{\frac{\varepsilon_{ctop}}{\varepsilon_{co}} - \frac{{\varepsilon_{ctop}}^2}{3{\varepsilon_{co}}^2}}\right]c \qquad \text{(A.4)}$$

$$\frac{\varepsilon_s'}{\varepsilon_{sy}} = \frac{c-d'}{d-c} \qquad \frac{\varepsilon_{ctop}}{\varepsilon_{sy}} = \frac{c}{d-c}$$

$$\varepsilon_s' = \varepsilon_{sy}(\frac{c-d'}{d-c}) \qquad \varepsilon_{ctop} = \varepsilon_{sy}(\frac{c}{d-c})$$

$$\sigma_s' = E_s\varepsilon_{sy}(\frac{c-d'}{d-c}) \le f_{yd}$$

Since force equilibrium equation is expressed as third degree polynomial function, there are two cases to find the roots as explained below:

ALTERNATIVE-1 (ALL THE ROOTS ARE REEL)

- This is valid when "h" is equal or smaller than zero.

$f = \frac{3\frac{C}{A}-(\frac{B}{A})^2}{3}$ $g= \frac{2(\frac{B}{A})^3-9\frac{BC}{A^2}+27\frac{D}{A}}{27}$ $h = \frac{g^2}{4}+\frac{f^3}{27}$

$i = (\frac{g^2}{4} - h)^{0.5}$ $j = i^{\frac{1}{3}}$ $k = \arccos(\frac{-g}{2i})$

$L=-j$ $M = \cos(\frac{k}{3})$ $N = \sqrt{3}\sin(\frac{k}{3})$ $P = \frac{-B}{3A}$

$c_1 = 2jM + P$ $c_2 = L(M+N) + P$ $c_3 = L(M+N) - P$

ALTERNATIVE-2 (ONE ROOT IS REEL TWO ROOTS ARE COMPLEX)

- This is valid when "h" is greater than zero.

$f = \frac{3\frac{C}{A}-(\frac{B}{A})^2}{3}$ $g= \frac{2(\frac{B}{A})^3-9\frac{BC}{A^2}+27\frac{D}{A}}{27}$ $h = \frac{g^2}{4}+\frac{f^3}{27}$

$R= \frac{-g}{2}+\sqrt{h}$ $S= R^{\frac{1}{3}}$ $T=\frac{-g}{2}-\sqrt{h}$ $U= T^{\frac{1}{3}}$

$c_1 = S+U+P$

A.3.1.1 Assume compression steel also has yielded

$F_c = bcf_c'[\frac{\varepsilon_{sy}(\frac{c}{d-c})}{\varepsilon_{co}} - \frac{\varepsilon_{sy}{}^2(\frac{c}{d-c})^2}{3\varepsilon_{co}{}^2}]$

$F_c = \frac{3bc^2f_c'\varepsilon_{sy}\varepsilon_{co}(d-c)-bcf_c'\varepsilon_{sy}{}^2c^2}{3\varepsilon_{co}{}^2(d-c)^2}$

$F_s = A_sf_{yd}$

$F_s' = A_s'f_{yd}$

Force Equilibrium:

$F_s' + F_c - F_s = 0$

$$A_s'f_{yd} + \frac{3bc^2f_c'\varepsilon_{sy}\varepsilon_{co}(d-c)-bcf_c'\varepsilon_{sy}{}^2c^2}{3\varepsilon_{co}{}^2(d-c)^2} - f_{yd}A_s = 0 \qquad (A.5)$$

If (A.5) is expressed in terms of $Ax^3+Bx^2+Cx+D=0$, the coefficients are obtained as follows:

$A = -3bf_c'\varepsilon_{co}\varepsilon_{sy} - bf_c'\varepsilon_{sy}^2$

$B = 3bf_c'\varepsilon_{co}\varepsilon_{sy}d + 3A_s'f_{yd}\varepsilon_{co}^2 - 3A_sf_{yd}\varepsilon_{co}^2$

$C = -6A_s'f_{yd}\varepsilon_{co}^2d + 6A_sf_{yd}\varepsilon_{co}^2d$

$D = 3A_s'f_{yd}\varepsilon_{co}^2d^2 - 3A_sf_{yd}\varepsilon_{co}^2d^2$

All the computational procedures are done to find the roots in the light of ALTERNATIVE-1 and ALTERNATIVE-2. Then,

$\varepsilon_s' = \varepsilon_{sy}(\frac{c-d'}{d-c})$ Check whether assumption is correct or not.

$\varepsilon_{ctop} = \varepsilon_{sy}(\frac{c}{d-c})$ Check whether assumption is correct or not.

- Even if one assumption is not verified, this alternative does not work.
- If both assumptions are verified together, this alternative works and moment is calculated with respect to centroid of concrete stress block. Then,

$M_y = F_s(d-c+\overline{y}) + F_s'(c-d'-\overline{y})$ $\quad \emptyset_y = \frac{\varepsilon_{ctop}}{c}$

A.3.1.2 Assume only tension steel has yielded

$F_c = \frac{3bc^2f_c'\varepsilon_{sy}\varepsilon_{co}(d-c)-bcf_c'\varepsilon_{sy}^2c^2}{3\varepsilon_{co}^2(d-c)^2}$

$F_s = A_sf_{yd}$

$F_s' = A_s' E_s\varepsilon_{sy}(\frac{c-d'}{d-c})$

Force Equilibrium:

$F_s' + F_c - F_s = 0$

$A_s' E_s\varepsilon_{sy}(\frac{c-d'}{d-c}) + \frac{3bc^2f_c'\varepsilon_{sy}\varepsilon_{co}(d-c)-bcf_c'\varepsilon_{sy}^2c^2}{3\varepsilon_{co}^2(d-c)^2} - f_{yd}A_s = 0$ (A.6)

If (A.6) is expressed in terms of $Ax^3+Bx^2+Cx+D=0$, the coefficients are obtained as follows:

$A = -3bf_c'\varepsilon_{co}\varepsilon_{sy} - bf_c'\varepsilon_{sy}^2$

$B = 3bf_c'\varepsilon_{co}\varepsilon_{sy}d - 3E_s\varepsilon_{sy}\varepsilon_{co}^2A_s' - 3A_sf_{yd}\varepsilon_{co}^2$

$C = 3E_s\varepsilon_{sy}\varepsilon_{co}{}^2A_s{}'d + 3E_s\varepsilon_{sy}\varepsilon_{co}{}^2A_s{}'d' + 6A_sf_{yd}\varepsilon_{co}{}^2d$

$D = -3E_s\varepsilon_{sy}\varepsilon_{co}{}^2A_s{}'dd' - 3A_sf_{yd}\varepsilon_{co}{}^2d^2$

All the computational procedures are done to find the roots in the light of ALTERNATIVE-1 and ALTERNATIVE-2. Then,

$\varepsilon_s' = \varepsilon_{sy}(\frac{c-d'}{d-c})$ Check whether assumption is correct or not.

$\varepsilon_{ctop} = \varepsilon_{sy}(\frac{c}{d-c})$ Check whether assumption is correct or not.

- Even if one assumption is not verified, this alternative does not work.
- If both assumptions are verified together, this alternative works and moment is calculated with respect to centroid of concrete stress block.

$M_y = F_s(d-c+\bar{y}) + F_s'(c-d'-\bar{y})$ $\quad$ $\emptyset_y = \frac{\varepsilon_{ctop}}{c}$

A.3.1.3 No compression steel

$F_c = \frac{3bc^2f_c{}'\varepsilon_{sy}\varepsilon_{co}(d-c)-bcf_c{}'\varepsilon_{sy}{}^2c^2}{3\varepsilon_{co}{}^2(d-c)^2}$

$F_s = A_sf_{yd}$

Force Equilibrium:

$F_c - F_s = 0$

$\frac{3bc^2f_c{}'\varepsilon_{sy}\varepsilon_{co}(d-c)-bcf_c{}'\varepsilon_{sy}{}^2c^2}{3\varepsilon_{co}{}^2(d-c)^2} - f_{yd}A_s = 0$ $\quad$ (A.7)

If (A.7) is expressed in terms of $Ax^3+Bx^2+Cx+D=0$, the coefficients are obtained as follows:

$A = -3bf_c{}'\varepsilon_{co}\varepsilon_{sy} - bf_c{}'\varepsilon_{sy}{}^2$

$B = 3bf_c{}'\varepsilon_{co}\varepsilon_{sy}d - 3A_sf_{yd}\varepsilon_{co}{}^2$

$C = 6A_sf_{yd}\varepsilon_{co}{}^2d$

$D = -3A_sf_{yd}\varepsilon_{co}{}^2d^2$

All the computational procedures are done to find the roots in the light of ALTERNATIVE-1 and ALTERNATIVE-2.

$\varepsilon_{ctop} = \varepsilon_{sy}(\frac{c}{d-c})$ Check whether assumption is correct or not.

- If the assumption is verified, this alternative works and moment is calculated with respect to centroid of concrete stress block. Then,

$M_y = F_s(d-c+\overline{y})$ $\quad$ $Ø_y = \frac{\varepsilon_{ctop}}{c}$

A.3.2 Yielding occurs in the descending portion ($\varepsilon_{co} < \varepsilon_{ctop} < \varepsilon_{cu}$)

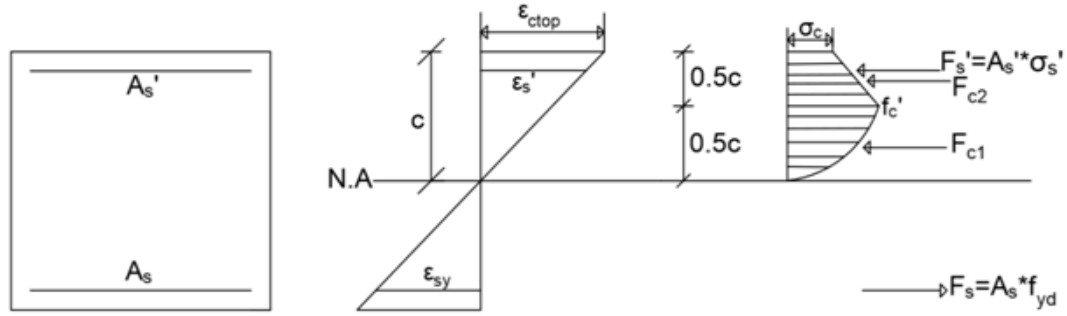

Figure A.6: Stress-strain profile for steel yielding case

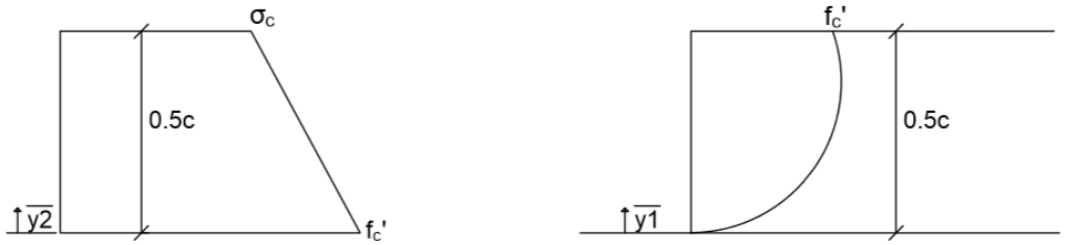

Figure A.7: Geometric center of ascending and descending portion of concrete stress block

$\sigma(\varepsilon) = f_c'(\frac{-0.15\varepsilon_{ctop}+\varepsilon_{cu}-0.85\varepsilon_{co}}{\varepsilon_{cu}-\varepsilon_{co}})$ $\quad$ for linear part of stress block.

Therefore,

$F_{c2} = 0.5[f_c' + (\frac{-0.15\varepsilon_{ctop}+\varepsilon_{cu}-0.85\varepsilon_{co}}{\varepsilon_{cu}-\varepsilon_{co}})f_c'](0.5bc)$

$F_{c2} = \frac{0.25bcf_c'}{\varepsilon_{cu}-\varepsilon_{co}}(2\varepsilon_{cu} - 1.85\varepsilon_{co} - 0.15\varepsilon_{ctop})$ $\quad$ (A.8)

$\overline{y2} = [\frac{(0.3333333333\sigma_c+0.1666666667f_c')}{(\sigma_c+f_c')}]c$ $\quad$ (A.9)

$\frac{\varepsilon_s'}{\varepsilon_{sy}} = \frac{c-d'}{d-c}$ $\qquad$ $\frac{\varepsilon_{ctop}}{\varepsilon_{sy}} = \frac{c}{d-c}$

$\varepsilon_s' = \varepsilon_{sy}(\frac{c-d'}{d-c})$ $\varepsilon_{ctop} = \varepsilon_{sy}(\frac{c}{d-c})$

$\sigma_s' = E_s\varepsilon_{sy}(\frac{c-d'}{d-c}) \leq f_{yd}$

$F_s' = E_s\varepsilon_{sy}\left(\frac{c-d'}{d-c}\right)A_s'$

$F_s = f_{yd}A_s$

To calculate F_{c1}, use (A.3) by putting "0.5c" instead of "c" and $\varepsilon_{ctop} = \varepsilon_{co}$. Then,

$F_{c1} = 0.3333333333f_c'bc$ (A.10)

To find $\overline{y1}$, put $\varepsilon_{ctop} = \varepsilon_{co}$ in (A.4). However ,the multiplier is "0.5c" instead of "c".

$\overline{y1} = 0.3125c$ (A.11)

A.3.2.1 Assume compression steel also has yielded

$F_c = F_{c1} + F_{c2} = 0.3333333333f_c'bc + \frac{0.25bcf_c'}{\varepsilon_{cu}-\varepsilon_{co}}(2\varepsilon_{cu} - 1.85\varepsilon_{co} - 0.15\varepsilon_{ctop})$

$F_s = A_sf_{yd}$

$F_s' = A_s'f_{yd}$

Force equilibrium is set as follows:

$F_c + F_s' - F_s = 0$

$0.3333333333f_c'bc + \frac{0.25bcf_c'}{\varepsilon_{cu}-\varepsilon_{co}}(2\varepsilon_{cu} - 1.85\varepsilon_{co} - 0.15\varepsilon_{ctop}) + A_s'f_{yd} - A_sf_{yd} = 0$ (A.12)

If (A.12) is expressed in $(Ax^2 + Bx + C)$ form, the constants are obtained as follows:

$A = -0.8333333333f_c'b\varepsilon_{cu} + 0.7958333333\ f_c'b\varepsilon_{co} - 0.0375\ f_c'b\varepsilon_{sy}$

$B = 0.8333333333f_c'b\varepsilon_{cu}d - 0.7958333333\ f_c'b\varepsilon_{co}d - A_s'f_{yd}\varepsilon_{cu} + A_s'f_{yd}\varepsilon_{co} + A_sf_{yd}\varepsilon_{cu} - A_sf_{yd}\varepsilon_{co}$

$C = A_s'f_{yd}\varepsilon_{cu}d - A_s'f_{yd}\varepsilon_{co}d - A_sf_{yd}\varepsilon_{cu}d + A_sf_{yd}\varepsilon_{co}d$

$\Delta = B^2 - 4AC$

$c_{1,2} = \frac{-B\pm\sqrt{\Delta}}{2A}$

$\varepsilon_s' = \varepsilon_{sy}(\frac{c-d'}{d-c})$ Check whether assumption is correct or not.

$\varepsilon_{ctop} = \varepsilon_{sy}(\frac{c}{d-c})$ Check whether assumption is correct or not.

- Even if one assumption is not verified, this alternative does not work.
- If both assumptions are verified together, this alternative works and moment is calculated with respect to centroid of concrete stress block. Then,

$M_y = F_s(d-0.5c+\overline{y2}) + F_s'(0.5c-d'-\overline{y2}) - F_{c1}(0.1875c+\overline{y2})$ $\quad \emptyset_y = \frac{\varepsilon_{ctop}}{c}$

A.3.2.2 Assume only tension steel has yielded

$F_c = F_{c1} + F_{c2} = 0.3333333333 f_c' bc + \frac{0.25bcf_c'}{\varepsilon_{cu}-\varepsilon_{co}}(2\varepsilon_{cu} - 1.85\varepsilon_{co} - 0.15\varepsilon_{ctop})$

$F_s = A_s f_{yd}$

$F_s' = A_s' E_s \varepsilon_{sy} (\frac{c-d'}{d-c})$

Force equilibrium is set as follows:

$F_c + F_s' - F_s = 0$

$0.3333333333 f_c' bc + \frac{0.25bcf_c'}{\varepsilon_{cu}-\varepsilon_{co}}(2\varepsilon_{cu} - 1.85\varepsilon_{co} - 0.15\varepsilon_{ctop}) + A_s' E_s \varepsilon_{sy} (\frac{c-d'}{d-c}) - A_s f_{yd} = 0$ (A.13)

If (A.13) is expressed in $(Ax^2 + Bx + C)$ form, the constants are obtained as follows:

$A = -0.8333333333 f_c' b\varepsilon_{cu} + 0.7958333333 f_c' b\varepsilon_{co} - 0.0375 f_c' b\varepsilon_{sy}$

$B = 0.8333333333 f_c' b\varepsilon_{cu} d - 0.7958333333 f_c' b\varepsilon_{co} d + A_s' E_s \varepsilon_{sy} \varepsilon_{cu} - A_s' E_s \varepsilon_{sy} \varepsilon_{co} + A_s f_{yd} \varepsilon_{cu} - A_s f_{yd} \varepsilon_{co}$

$C = -A_s' E_s \varepsilon_{sy} \varepsilon_{cu} d' + A_s' E_s \varepsilon_{sy} \varepsilon_{co} d' - A_s f_{yd} \varepsilon_{cu} d + A_s f_{yd} \varepsilon_{co} d$

$\Delta = B^2 - 4AC$

$c_{1,2} = \frac{-B \pm \sqrt{\Delta}}{2A}$

$\varepsilon_s' = \varepsilon_{sy}(\frac{c-d'}{d-c})$ Check whether assumption is correct or not.

$\varepsilon_{ctop} = \varepsilon_{sy}(\frac{c}{d-c})$ Check whether assumption is correct or not.

- Even if one assumption is not verified, this alternative does not work.
- If both assumptions are verified together, this alternative works and moment is calculated with respect to centroid of concrete stress block.

$M_y = F_s(d-0.5c+\overline{y2}) + F_s'(0.5c-d'-\overline{y2}) - F_{c1}(0.1875c+\overline{y2})$ $\quad \emptyset_y = \frac{\varepsilon_{ctop}}{c}$

A.3.2.3 No compression steel

$F_c = F_{c1} + F_{c2} = 0.3333333333 f_c' bc + \frac{0.25bcf_c'}{\varepsilon_{cu}-\varepsilon_{co}}(2\varepsilon_{cu} - 1.85\varepsilon_{co} - 0.15\varepsilon_{ctop})$

$F_s = A_s f_{yd}$

Force equilibrium is set as follows:

$F_c - F_s = 0$

$0.3333333333 f_c' bc + \frac{0.25bcf_c'}{\varepsilon_{cu}-\varepsilon_{co}}(2\varepsilon_{cu} - 1.85\varepsilon_{co} - 0.15\varepsilon_{ctop}) - A_s f_{yd} = 0$ (A.14)

If (A.14) is expressed in $(Ax^2 + Bx + C)$ form, the constants are obtained as follows:

$A = -0.8333333333 f_c' b\varepsilon_{cu} + 0.7958333333 f_c' b\varepsilon_{co} - 0.0375 f_c' b\varepsilon_{sy}$

$B = 0.8333333333 f_c' b\varepsilon_{cu} d - 0.7958333333 f_c' b\varepsilon_{co} d + A_s f_{yd}\varepsilon_{cu} - A_s f_{yd}\varepsilon_{co}$

$C = - A_s f_{yd}\varepsilon_{cu} d + A_s f_{yd}\varepsilon_{co} d$

$\Delta = B^2 - 4AC$

$c_{1,2} = \frac{-B \pm \sqrt{\Delta}}{2A}$

$\varepsilon_{ctop} = \varepsilon_{sy}(\frac{c}{d-c})$ Check whether assumption is correct or not.

- If assumption is verified, this alternative works and moment is calculated with respect to centroid of concrete stress block. Then,

$M_y = F_s(d - 0.5c + \overline{y2}) - F_{c1}(0.1875c + \overline{y2})$ $\quad \emptyset_y = \frac{\varepsilon_{ctop}}{c}$

A.4 AAC reaches its maximum compressive strength ($\varepsilon_{ctop}=\varepsilon_{co}$)

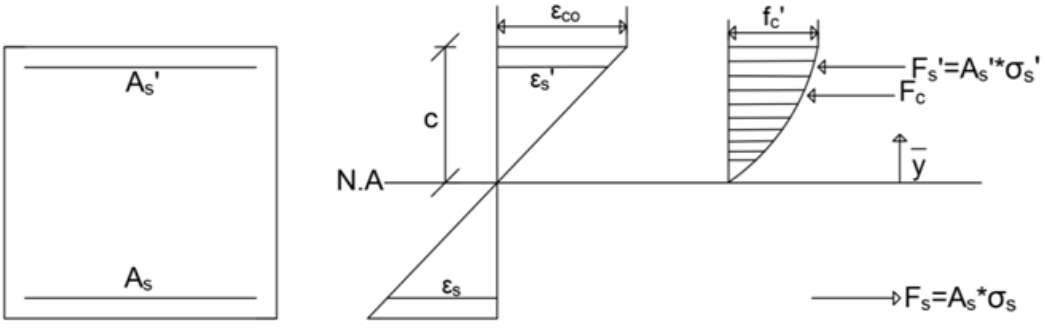

Figure A.8: Stress-strain profile at which $\varepsilon = \varepsilon_{co}$

$\frac{\varepsilon_s'}{\varepsilon_{co}} = \frac{c-d'}{c}$	$\frac{\varepsilon_s}{\varepsilon_{co}} = \frac{d-c}{c}$
$\varepsilon_s = \varepsilon_{co}(\frac{d-c}{c})$	$\varepsilon_s' = \varepsilon_{co}(\frac{c-d'}{c})$
$\sigma_s = E_s\varepsilon_{co}(\frac{d-c}{c}) \leq f_{yd}$	$\sigma_s' = E_s\varepsilon_{co}(\frac{c-d'}{c}) \leq f_{yd}$
$F_s = E_s\varepsilon_{co}\left(\frac{d-c}{c}\right)A_s$	$F_s' = E_s\varepsilon_{co}\left(\frac{c-d'}{c}\right)A_s'$

Put $\varepsilon_{ctop} = \varepsilon_{co}$ in (A.3).

$F_c = 0.6666666667 f_c'bc$ (A.15)

Put $\varepsilon_{ctop} = \varepsilon_{co}$ in (A.4). Then,

$\bar{y} = 0.625c$ (A.16)

A.4.1 Assume both steels have yielded

$F_c = 0.6666666667 f_c'bc$

$F_s = A_s f_{yd}$

$F_s' = A_s' f_{yd}$

Force equilibrium is set as follows:

$F_c + F_s' - F_s = 0$

$0.6666666667 f_c'bc + A_s' f_{yd} - A_s f_{yd} = 0$ (A.17)

$c = 1.5\frac{f_{yd}(A_s - A_s')}{bf_c'}$

$\varepsilon_s' = \varepsilon_{co}(\frac{c-d'}{c})$ Check whether assumption is correct or not.

$\varepsilon_s = \varepsilon_{co}(\frac{d-c}{c})$ Check whether assumption is correct or not.

- Even if one assumption is not verified, this alternative does not work.
- If both assumptions are verified together, this alternative works and moment is calculated with respect to centroid of concrete stress block. Then,

$M_o = F_s(d-0.375c) + F_s'(0.375c-d')$ $\quad \emptyset_o = \frac{\varepsilon_{co}}{c}$

A.4.2 Assume only tension steel has yielded

$F_c = 0.6666666667 f_c'bc$

$F_s = A_s f_{yd}$

$F_s' = A_s' E_s \varepsilon_{co} \left(\frac{c-d'}{c}\right)$

Force equilibrium is set as follows:

$F_c + F_s' - F_s = 0$

$0.6666666667 f_c' bc + A_s' E_s \varepsilon_{co} \left(\frac{c-d'}{c}\right) - A_s f_{yd} = 0$

$2f_c' bc^2 + (3E_s \varepsilon_{co} A_s' - 3A_s f_{yd})c - 3E_s \varepsilon_{co} A_s' d' = 0$ (A.18)

If (A.18) is expressed in $(Ax^2 + Bx + C)$ form, the constants are obtained as follows:

$A = 2f_c' b$

$B = 3E_s \varepsilon_{co} A_s' - 3A_s f_{yd}$

$C = -3E_s \varepsilon_{co} A_s' d'$

$\Delta = (3E_s \varepsilon_{co} A_s' - 3A_s f_{yd})^2 + 24 f_c' b E_s \varepsilon_{co} A_s' d'$

$c_{1,2} = \frac{-B \pm \sqrt{\Delta}}{2A}$

$\varepsilon_s' = \varepsilon_{co}(\frac{c-d'}{c})$ Check whether assumption is correct or not.

$\varepsilon_s = \varepsilon_{co}(\frac{d-c}{c})$ Check whether assumption is correct or not.

- Even if one assumption is not verified, this alternative does not work.
- If both assumptions are verified together, this alternative works and moment is calculated with respect to centroid of concrete stress block. Then,

$M_o = F_s(d-0.375c) + F_s'(0.375c-d')$ $\quad \emptyset_o = \frac{\varepsilon_{co}}{c}$

A.4.3 Assume both steels have not yielded

$F_c = 0.6666666667 f_c' bc$

$F_s = A_s E_s \varepsilon_{co} \left(\frac{d-c}{c}\right)$

$F_s' = A_s' E_s \varepsilon_{co} \left(\frac{c-d'}{c}\right)$

Force equilibrium is set as follows:

$F_c + F_s' - F_s = 0$

$0.6666666667 f_c' bc + A_s' E_s \varepsilon_{co} \left(\frac{c-d'}{c}\right) - A_s E_s \varepsilon_{co} \left(\frac{d-c}{c}\right) = 0$

$2f_c' bc^2 + (3E_s \varepsilon_{co} A_s' + 3 E_s \varepsilon_{co} A_s)c + (-3E_s \varepsilon_{co} A_s' d' - 3E_s \varepsilon_{co} A_s d) = 0$ (A.19)

If (A.19) is expressed in ($Ax^2 + Bx + C$) form, the constants are obtained as follows:

$A = 2f_c'b$

$B = 3E_s\varepsilon_{co}A_s' + 3E_s\varepsilon_{co}A_s$

$C = -3E_s\varepsilon_{co}A_s'd' - 3E_s\varepsilon_{co}A_sd$

$\Delta = (3E_s\varepsilon_{co}A_s' + 3E_s\varepsilon_{co}A_s)^2 + 24f_c'b(E_s\varepsilon_{co}A_s'd' + E_s\varepsilon_{co}A_sd)$

$c = \frac{-B+\sqrt{\Delta}}{2A}$

$\varepsilon_s' = \varepsilon_{co}(\frac{c-d'}{c})$ Check whether assumption is correct or not.

$\varepsilon_s = \varepsilon_{co}(\frac{d-c}{c})$ Check whether assumption is correct or not.

- Even if one assumption is not verified, this alternative does not work.
- If both assumptions are verified together, this alternative works and moment is calculated with respect to centroid of concrete stress block. Then,

$M_o = F_s(d-0.375c) + F_s'(0.375c-d')$ $\quad$ $Ø_o = \frac{\varepsilon_{co}}{c}$

A.4.4 Assume only compression steel has yielded

$F_c = 0.6666666667f_c'bc$

$F_s = A_s E_s\varepsilon_{co}\left(\frac{d-c}{c}\right)$

$F_s' = A_s'f_{yd}$

Force equilibrium is set as follows:

$F_c + F_s' - F_s = 0$

$0.6666666667f_c'bc + A_s'f_{yd} - A_s E_s\varepsilon_{co}\left(\frac{d-c}{c}\right) = 0$

$2f_c'bc^2 + (3A_s'f_{yd} + 3E_s\varepsilon_{co}A_s)c - 3E_s\varepsilon_{co}A_sd = 0$ $\quad$ (A.20)

If (A.20) is expressed in ($Ax^2 + Bx + C$) form, the constants are obtained as follows:

$A = 2f_c'b$

$B = 3A_s'f_{yd} + 3E_s\varepsilon_{co}A_s$

$C = -3E_s\varepsilon_{co}A_sd$

$\Delta = (3A_s'f_{yd} + 3E_s\varepsilon_{co}A_s)^2 + 24f_c'bE_s\varepsilon_{co}A_sd$

$c = \frac{-B+\sqrt{\Delta}}{2A}$

$\varepsilon_s' = \varepsilon_{co}(\frac{c-d'}{c})$ Check whether assumption is correct or not.

$\varepsilon_s = \varepsilon_{co}(\frac{d-c}{c})$ Check whether assumption is correct or not.

- Even if one assumption is not verified, this alternative does not work.
- If both assumptions are verified together, this alternative works and moment is calculated with respect to centroid of concrete stress block. Then,

$M_o = F_s(d-0.375c) + F_s'(0.375c-d')$ $\quad \emptyset_o = \frac{\varepsilon_{co}}{c}$

A.4.5 No compression steel

Assume tension steel has yielded.

$F_c = 0.6666666667 f_c'bc$

$F_s = A_s f_{yd}$

Force equilibrium is set as follows:

$F_c - F_s = 0$

$0.6666666667 f_c'bc - A_s f_{yd} = 0$ (A.21)

$c = 1.5 \frac{f_{yd}A_s}{bf_c'}$

$\varepsilon_s = \varepsilon_{co}(\frac{d-c}{c})$ Check whether assumption is correct or not.

- If assumption is verified, this alternative works and moment is calculated with respect to centroid of concrete stress block. Then,

$M_o = F_s(d-0.375c)$ $\quad \emptyset_o = \frac{\varepsilon_{co}}{c}$

- If assumption is not verified, this alternative does not work and general solution is used.

$F_s = A_s E_s \varepsilon_{co} \left(\frac{d-c}{c}\right)$ $\quad 0.6666666667 f_c'bc - A_s E_s \varepsilon_{co} \left(\frac{d-c}{c}\right) = 0$ (A.22)

If (A.22) is expressed in $(Ax^2 + Bx + C)$ form, the constants are obtained as follows:

$A = 2f_c'b$

$B = 3E_s\varepsilon_{co}A_s$

$C = -3E_s\varepsilon_{co}A_s d$

$\Delta = (3E_s\varepsilon_{co}A_s)^2 + 24 f_c'b E_s\varepsilon_{co}A_s d$

$M_o = F_s(d-0.375c)$ $\quad \emptyset_o = \frac{\varepsilon_{co}}{c}$

A.5 AAC reaches its crushing strain ($\varepsilon_{ctop}=\varepsilon_{cu}$)

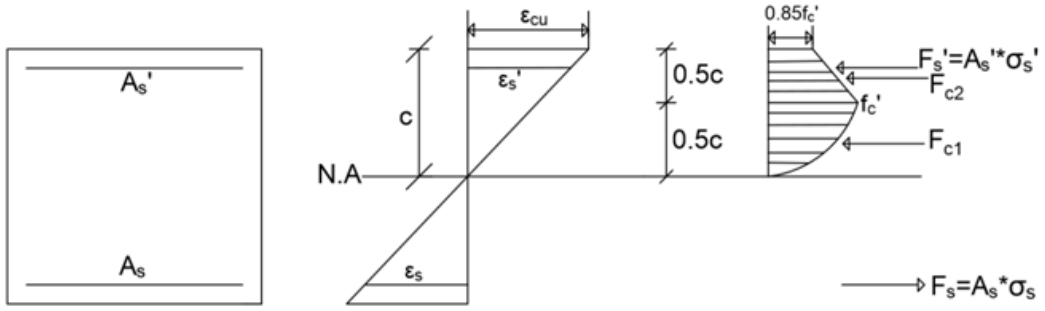

Figure A.9: Stress-strain profile for AAC crushing

$\frac{\varepsilon_s'}{\varepsilon_{cu}} = \frac{c-d'}{c}$	$\frac{\varepsilon_s}{\varepsilon_{cu}} = \frac{d-c}{c}$
$\varepsilon_s = \varepsilon_{cu}(\frac{d-c}{c})$	$\varepsilon_s' = \varepsilon_{cu}(\frac{c-d'}{c})$
$\sigma_s = E_s\varepsilon_{cu}(\frac{d-c}{c}) \leq f_{yd}$	$\sigma_s' = E_s\varepsilon_{cu}(\frac{c-d'}{c}) \leq f_{yd}$
$F_s = E_s\varepsilon_{cu}\left(\frac{d-c}{c}\right)A_s$	$F_s' = E_s\varepsilon_{cu}\left(\frac{c-d'}{c}\right)A_s'$

F_{c1} and $\overline{y1}$ are the same with (A.10) and (A.11).

$F_{c1} = 0.3333333333f_c'bc$ (A.23)

$\overline{y1} = 0.3125c$ (A.24)

To calculate F_{c2}, put $\varepsilon_{ctop} = \varepsilon_{cu}$ in (A.8). Then,

$F_{c2} = 0.4625f_c'bc$ (A.25)

To calculate $\overline{y2}$, put $\sigma_c = 0.85f_c'$ in (A.9). Then,

$\overline{y2} = 0.2432432432c$ (A.26)

A.5.1 Assume both steels have yielded

$F_c = F_{c1} + F_{c2} = 0.7958333333f_c'bc$

$F_s = A_sf_{yd}$

$F_s' = A_s'f_{yd}$

Force equilibrium is set as follows:

$F_c + F_s' - F_s = 0$

$0.7958333333f_c'bc + A_s'f_{yd} - A_sf_{yd} = 0$ (A.27)

$c = 1.256544503\frac{f_{yd}(A_s - A_s')}{bf_c'}$

$\varepsilon_s' = \varepsilon_{cu}(\frac{c-d'}{c})$ Check whether assumption is correct or not.

$\varepsilon_s = \varepsilon_{cu}(\frac{d-c}{c})$ Check whether assumption is correct or not.

- Even if one assumption is not verified, this alternative does not work.
- If both assumptions are verified together, this alternative works and moment is calculated with respect to centroid of F_{c2}. Then,

$M_u = F_s(d-0.2567567568c) + F_s'(0.2567567568c-d') - F_{c1}(0.4307432432c)$

$Ø_u = \frac{\varepsilon_{cu}}{c}$

A.5.2 Assume only tension steel has yielded

$F_c = 0.7958333333f_c'bc$

$F_s = A_sf_{yd}$

$F_s' = A_s' E_s\varepsilon_{cu}\left(\frac{c-d'}{c}\right)$

Force equilibrium is set as follows:

$F_c + F_s' - F_s = 0$

$0.7958333333f_c'bc + A_s' E_s\varepsilon_{cu}\left(\frac{c-d'}{c}\right) - A_sf_{yd} = 0$

$0.7958333333f_c'bc^2 + (E_s\varepsilon_{cu}A_s' - A_sf_{yd})c - E_s\varepsilon_{cu}A_s'd' = 0$ (A.28)

If (A.28) is expressed in $(Ax^2 + Bx + C)$ form, the constants are obtained as follows:

$A = 0.7958333333f_c'b$

$B = E_s\varepsilon_{cu}A_s' - A_sf_{yd}$

$C = -E_s\varepsilon_{cu}A_s'd'$

$\Delta = (E_s\varepsilon_{cu}A_s' - A_sf_{yd})^2 + 3.183333333\, f_c'bE_s\varepsilon_{cu}A_s'd'$

$c_{1,2} = \frac{-B \pm \sqrt{\Delta}}{2A}$

$\varepsilon_s' = \varepsilon_{cu}(\frac{c-d'}{c})$ Check whether assumption is correct or not.

$\varepsilon_s = \varepsilon_{cu}(\frac{d-c}{c})$ Check whether assumption is correct or not.

- Even if one assumption is not verified, this alternative does not work.
- If both assumptions are verified together, this alternative works and moment is calculated with respect to centroid of concrete stress block. Then,

$M_u = F_s(d-0.2567567568c) + F_s'(0.2567567568c-d') - F_{c1}(0.4307432432c)$

$\emptyset_u = \frac{\varepsilon_{cu}}{c}$

A.5.3 Assume both steels have not yielded

$F_c = 0.7958333333 f_c' bc$

$F_s = A_s E_s \varepsilon_{cu} \left(\frac{d-c}{c}\right)$

$F_s' = A_s' E_s \varepsilon_{cu} \left(\frac{c-d'}{c}\right)$

Force equilibrium is set as follows:

$F_c + F_s' - F_s = 0$

$0.7958333333 f_c' bc + A_s' E_s \varepsilon_{cu} \left(\frac{c-d'}{c}\right) - A_s E_s \varepsilon_{cu} \left(\frac{d-c}{c}\right) = 0$

$0.7958333333 f_c' bc^2 + (E_s \varepsilon_{cu} A_s' + E_s \varepsilon_{cu} A_s)c + (-E_s \varepsilon_{cu} A_s' d' - E_s \varepsilon_{cu} A_s d) = 0$ (A.29)

If (A.29) is expressed in $(Ax^2 + Bx + C)$ form, the constants are obtained as follows:

$A = 0.7958333333 f_c' b$

$B = E_s \varepsilon_{cu} A_s' + E_s \varepsilon_{cu} A_s$

$C = -E_s \varepsilon_{cu} A_s' d' - E_s \varepsilon_{cu} A_s d$

$\Delta = (E_s \varepsilon_{cu} A_s' + E_s \varepsilon_{cu} A_s)^2 + 3.183333333 f_c' b(E_s \varepsilon_{cu} A_s' d' + E_s \varepsilon_{cu} A_s d)$

$c = \frac{-B+\sqrt{\Delta}}{2A}$

$\varepsilon_s' = \varepsilon_{cu}(\frac{c-d'}{c})$ Check whether assumption is correct or not.

$\varepsilon_s = \varepsilon_{cu}(\frac{d-c}{c})$ Check whether assumption is correct or not.

- Even if one assumption is not verified, this alternative does not work.

- If both assumptions are verified together, this alternative works and moment is calculated with respect to centroid of concrete stress block. Then,

$M_u = F_s(d-0.2567567568c) + F_s'(0.2567567568c-d') - F_{c1}(0.4307432432c)$

$Ø_u = \frac{\varepsilon_{cu}}{c}$

A.5.4 Assume only compression steel has yielded

$F_c = 0.7958333333 f_c' bc$

$F_s = A_s E_s \varepsilon_{co} \left(\frac{d-c}{c}\right)$

$F_s' = A_s' f_{yd}$

Force equilibrium is set as follows:

$F_c + F_s' - F_s = 0$

$0.7958333333 f_c' bc + A_s' f_{yd} - A_s E_s \varepsilon_{cu} \left(\frac{d-c}{c}\right) = 0$

$0.7958333333 f_c' bc^2 + (A_s' f_{yd} + E_s \varepsilon_{cu} A_s)c - E_s \varepsilon_{cu} A_s d = 0$ (A.30)

If (A.30) is expressed in $(Ax^2 + Bx + C)$ form, the constants are obtained as follows:

$A = 0.7958333333 f_c' b$

$B = A_s' f_{yd} + E_s \varepsilon_{cu} A_s$

$C = - E_s \varepsilon_{cu} A_s d$

$\Delta = (A_s' f_{yd} + E_s \varepsilon_{cu} A_s)^2 + 3.183333333 f_c' b E_s \varepsilon_{cu} A_s d$ $c = \frac{-B+\sqrt{\Delta}}{2A}$

$\varepsilon_s' = \varepsilon_{cu}(\frac{c-d'}{c})$ Check whether assumption is correct or not.

$\varepsilon_s = \varepsilon_{cu}(\frac{d-c}{c})$ Check whether assumption is correct or not.

- Even if one assumption is not verified, this alternative does not work.
- If both assumptions are verified together, this alternative works and moment is calculated with respect to centroid of concrete stress block. Then,

$M_u = F_s(d-0.2567567568c) + F_s'(0.2567567568c-d') - F_{c1}(0.4307432432c)$

$Ø_u = \frac{\varepsilon_{cu}}{c}$

A.5.5 No compression steel

Assume tension steel has yielded.

$F_c = 0.7958333333 f_c' bc$

$F_s = A_s f_{yd}$

Force equilibrium is set as follows:

$F_c - F_s = 0$

$0.7958333333 f_c'bc - A_s f_{yd} = 0$ (A.31)

$c = 1.256544503 \frac{f_{yd} A_s}{b f_c'}$

$\varepsilon_s = \varepsilon_{cu}(\frac{d-c}{c})$ Check whether assumption is correct or not.

- If assumption is verified, this alternative works and moment is calculated with respect to centroid of concrete stress block. Then,

$M_u = F_s(d-0.2567567568c) - F_{c1}(0.4307432432c)$ $\quad \emptyset_u = \frac{\varepsilon_{cu}}{c}$

- If assumption is not verified, this alternative does not work and general solution is used.

$F_s = A_s E_s \varepsilon_{cu} \left(\frac{d-c}{c}\right)$

$0.7958333333 f_c'bc - A_s E_s \varepsilon_{cu} \left(\frac{d-c}{c}\right) = 0$ (A.32)

If (A.32) is expressed in $(Ax^2 + Bx + C)$ form, the constants are obtained as follows:

$A = 0.7958333333 f_c'b$

$B = E_s \varepsilon_{cu} A_s$

$C = - E_s \varepsilon_{cu} A_s d$

$\Delta = (E_s \varepsilon_{cu} A_s)^2 + 3.183333333 f_c'b E_s \varepsilon_{cu} A_s d$

$M_u = F_s(d-0.2567567568c) - F_{c1}(0.4307432432c$ $\quad \emptyset_u = \frac{\varepsilon_{cu}}{c}$

APPENDIX B

FIBER REINFORCED SECTION ANALYSIS

All failure modes are mathematically explained in order to clarify the calculations behind MS Excel Spreadsheet. Solution procedure of fiber reinforced sections is illustrated in this part.

B.1 Prior to Cracking

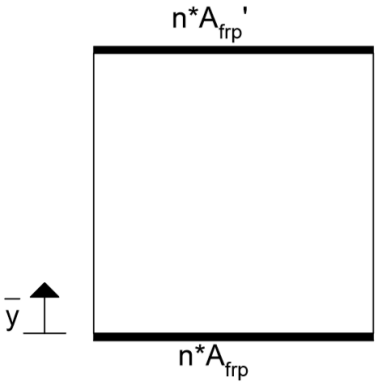

Figure B.1: Section analysis for prior to cracking case

$$n = \frac{E_{frp}}{E_c}$$

$$\bar{y} = \frac{n*A'_{frp}*h + b*h*\frac{h}{2}}{b*h + n*A'_{frp}} \qquad f_{ctf,d} = \frac{f_{ctf,k}}{\gamma_M} \qquad M_{cr} = \frac{f_{ctf,d}*I_{tr}}{\bar{y}}$$

$$Ø_{cr} = \frac{M_{cr}}{E_c*I}$$

$$I_{tr} = \frac{1}{12}bh^3 + bh(\frac{h}{2} - \bar{y})^2 + nA_{frp}\bar{y}^2 + nA_{frp}'(h - \bar{y})^2$$

B.2 After Cracking

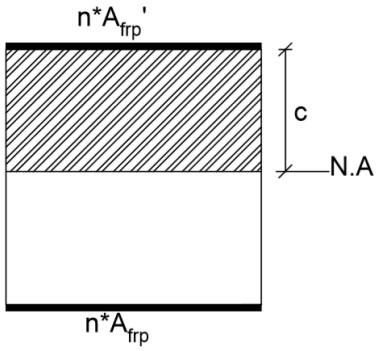

Figure B.2: Section analysis for after cracking case

Force Equilibrium:

$bc\frac{c}{2} + nA_{frp}'c = nA_{frp}(h-c)$

$bc^2 + c(2nA_{frp}'+2nA_{frp})-2nA_{frp}h = 0$ (B.1)

If (B.1) is expressed in $(Ax^2 + Bx + C)$ form, the constants are obtained as follows:

$A = b$

$B = 2nA_{frp}'+2nA_{frp}$

$C = -2nA_{frp}h$

$\Delta = B^2-4AC$ $c = \frac{-B+\sqrt{\Delta}}{2A}$

$I_{cr} = \frac{1}{3}bc^3+nA_{frp}(h-c)^2+nA_{frp}'c^2$ $\emptyset_{cr} = \frac{M_{cr}}{E_c*I_{cr}}$

B.3 Concrete reaches its maximum compressive strength ($\varepsilon_{ctop}=\varepsilon_{co}$)

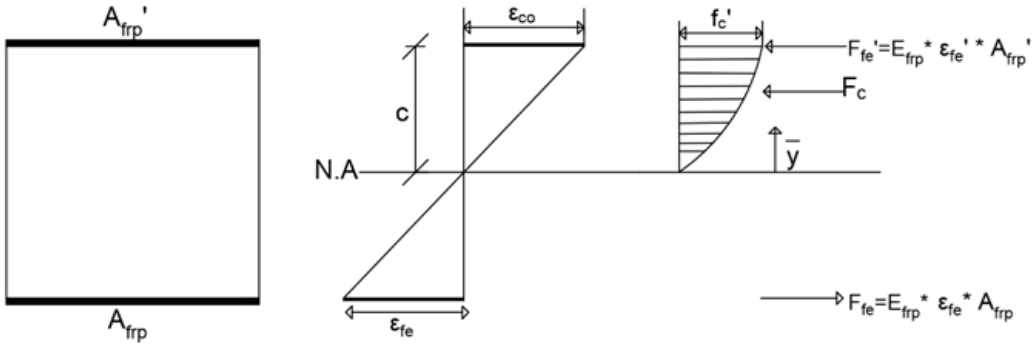

Figure B.3: Stress-strain profile at which $\varepsilon = \varepsilon_{co}$

B.3.1 Both FRP's Do Not Debond

$F_c = 0.6666666667 f_c' bc$

$F_{fe} = E_{frp}\varepsilon_{co}(\frac{h-c}{c})A_{frp}$

$F_{fe}' = E_{frp}\varepsilon_{co}A_{frp}'$

$0.6666666667 f_c' bc^2 + c(E_{frp}\varepsilon_{co}A_{frp}' + E_{frp}\varepsilon_{co}A_{frp}) - E_{frp}\varepsilon_{co}A_{frp}h = 0$

$A = 0.6666666667 f_c' b$

$B = E_{frp}\varepsilon_{co}A_{frp}' + E_{frp}\varepsilon_{co}A_{frp}$

$C = -E_{frp}\varepsilon_{co}A_{frp}$

$M = F_{fe} * (h - c + \bar{y}) + F_{fe}' * (c - \bar{y})$ $\quad$ $\emptyset_o = \frac{\varepsilon_{co}}{c}$

B.4 Concrete reaches its crushing strain ($\varepsilon_{ctop} = \varepsilon_{cu}$)

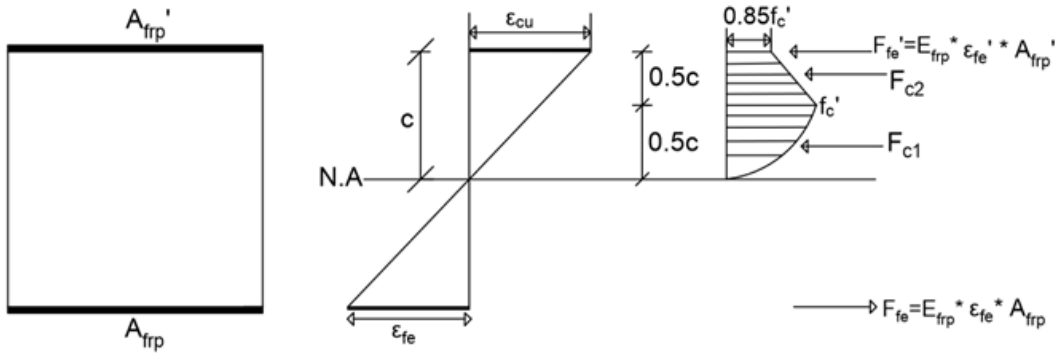

Figure B.4: Stress-strain profile for AAC crushing

B.4.1 Both FRP's Do Not Debond

$F_c = 0.7958333333 f_c' bc$

$F_{fe} = E_{frp}\varepsilon_{cu}(\frac{h-c}{c})A_{frp}$

$F_{fe}' = E_{frp}\varepsilon_{cu}A_{frp}'$

$0.7958333333 f_c' bc^2 + c(E_{frp}\varepsilon_{cu}A_{frp}' + E_{frp}\varepsilon_{cu}A_{frp}) - E_{frp}\varepsilon_{cu}A_{frp}h = 0$

$A = 0.7958333333 f_c' b$

$B = E_{frp}\varepsilon_{cu}A_{frp}' + E_{frp}\varepsilon_{cu}A_{frp}$

$C = -E_{frp}\varepsilon_{cu}A_{frp}h$

$M=F_{fe} * (h - 0.5c + \overline{y2}) + F_{fe}' * (0.5c - \overline{y2})\text{-}F_{c1} * (0.1875c + \bar{y}2)$ $\quad \emptyset_u = \frac{\varepsilon_{cu}}{c}$

B.5 Debonding ($\varepsilon_{fe}= \varepsilon_{fd}$)

B.5.1 Debonding occurs in the ascending portion ($\varepsilon_{ctop} < \varepsilon_{co}$)

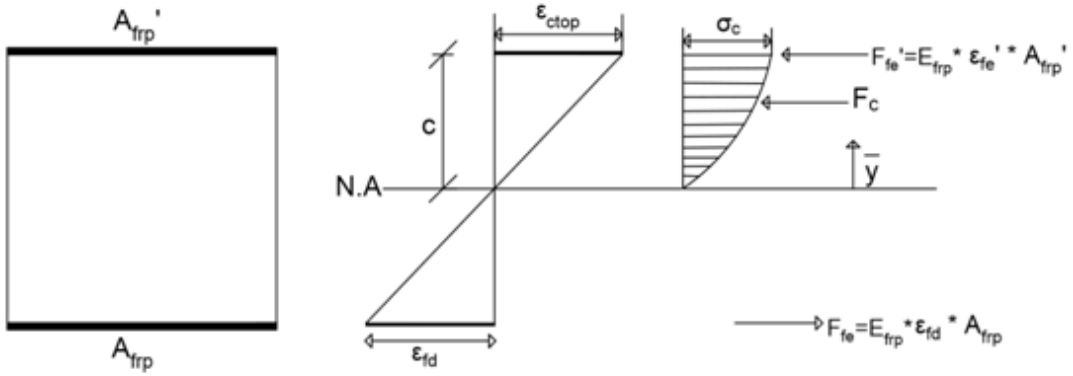

Figure B.5: Stress-strain profile for FRP debonding

B.5.1.1 Top FRP Does Not Debond

$F_c = \frac{f_c'b}{3\varepsilon_{co}^2(h-c)^2}(-3\varepsilon_{co}\varepsilon_{fd}c^3 - \varepsilon_{fd}^2c^3 + 3\varepsilon_{co}\varepsilon_{fd}hc^2)$

$F_{fe} = E_{frp}\varepsilon_{fd}A_{frp}$

$F_{fe}' = E_{frp}\varepsilon_{fd}(\frac{c}{h-c})A_{frp}'$

$A=\text{-}3f_c'b\varepsilon_{co}\varepsilon_{fd}\text{-}f_c'b\varepsilon_{fd}^2$

$B=3f_c'b\varepsilon_{co}\varepsilon_{fd}h\text{-}3\varepsilon_{co}^2\varepsilon_{fd}E_{frp}A_{frp}'\text{-}3\varepsilon_{co}^2\varepsilon_{fd}E_{frp}A_{frp}$

$C=3\varepsilon_{co}^2\varepsilon_{fd}E_{frp}A_{frp}'h+6\varepsilon_{co}^2\varepsilon_{fd}E_{frp}A_{frp}h$

$D= \text{-}3\varepsilon_{co}^2\varepsilon_{fd}E_{frp}A_{frp}h^2$

$M=F_{fe} * (h - c + \bar{y}) + F_{fe}' * (c - \bar{y})$

$\emptyset_u = \frac{\varepsilon_{ctop}}{c}$

B.5.2 Debonding occurs in the descending portion ($\varepsilon_{co} < \varepsilon_{ctop} < \varepsilon_{cu}$)

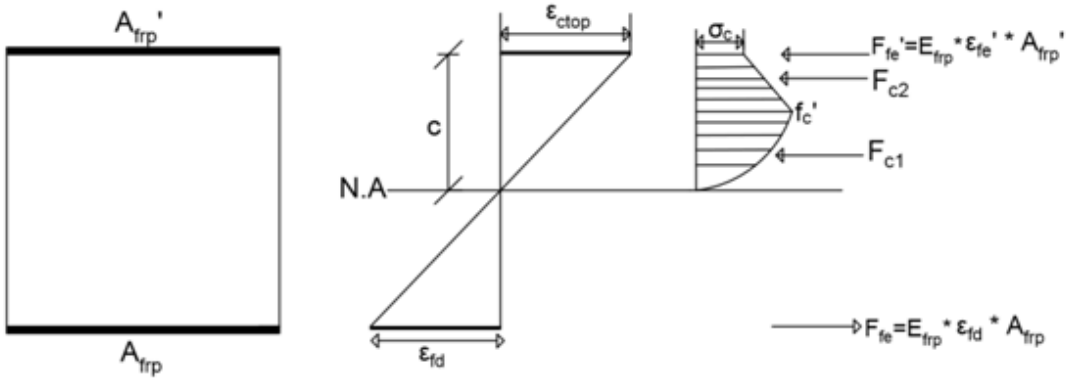

Figure B.6: Stress-strain profile for FRP debonding

B.5.2.1 Top FRP Does Not Debond

$F_{c1} = 0.3333333333 f_c' bc$

$F_{c2} = \frac{0.25 f_c' bc}{\varepsilon_{cu} - \varepsilon_{co}} (2\varepsilon_{cu} - 1.85\varepsilon_{co} - 0.15\varepsilon_{ctop})$

$F_{fe} = E_{frp} \varepsilon_{fd} A_{frp}$

$F_{fe}' = E_{frp} \varepsilon_{fd} (\frac{c}{h-c}) A_{frp}'$

$A = 0.7958333333 f_c' b\varepsilon_{co} - 0.8333333333 f_c' b\varepsilon_{cu} - 0.0375 f_c' b\varepsilon_{fd}$

$B = 0.8333333333 f_c' b\varepsilon_{cu} h - 0.7958333333 f_c' b\varepsilon_{co} h + E_{frp}\varepsilon_{fd} A_{frp}'\varepsilon_{cu} - E_{frp}\varepsilon_{fd} A_{frp}'\varepsilon_{co} + E_{frp}\varepsilon_{fd}\varepsilon_{cu} A_{frp} - E_{frp}\varepsilon_{fd}\varepsilon_{co} A_{frp}$

$C = -E_{frp}\varepsilon_{fd}\varepsilon_{cu} A_{frp} h + E_{frp}\varepsilon_{fd}\varepsilon_{co} A_{frp} h$

$M = F_{fe} * (h - 0.5c + \overline{y2}) + F_{fe}' * (0.5c - \overline{y2}) + 0.5c + \bar{y}2) - F_{c1} * (0.1875c + \bar{y}2)$

APPENDIX C

MOMENT-CURVATURE ANALYSIS

In this part, moment-curvature analysis results are presented in Figures C.1 through C.3 for all the test specimens. Figure C.1 shows the moment-curvature relation of Group-A specimens. Moment-curvature analysis results of Group-B and Group-C specimens are provided in Figure C.2 and Figure C.3, respectively. In these figures, it should be known that graphs were plotted by using the design debonding strain values given in Table 3.4 for fiber reinforced specimens.

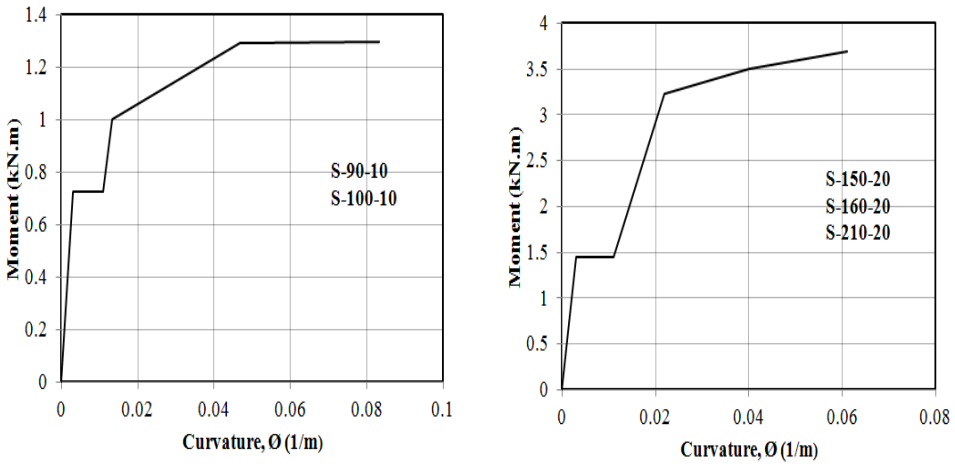

Figure C.1: Moment-curvature relation for Group-A specimens

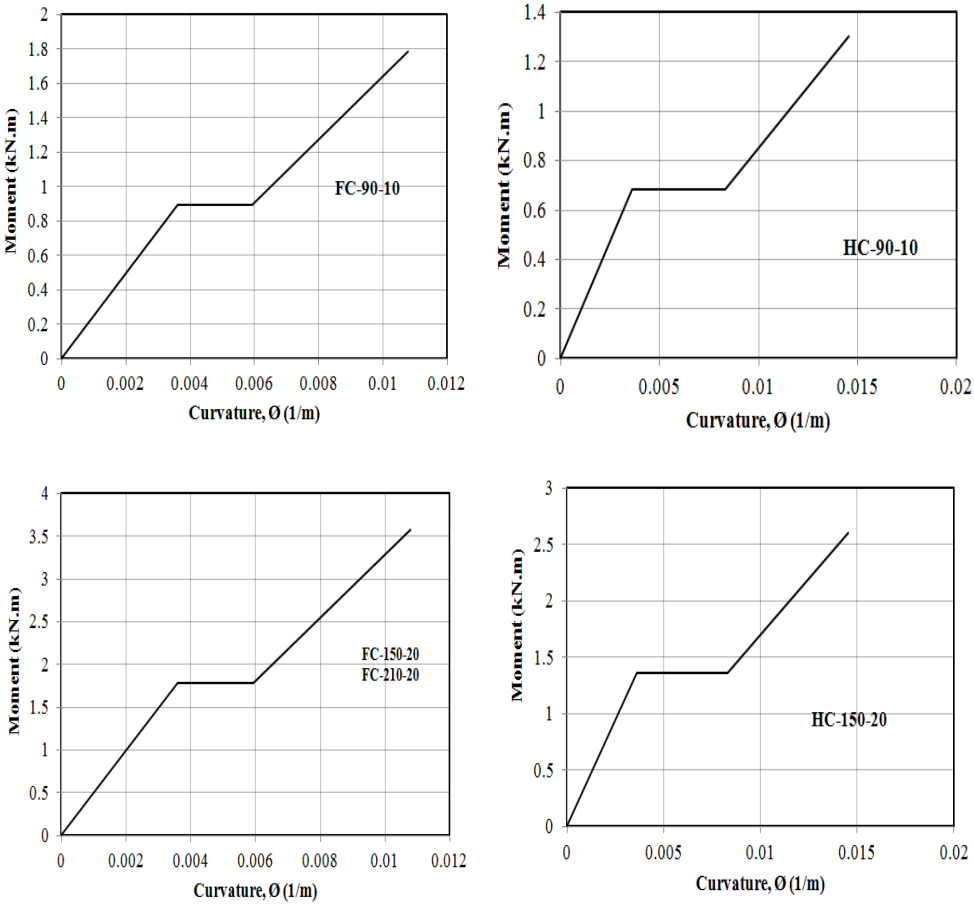

Figure C.2: Moment-curvature relation for Group-B specimens

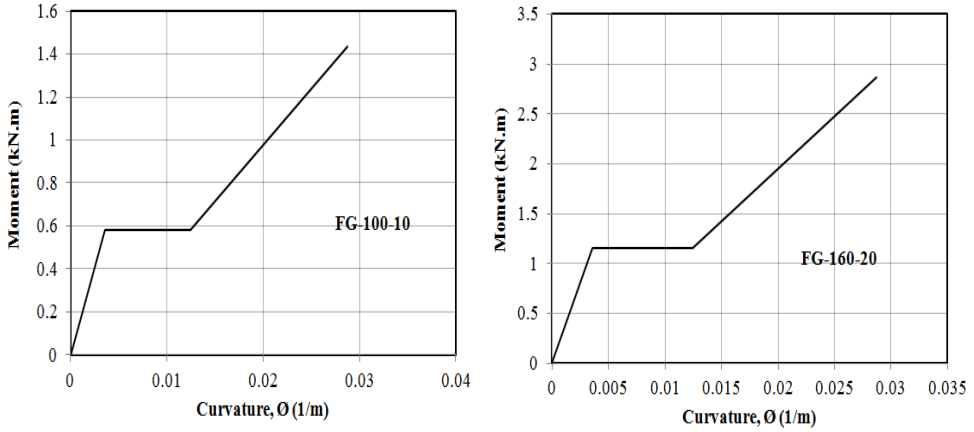

Figure C.3: Moment-curvature relation for Group-C specimens